DEVELOPMENT OF VALIDATED METHODS FOR SOIL-STRUCTURE ANALYSIS OF BURIED STRUCTURES

A Final Report submitted on research conducted under Grant No. 65A0561 from the California Department of Transportation (Caltrans).
This is also the Caltrans Final Report No. CA17-2754

Elnaz Esmaeilzadeh Seylabi[1], Wenyang Zhang[2], Eva Agapaki[3], Dimitiris Pitilakis[4], Scott J. Brandenberg[5], Jonathan P. Stewart[6], Ertugrul Taciroglu[7]

Civil & Environmental Engineering Department
University of California, Los Angeles

March 30, 2018

[1]Postdoctoral Scholar, Caltech, esmaeilzadeh@caltech.edu
[2]Ph.D. Candidate, UCLA, zwyll@ucla.edu
[3]Ph.D. Candidate, University of Cambridge, ea437@cam.ac.uk
[4]Assistant Professor, Aristotle University of Thessaloniki, dpitilakis@civil.auth.gr
[5]Professor, UCLA, sjbrandenberg@ucla.edu
[6]Professor, UCLA, jstewart@seas.ucla.edu
[7]Professor, UCLA, etacir@ucla.edu (Principal Investigator)

STATE OF CALIFORNIA DEPARTMENT OF TRANSPORTATION

TECHNICAL REPORT DOCUMENTATION PAGE

TR0003 (REV. 10/98)

1. REPORT NUMBER	2. GOVERNMENT ASSOCIATION NUMBER	3. RECIPIENT'S CATALOG NUMBER
CA17-2754		

4. TITLE AND SUBTITLE	5. REPORT DATE
Development of Validated Methods for Soil-Structure Analysis of Buried Structures	August 18, 2017
	6. PERFORMING ORGANIZATION CODE: UCLA

7. AUTHOR(S)	8. PERFORMING ORGANIZATION REPORT NO.
Elnaz Esmaeilzadeh Seylabi, Wenyang Zhang, Eva Agapaki, Dimitris Pitilakis Scott J. Brandenberg, Jonathan P. Stewart, Ertugrul Taciroglu	UCLA/CA17-2754

9. PERFORMING ORGANIZATION NAME AND ADDRESS	10. WORK UNIT NUMBER
UCLA, Civil & Environmental Engineering Dept University of California, Los Angeles, CA 90095	
	11 CONTRACT OF GRANT NUMBER: 65A0468

12. SPONSORING AGENCY ADDRESS	13. TYPE OF REPORT AND PERIOD COVERED
California Department of Transportation Engineering Service Center 1801 30th Street, MS 9-2/5i Sacramento CA 95816 California Department of Transportation Division of Research and Innovation, MS-83 1227 O Street Sacramento CA 95814	Final Report 6-1-2015 to 5-31-2017
	14. SPONSORING AGENCY CODE: 913

15. SUPPLEMENTAL NOTES

Prepared in cooperation with the State of California Department of Transportation.

16. ABSTRACT

.

17. KEYWORDS	18. DISTRIBUTION STATEMENT
Buried Structures, Soil-Structure-Interaction, Culverts, NCHRP-611	No restrictions. This document is available to the public through the National Technical Information Service, Springfield, VA 22161

19. SECURITY CLASSIFICATION (of this report)	20. NUMBER OF PAGES	21. PRICE
Unclassified		

ACKNOWLEDGEMENTS

Support for this research was provided by the California Department of Transportation under Research Contract No. 65A0561, which is gratefully acknowledged. We would like to acknowledge the valuable assistance and technical support of Caltrans staff in this project, particularly Carl Duan and Anoosh Shamsabadi. Caltrans Research Project Manager Peter Lee is recognized for his assistance in contract administration. Finally, we would like to acknowledge the technical assistance provided by Dan Wilson during the tests at the UC Davis Centrifuge Facility.

DISCLAIMER STATEMENT

EXECUTIVE SUMMARY

The main objective of this study has been to examine the predictive capabilities of various pseudo-static analytic methods of analysis in capturing key response parameters for culvert structures under seismic loads. These methods rely on several simplifying assumptions and consequently bear errors. State-of-the-art versions of these simplified methods of seismic analysis for buried/embedded structures were most recently articulated in the "NCHRP 611" report, and comparisons of their predictions to experimental data are made in the present study. Experiments comprised centrifuge tests on two specimens—one relatively-stiff rectangular and one relatively-flexible circular culvert—embedded in dense dry sand. Dimensions and properties of these specimens were representative of two large culverts selected from the "Caltrans Standard Plans." Both specimens and the soil media were well-instrumented, and were subjected to a series of harmonic, as well as low, moderate, and high amplitude broadband (earthquake) base excitations. Comparisons revealed various shortcomings of the NCHRP 611 methods. The most important issue was found to be the sensitivity of model results to the estimated soil shear strain, which represents the seismic demands on the culverts. Depending on the particular algorithmic branch of the NCHRP 611 methods adopted, some of the structural strains were over-predicted while others were under-predicted. Such inaccuracies should not necessarily lead to catastrophic results for culverts, but they nonetheless reduce the margins of safety and economy in their designs. Overall a "refined" version of the NCHRP 611 method, which used maximum shear strains obtained through a one-dimensional site response analysis, produced acceptable results for the rigid (rectangular) culvert specimen. For the flexible (circular) culvert, the results appeared fairly inaccurate.

Comparisons of experimental data were also made with predictions from a two-dimensional (plane-strain) finite element (FE) model. Material properties of this model were calibrated using data collected from accelerometer readings made by the centrifuge specimens' free-field arrays—i.e., part of the same data that were used for estimating the shear strain demands on the specimen culverts using the NCHRP 611 methods. Predictions made using this FE model were superior and exhibited acceptable errors.

Given the aforementioned findings, various detailed recommendations are made for future work in the final chapter of this report. The test data are archived at DesignSafe.org, and a Jupyter notebook is developed to serve as a front-end, providing easy access to data by other researchers. Additionally, the nonlinear soil model used in the finite element simulations is implemented as a user material subroutine (UMAT) for ABAQUS, and is also made publicly available.

Contents

Chapter 1

Introduction

1.1 Motivation and objectives

Seismic response of underground structures is a complex soil-structure interaction (SSI) problem in which two fundamental mechanisms are at play. Differences in motion between the free-field soil and the foundation system in the absence of excess or deficient mass between the two that are due to their stiffness contrast are collectively referred as Kinematic Interaction (KI) effects. Inertial Interaction (II) effects are, therefore, complementary, and are concerned with the soil reactions that develop to resist inertial forces associated with accelerations of the foundation-structure system relative to the soil. The kinematic component is generally considered to be more significant for buried structures due to their modest mass and their confinement by soil.

Limit equilibrium methods (e.g. Mononobe and Matsuo, 1929) are not appropriate for the seismic design of buried structures because their formulation does not reflect the SSI processes that are responsible for the formation of interface pressures. As such, a number of researchers (e.g., Wang, 1993a) proposed pseudo-static deformation-based approaches to take the effects of SSI into account for the seismic design of underground structures, followed by Penzien (2000b) and Hashash et al. (2001). In the said approaches, analytical elasticity-based formulations are provided to compute the seismic bending moments and hoop forces in circular structures. Methods proposed for computing internal seismic forces for rectangular structures, on the other hand, are based on static frame analysis.

More recently, Katona (2010) presented a finite element approach to obtain the seismic responses of buried culverts and cut-and-cover tunnels, by specifying quasi-static displacement profiles at the soil boundaries. These profiles taken as the products of free-field ground strains and the height of the modeled soil domain. As a result, the frequency content of

the ground motion—which, in turn, controls the wavelength—is indirectly represented in these methods through their impact on the shear strain. It should be noted that pseudo-static methods described in Wang (1993a) and Hashash et al. (2001) are very similar to the implementation in Katona (2010), so these are conceptually similar methods.

Limitations of the aforementioned methods are manifold: (1) They do not directly account for the broadband frequency content of seismic input excitations, as it is now well understood that seismic earth pressures vary with excitation wavelength (Brandenberg et al., 2015); (2) By conditioning the analyses on shear strain, their results are impacted by the challenges and limitations of 1D ground response assumption (e.g. Stewart et al., 2014); (3) The shear strain field is taken as uniform over the height of the buried structure, which may not be a valid assumption depending on the frequency of the seismic excitation, size of the underground structure, heterogeneity of the soil profile, and the mode of free-field wave. Finally, (4) these methods do not consider the relative inertia that can develop between the buried structure and the soil (that is, negative inertia that is caused by the culvert's empty space).

Current seismic design practices—articulated in, for example, the NCHRP Report 611 (Anderson et al., 2008)—are based on the procedures proposed by Wang (1993a) for circular and rectangular buried structures. During the last few years, a number of experimental (e.g. Cilingir and Madabhushi, 2011a,b; Lanzano et al., 2012, 2015; Tsinidis et al., 2015; Ulgen et al., 2015; Abuhajar et al., 2015), numerical (e.g. Hashash et al., 2005; Kontoe et al., 2014; Lanzano et al., 2015; Tsinidis et al., 2016; Tsinidis, 2017) and analytical (e.g. Bobet et al., 2008; Park et al., 2009; Bobet, 2010) studies have been conducted to explore the accuracy of the aforementioned simplified procedures. A non-exhaustive list of previously performed experimental studies on buried structures in dry sand is provided in Table 1.1.

We have undertaken here a centrifuge modeling program that is designed to extend the previous test results by (1) applying a wider range of ground motions spanning frequency contents where interaction effects are expected to range from significant to negligible; (2) applying a wider range of shaking amplitudes to investigate variable effects of soil non-linearity; and (3) deploying a relatively dense instrument configuration to enable detailed measurements of the culvert section responses as well as near- and far-field soils. The centrifuge tests were performed using the 9m-radius centrifuge at the Center for Geotechnical Modeling (CGM) at UC Davis (Kutter et al., 1994). Specimens consisted of two representative structures that were selected per Caltrans Standard Plans A62E and A62F (Department of Transportation State of California, 2015), which were embedded in a granular backfill.

The main objectives of this research project were (1) to compare the experimental findings with the design method described in NCHRP Report 611 (Anderson et al., 2008) in order to establish the validity (or lack thereof) of this method for the specific Caltrans configurations tested; (2) to formulate preliminary recommendations for Caltrans practice; and (3) to

identify future research needs in this area, as needed.

Table 1.1: A list of previous experimental studies on buried structures in dry sand.

Authors	Structure		Input motion			Soil relative density
	Type	Dimensions (m)	Type	PGA (g)	Frequency (Hz)	
Cilingir and Madabhushi (2011a,b)	S	5×0.061 5×0.155	H	$0.08 - 0.32$	$0.8 - 1.2$	45%
	C	5×0.088	E	$0.22 - 0.62$	$1 - 3$	
Lanzano et al. (2012, 2015)	C	6×0.06	H	$0.05 - 0.15$	$0.37 - 0.75$	40%, 75%
Tsinidis et al. (2015)	S	5×0.13	H, SS	$0.02 - 0.24$	$0.6 - 1.2$	90%
Ulgen et al. (2015)	S	2×0.06	H	$0.25 - 0.4$	$2 - 3.5$	70%
Abuhajar et al. (2015)	S	4.57×0.27 4.57×0.53	E	$0.11 - 0.33$	$0.46 - 1.45$	50%, 90%

In the second column, S and C stand for Square and Circle, respectively.
In the third column, dimensions are in width×thickness for square sections and in diameter×thickness for circular sections.
In the fourth column, H, E, and SS stand for Harmonic, Earthquake and Sine Sweep motions, respectively.

1.2 Organization of the report

In this report, we present all of the steps taken to achieve the objectives stated in §1.1. We provide details of the centrifuge modeling effort in Chapter 2. Methods we used for data archiving and processing are provided in Chapter 3. A brief review of the portions of the NCHPR 611 report on quantifying the seismic demands in culvert structures are provided in Chapter 4. We compare the experimental results against those estimated using the NCHRP 611 method in Chapter 5. We go through the steps we took for numerical modeling of the performed experiments and the calibration and validation of those models using experimental data in Chapter 6. Conclusions and recommendations are provided in Chapter 7.

Chapter 2

Centrifuge modeling

2.1 Centrifuge modeling and scaling laws

Scaling laws are used in centrifuge modeling so that the stress field at any point within the model is similar to what is expected in the prototype. As shown in Figure 2.1, if we scale down the size of the prototype by N, and increase the centrifugal acceleration by the same amount, the stress field in the model and the prototype—e.g., γH in Figure 2.1—will be similar. In other words, by using the aforementioned scaling law, we can capture the actual nonlinear and pressure-dependent behavior of the soil with the scaled model. Scaling laws for different parameters relevant to this research are listed in Table 2.1.

Table 2.1: Scaling laws (Madabhushi, 2014).

Parameter	Model/Prototype
Length	$1/N$
Area	$1/N^2$
Volume	$1/N^3$
Mass	$1/N^3$
Stress	1
Strain	1
Force	$1/N^2$
Moment	$1/N^3$
Time (dynamic)	$1/N$
Frequency	N
Displacement	$1/N$
Velocity	1
Acceleration	N

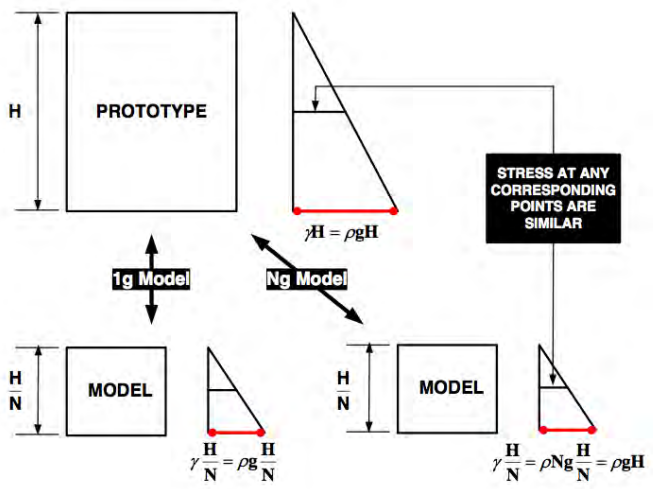

Figure 2.1: Scaling law for the stress field (Abuhajar et al., 2014).

2.2 UC Davis centrifuge and model container

We used the NEES@UCDavis Flexible Shear Beam Container 2 (FSB2), which has a number of aluminum shear rings as well as rubber shear layers to replicate free-field shear conditions in the soil deposit when no structure is present. The length, width, and height of this container are shown in Figure 2.2. After model construction and instrumentation, the filled container was mounted on the centrifuge arm to be spun. An illustrative example of a mounted model is shown in Figure 2.3.

2.3 Soil properties

2.3.1 Mechanical properties of the Ottawa sand

Ottawa sand, which is a pure quartz sand composed of naturally rounded grains, was used in the centrifuge experiments. Representative mechanical properties of the Ottawa sand are summarized in Table 2.2.

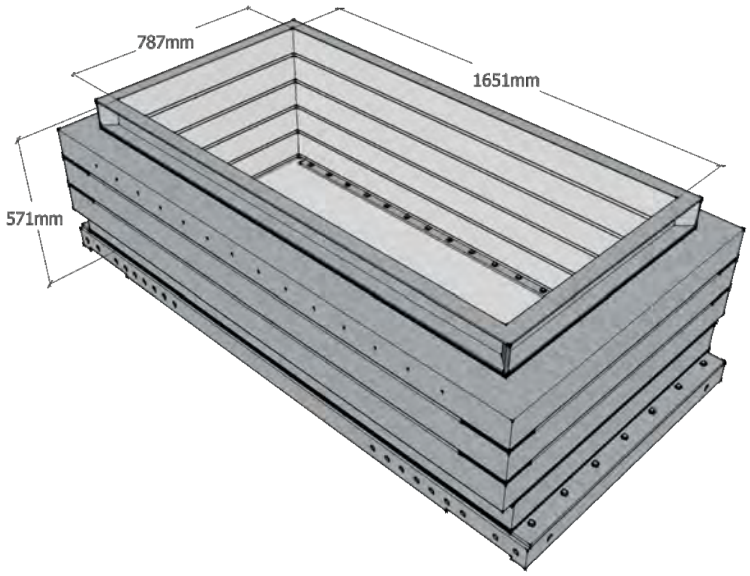

Figure 2.2: Geometry of the flexible shear beam container (FSB2).

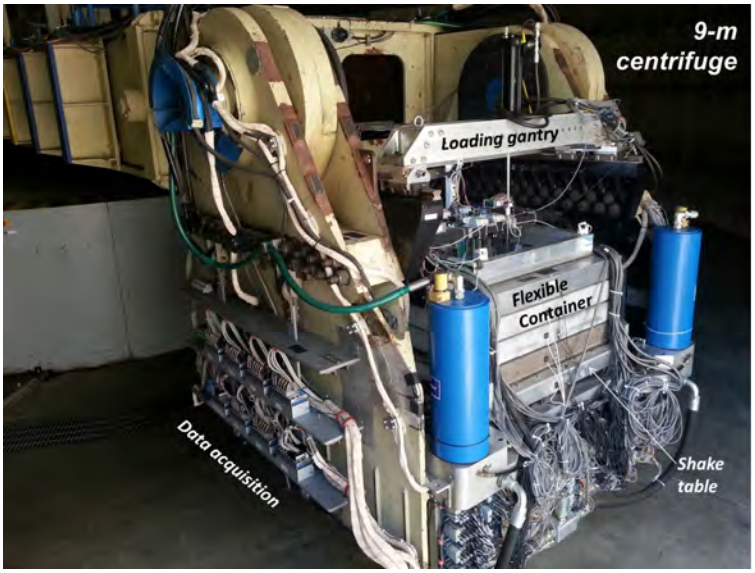

Figure 2.3: Configuration of the instrumented container mounted on the 9m-radius centrifuge arm (CGM, personal communication).

Table 2.2: Mechanical properties of the Ottawa sand (CGM, personal comunication).

Soil paeameter	Value
Specific gravity, G_s	2.673
Mean grain size, D_{50}	≈ 0.2 mm
Coefficient of uniformity, C_u	1.73
Coefficient of gradation, C_c	1.08

2.3.2 Air pluviation trials

We sought to place the sand in a dense state to represent the compacted select granular fills utilized in Caltrans culvert construction practice. The properties of these fill materials were obtained through personal communications with Caltrans engineers. An additional benefit of testing dense sand is that loose sands tend to densify during shaking, thereby resulting in significant evolutions of relative density during testing, whereas dense sand tends not to experience significant changes of state when vibrated. This simplifies interpretation of the test results. Therefore, we pluviated the sand at an average relative density of 93%. Details of the trial tests conducted to achieve this relative density are provided in Esmaeilzadeh Seylabi et al. (2017).

2.3.3 Shear wave velocity

Shear wave velocity measurements were obtained by bender elements (see, e.g. Brandenberg et al., 2006) at four positions in the soil profile—namely, near the bottom of the container, below the circular pipe, below the rectangular culvert, and close to the surface of the container. Figure 2.4 displays the array next to the box structure. Center-to-center distance between bender elements, which are piezoelectric transducers, were approximately 10 cm. In all these arrays, three bender elements were used (one source, and two receivers). The measurements were taken at $20g$ (during spinning). A high voltage step-wave motion was imposed on the source bender element, which causes the element to rapidly bend and induce a horizontally propagating shear wave with a vertical particle motion. Such a wave travels through the soil and deforms the receivers, and results in a recorded voltage signal. Shear wave velocity can then be estimated by measuring the time it takes for the waves to travel between the receivers. Details of the bender element signal processing is provided in Chapter 3.

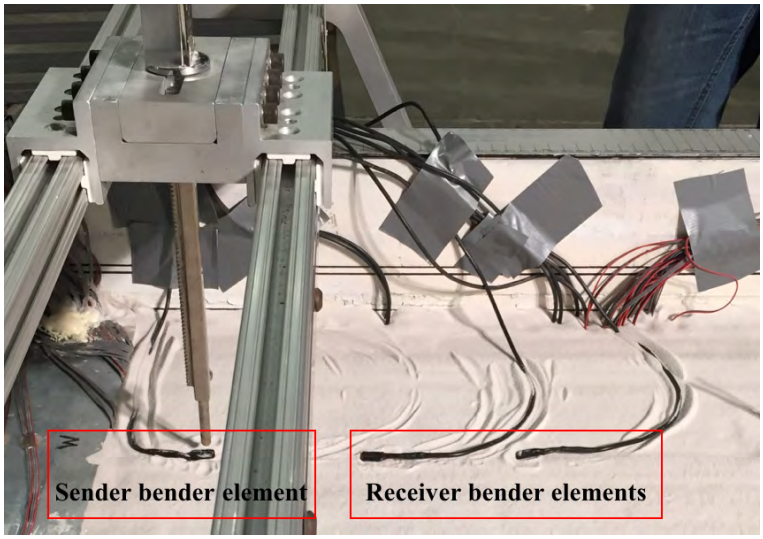

Figure 2.4: An array of the bender elements used for measuring shear wave velocity.

2.4 Culvert structures

2.4.1 Mechanical properties of the culvert structures

The Caltrans Standard Plans (Department of Transportation State of California, 2015) provide common configurations for culvert structures used in California. These culverts are typically either corrugated steel pipes or reinforced concrete box structures. The model structures, embedment depths, and soil properties adopted for the centrifuge models were selected to be consistent with these commonly used culvert types.

Pipe structure

The model specimen is a uniform seamless aluminum pipe with a thickness of 0.16 cm (0.065 in) and inside diameter of 12.37 cm (4.87 in). It is made from Aluminum 6061-T6 with $E = 68.95$ GPa (10^7 psi), $\gamma = 26.48$ kN/m^3 (0.0975 lb/in^3), and $\nu = 0.33$ (all based on manufacturer specifications rather than measurements). These dimensions were selected to match the static flexural stiffness of a representative prototype corrugated steel pipe structure (cf. Caltrans Standard Plans).

Box structure

The specimen is a box tube with inside dimensions of 18.4cm×10.8cm (7.25in×4.25in) and uniform thickness of 0.95 cm (0.375 in). Like the other specimen, it is made of Aluminum 6061-T6. These dimensions are selected to match the flexural stiffness of a representative reinforced concrete culvert structure (cf. Caltrans Standard Plans).

2.4.2 Strain gauges

Strain gauges are used to measure the response demands in the specimens, which can also be used to evaluate dynamic increments of internal forces. Our preliminary numerical simulations, as explained in the next section, showed that both specimens would exhibit measurable strains during seismic loading. We measured in-plane bending and in-plane axial (hoop) strains using dense strain gauge arrays on the walls of each structure.

Determination of ideal sensor positions

In order to determine the ideal positions for strain gauges, a numerical model was with a setting similar to the planned centrifuge experiments was developed, and analyses were carried out using an in-house finite element code to solve the wave equations in the frequency domain. The two-dimensional plane strain model was constructed with 8-node quadrilateral elements. Periodic boundaries were applied along the left and right sides of the model to mimic the behavior of the container walls. An elastic homogeneous soil with shear wave velocity of 198 m/s, unit weight of 17.5 kN/m^3 and Poisson's ratio of 0.3 were considered in all simulations. The properties of the box and pipe specimens were set as those for aluminum. Using this model, the steady-state response of the structures were obtained over frequency range of 0 to 25 Hz. Further details can be found in the data report by Esmaeilzadeh Seylabi et al. (2017). Figures 2.5 and 2.6 display the amplitude of the in-plane bending and hoop strain profiles for the pipe structure at three frequencies of 5, 14.5 and 25 Hz. These frequencies were chosen as the computed strain energy within the structure was more significant at frequencies close to the natural frequencies of the soil deposit— i.e., 4.95, 14.85, and 24.75 Hz for $V_s = 198$ m/s and layer thickness of 10 m. The results indicated that the maximum bending strains would occur at $\theta = 45$, 135, 225, and 315 degrees—a finding that enabled the optimal placement of the strain gauges.

Figure 2.7 displays the in-plane bending strain profile for the box structure at the selected frequencies. The strain profiles along the walls and roof visually appear to conform with linear or 2nd-order polynomial functions, whereas along the invert, strain profiles appear to be more compatible with 3rd-order polynomials. In-plane axial strains are not shown for the box structure, as they were very small in magnitude compared to the bending strain.

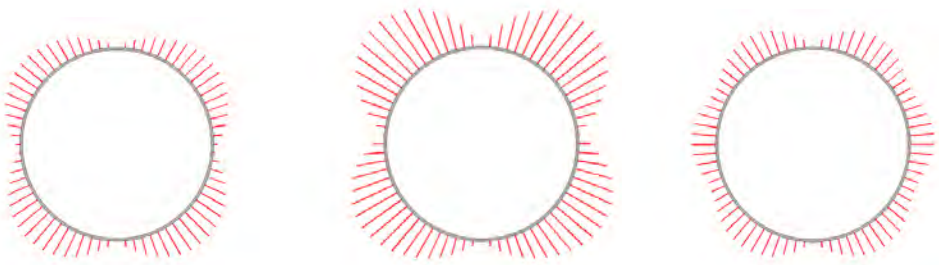

(a) $f = 5$ Hz (b) $f = 14.5$ Hz (c) $f = 25$ Hz

Figure 2.5: Amplitude of the steady-state bending strain profile of the pipe structure.

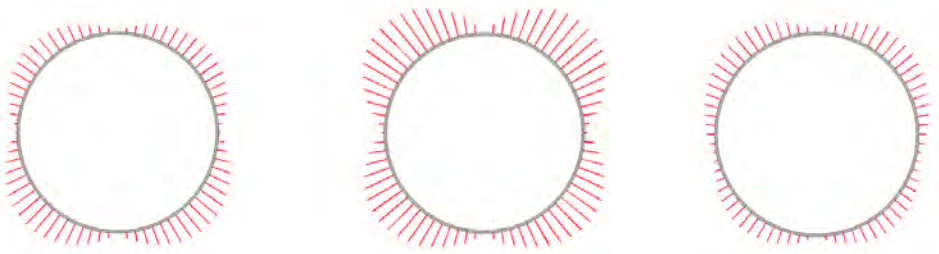

(a) $f = 5$ Hz (b) $f = 14.5$ Hz (c) $f = 25$ Hz

Figure 2.6: Amplitude of the steady-state hoop strain profile of the pipe structure.

(a) $f = 5$ Hz (b) $f = 14.5$ Hz (c) $f = 25$ Hz

Figure 2.7: Amplitude of the steady-state bending strain profile of the box structure.

"OMEGA KFH-6-350-C1-11L3M3R" strain gauges were used, which are linear-pattern prewired gauges with a nominal resistance of 350 Ω and three 3m leads. The gauge dimensions are 10.5 mm × 3.9 mm, and the gauge factor is 2.04. The gauge factor is defined as:

$$\mathrm{GF} = \frac{\Delta R/R}{\epsilon} \tag{2.1}$$

where R is the resistance of the strain gauge, ΔR is the change in the electrical resistance and ϵ is the measured strain. Using this gauge factor, the nominal sensitivity of the strain gauges can be obtained. Wheatstone full bridges were used to measure both bending and hoop (axial) strains. Therefore, for the bending strain ϵ_b,

$$\frac{\Delta V}{V} = \mathrm{GF}\epsilon_b \tag{2.2}$$

and for the hoop (axial) strain ϵ_h,

$$\frac{\Delta V}{V} = \mathrm{GF}\frac{1+\nu}{2}\epsilon_h\,. \tag{2.3}$$

Therefore, for a Wheatstone full bridge configured to measure bending strain, the nominal sensitivity is 2.04, and for the hoop full strains, it is 1.36. The latter is obtained by multiplying the gauge factor by $(1+\nu)/2$, in which $\nu = 0.33$ is the Poisson's ratio of aluminum.

For the gauge bonding inside and outside of the box, we used an "Omega TT300 complete heat cure adhesive kit," following a specific curing procedure of applying a uniform pressure of about 207 kPa (30 psi) for 2 hours at the temperature of 125°C. In order to accelerate the process, the clamp mechanism shown in Figure 2.8 was used for installing multiple gauges simultaneously.

Affixing the strain gauges to the inside of the pipe was not straightforward due to the curved surface and small diameter of the pipe compared to the box. Applying the specified pressure for the required duration ruled out the use of the TT300 adhesive. As an alternative, we used the "instant Omega SG496 adhesive" to install the strain gauges manually, one pair at a time. This adhesive is not as durable as the TT300, resulting in a shorter design life for the pipe structure. However, we deemed the solution acceptable for a single test. Figure 2.9 shows the steps we took for installation. A camera was installed inside the pipe to aid alignment and placement of the strain gauges.

2.5 Model construction and instrumentation configurations

Ottawa sand was pluviated in the model container in 2.5 cm thick layers, using the same procedure as that for trial air-pluviation (cf. §2.3.2). The surface of each layer was vacuumed to make it even. The pipe and box structures were placed such that the soil cover

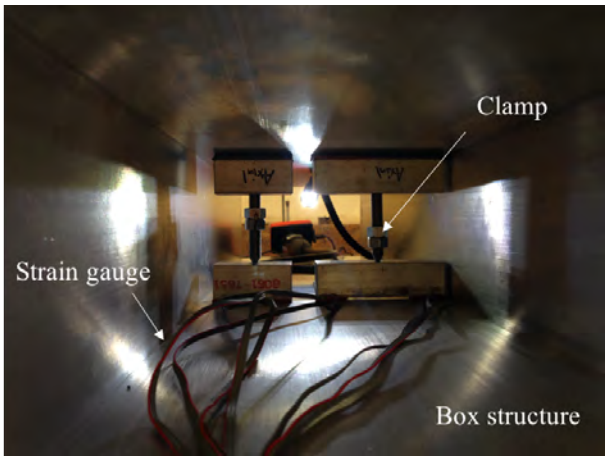

Figure 2.8: The clamp used for installation of strain gauges inside the box.

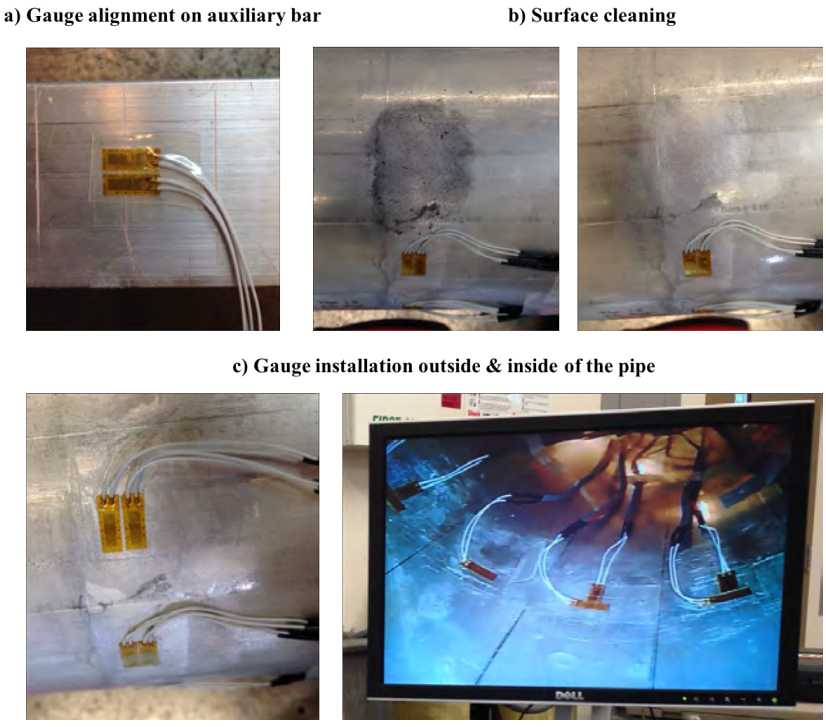

Figure 2.9: Installation of strain gauges inside and outside of the pipe.

for each was 15.24 cm (0.5 ft) and 3 cm (0.1 ft), respectively. These soil covers are in accord with the Caltrans Standard Plans. We used a hand-held vibrator to compact the soil around the specimen. Finally, a thin 0.5 cm layer of Monterey sand was placed above the last layer to prevent wind erosion during spinning. The top of the Monterey sand was sprayed with glue to create a crust.

Figure 2.10 displays an elevation view of the centrifuge model.

Sensors were placed in six stages at different elevations in the model, including 59 accelerometers. 43 of these were installed in soil or on the container while the rest were installed inside the specimens. A frame was mounted on top of the container to secure the LPs in order to measure the soil surface settlements and to capture the specimens' vertical displacements. Another frame was used to attach Linear Potentiometers (LPs) to the container wall and to measure the associated lateral displacements (see Figure 2.10). All sensors used in the model were connected to a data acquisition system as shown in Figure 2.3. We used thin aluminum sheets to close the two-ends of each specimen in order to avoid intrusion of sand inside the specimens. The plan views of the centrifuge model at different elevations are shown in Figures 2.11-2.16. The configurations and labels of the sensors installed on the pipe and box structures are provided in Figure 2.17.

The IDs used for labeling the sensors, along with their positions and configurations, are provided in Table 2.3. X, Y, and Z are measured from the reference point located at the center and bottom of the south wall of the container. (i, j, k) indicate how the sensors are aligned. For ICPs (Integrated Circuit Piezoelectric sensors), LPs and bender elements, (+1, 0, 0) is the positive direction of X axis and (0, 0, +1) is the positive direction of Z axis. For strain gauges, (+1, 0, 0) represents in-plane axial strain and (0,+1,0) represents in-plane bending strain. The remaining columns respectively provide information on the serial numbers of the sensors in UC Davis' inventory, the sensor sensitivities and their unit, the maximum values of the sensors' range and their unit, the DAQ ranges and their unit, and the excitation values and their unit.

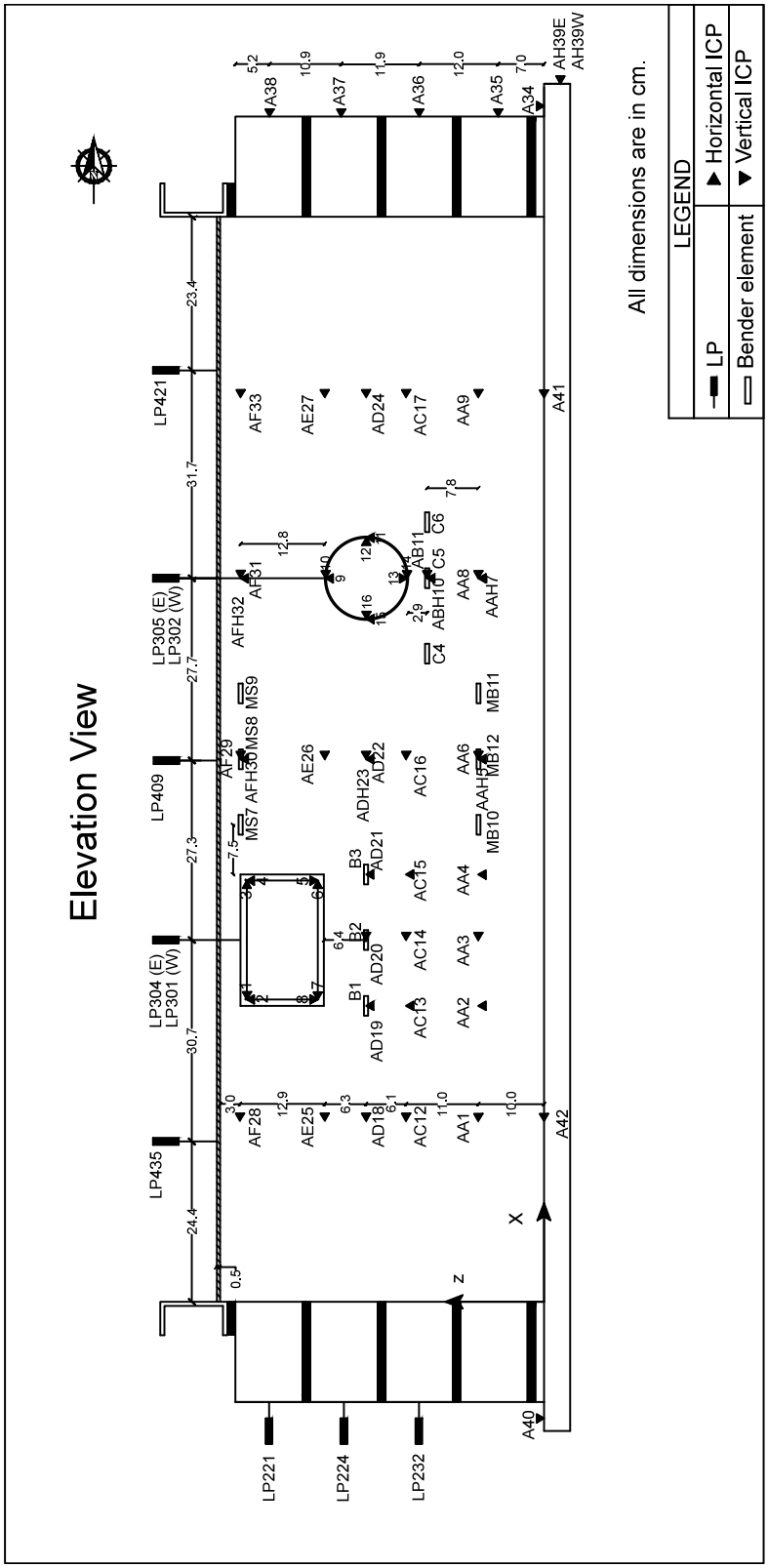

Figure 2.10: Elevation view of the centrifuge model.

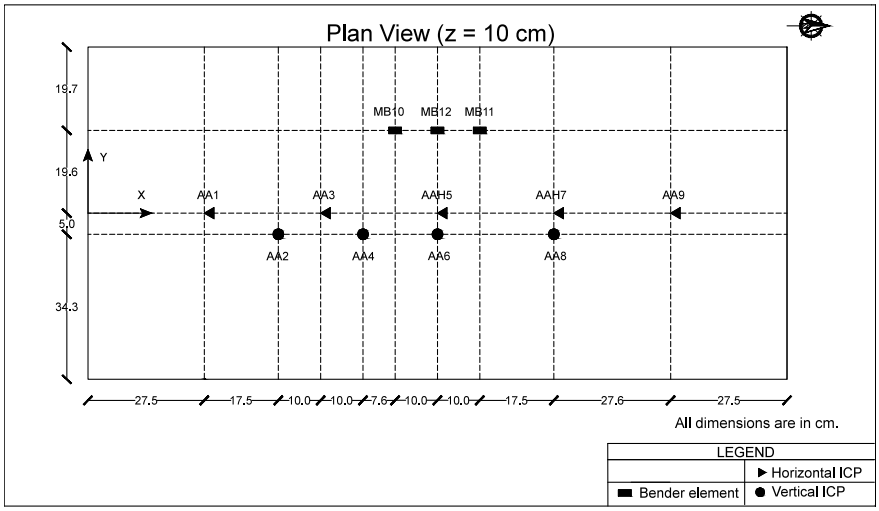

Figure 2.11: Plan view of the constructed model at $z = 10$ cm.

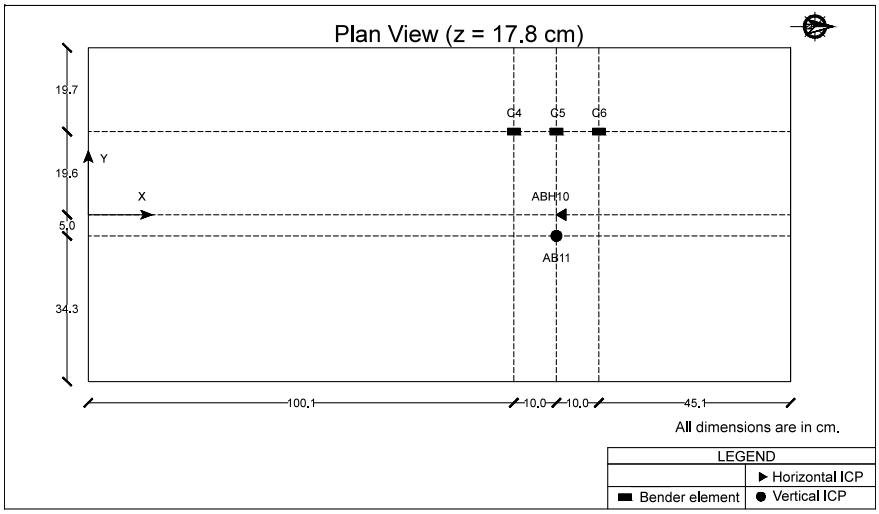

Figure 2.12: Plan view of the constructed model at $z = 17.8$ cm.

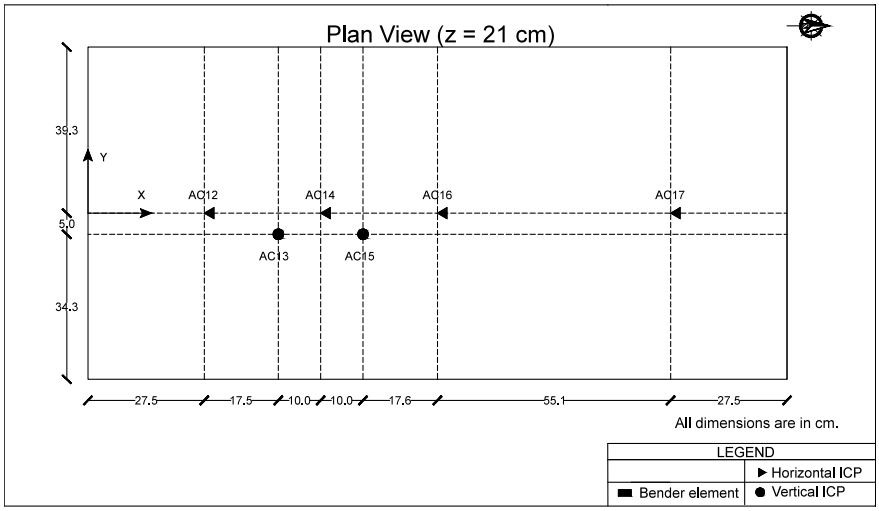

Figure 2.13: Plan view of the constructed model at $z = 21$ cm.

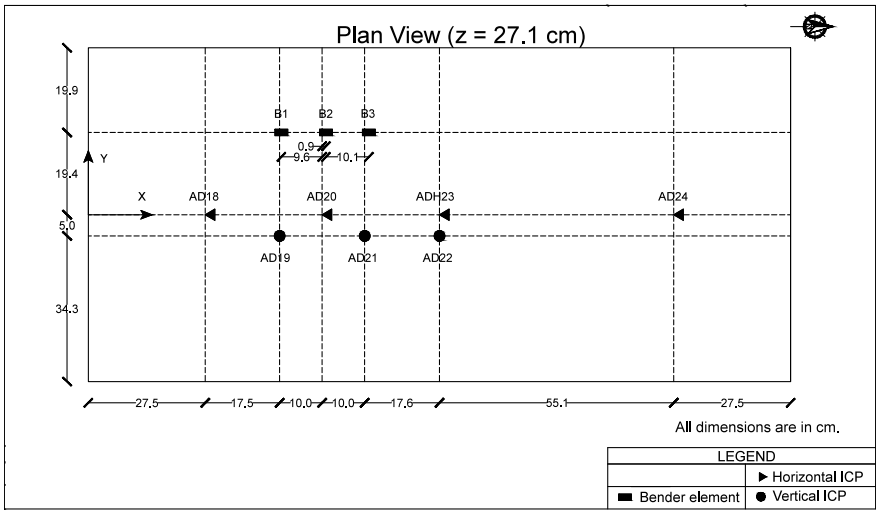

Figure 2.14: Plan view of the constructed model at $z = 27.1$ cm.

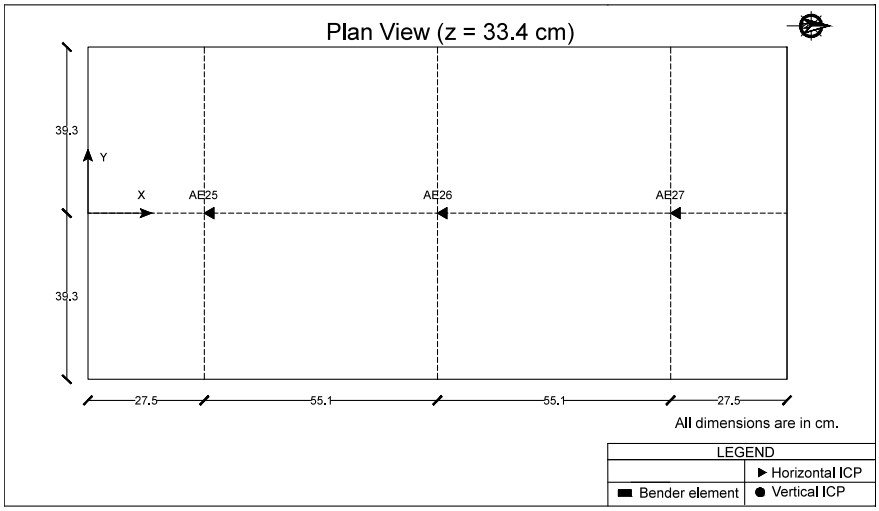

Figure 2.15: Plan view of the constructed model at $z = 33.4$ cm.

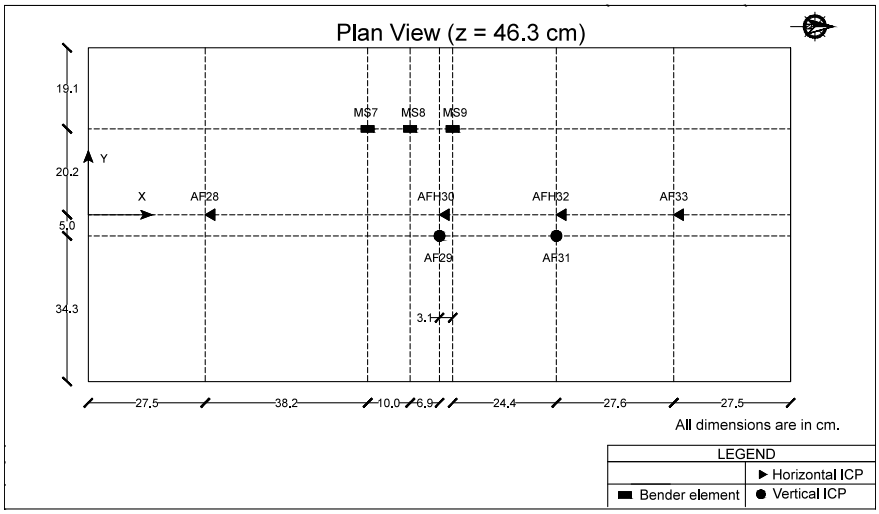

Figure 2.16: Plan view of the constructed model at $z = 46.3$ cm.

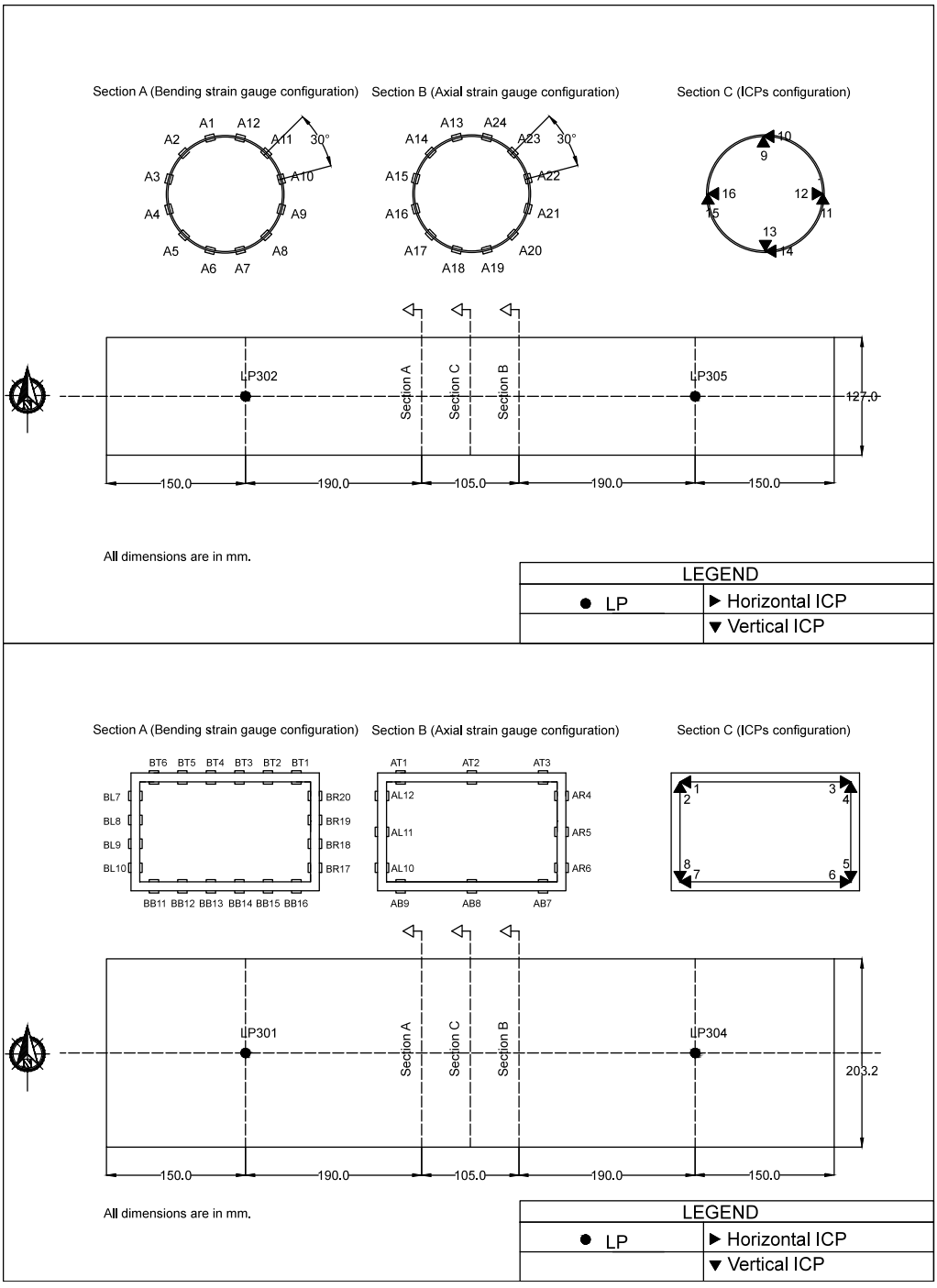

Figure 2.17: Layout of the instrumentation for the rectangular and circular specimens.

Table 2.3: The list of the sensors used for model instrumentation.

Sensor (XDCR) ID	X (cm)	Y (cm)	Z (cm)	i	j	k	Interface Channel	Serial Number	Sensitivity	Sensitivity Units	XDCR Range	XDCR Units	DAQ Range	DAQ Units	Excitation Value	Excitation Units
H-E	East shaker	-	-	-1	0	0	ICP1-0	6025	52.4	mV/g	100	g	5	Volts	2	mA
H-W	West shaker	-	-	-1	0	0	ICP1-1	6021	53.6	mV/g	100	g	5	Volts	2	mA
AA1	27.5	0	10	-1	0	0	ICP3-4	3166	106.5	mV/g	50	g	5	Volts	2	mA
AA2	45	-5	10	0	0	1	ICP3-6	37003	48.8	mV/g	100	g	5	Volts	2	mA
AA3	55	0	10	-1	0	0	ICP3-5	96937	101.7	mV/g	50	g	5	Volts	2	mA
AA4	65	-5	10	0	0	1	ICP2-2	6023	52.2	mV/g	100	g	5	Volts	2	mA
AAH5	82.6	0	10	-1	0	0	ICP2-4	3962	106.5	mV/g	50	g	5	Volts	2	mA
AA6	82.6	-5	10	0	0	1	ICP2-3	37001	48.3	mV/g	100	g	5	Volts	2	mA
AAH7	110.1	0	10	-1	0	0	ICP6-2	3164	106.6	mV/g	50	g	5	Volts	2	mA
AA8	110.1	-5	10	0	0	1	ICP6-3	6020	52.3	mV/g	100	g	5	Volts	2	mA
AA9	137.7	0	10	-1	0	0	ICP6-0	4523	104.9	mV/g	50	g	5	Volts	2	mA
ABH10	110.1	0	17.8	-1	0	0	ICP6-1	3162	108.1	mV/g	50	g	5	Volts	2	mA
AB11	110.1	-5	17.8	0	0	1	ICP7-2	6022	53.4	mV/g	100	g	5	Volts	2	mA
AC12	27.5	0	21	-1	0	0	ICP3-7	107647	48.8	mV/g	100	g	5	Volts	2	mA
AC13	45	-5	21	0	0	1	ICP1-5	37097	47.8	mV/g	100	g	5	Volts	2	mA
AC14	55	0	21	-1	0	0	ICP1-7	99513	50.5	mV/g	100	g	5	Volts	2	mA
AC15	65	-5	21	0	0	1	ICP2-6	6016	51.0	mV/g	100	g	5	Volts	2	mA
AC16	82.6	0	21	-1	0	0	ICP2-0	21060	52.4	mV/g	100	g	5	Volts	2	mA
AC17	137.7	0	21	-1	0	0	ICP6-4	5607	54.1	mV/g	100	g	5	Volts	2	mA
AD18	27.5	0	27.1	-1	0	0	ICP1-3	107064	49.0	mV/g	100	g	5	Volts	2	mA
AD19	45	-5	27.1	0	0	1	ICP1-4	36999	49.1	mV/g	100	g	5	Volts	2	mA
AD20	55	0	27.1	-1	0	0	ICP3-2	107644	48.6	mV/g	100	g	5	Volts	2	mA
AD21	65	-5	27.1	0	0	1	ICP3-1	37004	48.1	mV/g	100	g	5	Volts	2	mA
AD22	82.6	-5	27.1	0	0	1	ICP2-1	6026	54.1	mV/g	100	g	5	Volts	2	mA
ADH23	82.6	0	27.1	-1	0	0	ICP3-3	132245	48.3	mV/g	100	g	5	Volts	2	mA
AD24	137.7	0	27.1	-1	0	0	ICP6-5	73964	53.2	mV/g	100	g	5	Volts	2	mA
AE25	27.5	0	33.4	-1	0	0	ICP1-2	73959	52.2	mV/g	100	g	5	Volts	2	mA
AE26	82.6	0	33.4	-1	0	0	ICP2-5	21048	51.3	mV/g	100	g	5	Volts	2	mA
AE27	137.7	0	33.4	-1	0	0	ICP6-6	21044	53.1	mV/g	100	g	5	Volts	2	mA
AF28	27.5	0	46.3	-1	0	0	ICP1-6	127803	50.3	mV/g	100	g	5	Volts	2	mA
AF29	82.6	-5	46.3	0	0	1	ICP3-0	37002	48.2	mV/g	100	g	5	Volts	2	mA
AFH30	82.6	0	46.3	-1	0	0	ICP2-7	127802	49.9	mV/g	100	g	5	Volts	2	mA
AF31	110.1	-5	46.3	0	0	1	ICP7-0	37006	47.9	mV/g	100	g	5	Volts	2	mA
AFH32	110.1	0	46.3	-1	0	0	ICP7-1	99511	50.4	mV/g	100	g	5	Volts	2	mA
AF33	137.7	0	46.3	-1	0	0	ICP6-7	108848	50.0	mV/g	100	g	5	Volts	2	mA
A34	North Base	0	0	0	0	-1	ICP8-3	97112	99.4	mV/g	50	g	5	Volts	2	mA
A35	North Wall	-5.5	7	-1	0	0	ICP8-0	3204	107.7	mV/g	50	g	5	Volts	2	mA
A36	North Wall	-0.7	19	-1	0	0	ICP7-7	5602	53.8	mV/g	100	g	5	Volts	2	mA
A37	North Wall	-0.7	30.9	-1	0	0	ICP7-6	107038	50.5	mV/g	100	g	5	Volts	2	mA
A38	North Wall	-0.3	41.8	-1	0	0	ICP7-5	127804	50.5	mV/g	100	g	5	Volts	2	mA
AH39E	North Base	-	-2.5	-1	0	0	ICP8-1	3160	108.0	mV/g	50	g	5	Volts	2	mA
AH39W	North Base	-	-2.5	-1	0	0	ICP8-2	3955	106.6	mV/g	50	g	5	Volts	2	mA
A40	South Base	0	0	0	0	-1	ICP8-4	21321	50.9	mV/g	100	g	5	Volts	2	mA
A41	137.7	0	0	-1	0	0	ICP7-4	127920	50.7	mV/g	100	g	5	Volts	2	mA
A42	27.5	0	0	-1	0	0	ICP7-3	21067	54.1	mV/g	100	g	5	Volts	2	mA
1	45.8	0	45.35	-1	0	0	ICP4-0	4435	105.8	mV/g	50	g	5	Volts	2	mA
2	45.8	0	45.35	0	0	1	ICP4-1	5268	106.4	mV/g	50	g	5	Volts	2	mA
3	64.2	0	45.35	1	0	0	ICP4-2	5274	105.3	mV/g	50	g	5	Volts	2	mA
4	64.2	0	45.35	0	0	1	ICP4-3	3163	106.4	mV/g	50	g	5	Volts	2	mA
5	64.2	0	34.55	0	0	-1	ICP4-4	97116	97.7	mV/g	50	g	5	Volts	2	mA
6	64.2	0	34.55	1	0	0	ICP4-5	97113	98.5	mV/g	50	g	5	Volts	2	mA
7	45.8	0	34.55	-1	0	0	ICP4-6	96938	100.9	mV/g	50	g	5	Volts	2	mA
8	45.8	0	34.55	0	0	-1	ICP4-7	97115	99.7	mV/g	50	g	5	Volts	2	mA
9	110.1	0	33.25	0	0	1	ICP5-0	3950	104.7	mV/g	50	g	5	Volts	2	mA

Table 2.3: The list of the sensors used for model instrumentation.

Sensor (XDCR) ID	X (cm)	Y (cm)	Z (cm)	i	j	k	Interface Channel	Serial Number	Sensitivity	Sensitivity Units	XDCR Range	XDCR Units	DAQ Range	DAQ Units	Excitation Value	Excitation Units
10	110.1	0	33.25	-1	0	0	ICP5-1	3948	105.8	mV/g	50	g	5	Volts	2	mA
11	116.3	0	27.05	0	0	1	ICP5-2	96936	98.8	mV/g	50	g	5	Volts	2	mA
12	116.3	0	27.05	1	0	0	ICP5-3	5267	103.8	mV/g	50	g	5	Volts	2	mA
13	110.2	0	20.85	0	0	-1	ICP5-4	5276	104.6	mV/g	50	g	5	Volts	2	mA
14	110.2	0	20.85	-1	0	0	ICP5-5	3203	102.9	mV/g	50	g	5	Volts	2	mA
15	104	0	27.05	0	0	1	ICP5-6	4534	104.8	mV/g	50	g	5	Volts	2	mA
16	104	0	27.05	-1	0	0	ICP5-7	3964	105.0	mV/g	50	g	5	Volts	2	mA
BT1	62.7	5.25	46.3	0	1	0	Bridge7-0	-	2.0	mV/Volt	1	milistrain	25	mV	3.3	Volts
BT2	59.6	5.25	46.3	0	1	0	Bridge7-1	-	2.0	mV/Volt	1	milistrain	25	mV	3.3	Volts
BT3	56.5	5.25	46.3	0	1	0	Bridge7-2	-	2.0	mV/Volt	1	milistrain	25	mV	3.3	Volts
BT4	53.5	5.25	46.3	0	1	0	Bridge7-3	-	2.0	mV/Volt	1	milistrain	25	mV	3.3	Volts
BT5	50.4	5.25	46.3	0	1	0	Bridge7-4	-	2.0	mV/Volt	1	milistrain	25	mV	3.3	Volts
BT6	47.3	5.25	46.3	0	1	0	Bridge7-5	-	2.0	mV/Volt	1	milistrain	25	mV	3.3	Volts
BL7	44.8	5.25	43.8	0	1	0	Bridge1-0	-	2.0	mV/Volt	1	milistrain	25	mV	3.3	Volts
BL8	44.8	5.25	41.2	0	1	0	Bridge1-1	-	2.0	mV/Volt	1	milistrain	25	mV	3.3	Volts
BL9	44.8	5.25	38.7	0	1	0	Bridge1-2	-	2.0	mV/Volt	1	milistrain	25	mV	3.3	Volts
BL10	44.8	5.25	36.1	0	1	0	Bridge1-3	-	2.0	mV/Volt	1	milistrain	25	mV	3.3	Volts
BB11	47.3	5.25	33.6	0	1	0	Bridge8-0	-	2.0	mV/Volt	1	milistrain	25	mV	3.3	Volts
BB12	50.4	5.25	33.6	0	1	0	Bridge8-1	-	2.0	mV/Volt	1	milistrain	25	mV	3.3	Volts
BB13	53.5	5.25	33.6	0	1	0	Bridge8-2	-	2.0	mV/Volt	1	milistrain	25	mV	3.3	Volts
BB14	56.5	5.25	33.6	0	1	0	Bridge8-3	-	2.0	mV/Volt	1	milistrain	25	mV	3.3	Volts
BB15	59.6	5.25	33.6	0	1	0	Bridge8-4	-	2.0	mV/Volt	1	milistrain	25	mV	3.3	Volts
BB16	62.7	5.25	33.6	0	1	0	Bridge8-5	-	2.0	mV/Volt	1	milistrain	25	mV	3.3	Volts
BL17	65.2	5.25	36.1	0	1	0	Bridge1-4	-	2.0	mV/Volt	1	milistrain	25	mV	3.3	Volts
BL18	65.2	5.25	38.7	0	1	0	Bridge1-5	-	2.0	mV/Volt	1	milistrain	25	mV	3.3	Volts
BL19	65.2	5.25	41.2	0	1	0	Bridge1-6	-	2.0	mV/Volt	1	milistrain	25	mV	3.3	Volts
BL20	65.2	5.25	43.8	0	1	0	Bridge1-7	-	2.0	mV/Volt	1	milistrain	25	mV	3.3	Volts
AT1	47.3	-5.25	46.3	1	0	0	Bridge3-3	-	1.4	mV/Volt	1	milistrain	25	mV	3.3	Volts
AT2	55	-5.25	46.3	1	0	0	Bridge3-4	-	1.4	mV/Volt	1	milistrain	25	mV	3.3	Volts
AT3	62.3	-5.25	46.3	1	0	0	Bridge3-5	-	1.4	mV/Volt	1	milistrain	25	mV	3.3	Volts
AR4	65.2	-5.25	43.8	1	0	0	Bridge5-4	-	1.4	mV/Volt	1	milistrain	25	mV	3.3	Volts
AR5	65.2	-5.25	39.95	1	0	0	Bridge5-1	-	1.4	mV/Volt	1	milistrain	25	mV	3.3	Volts
AR6	65.2	-5.25	36.1	1	0	0	Bridge5-2	-	1.4	mV/Volt	1	milistrain	25	mV	3.3	Volts
AB7	62.3	-5.25	33.6	1	0	0	Bridge5-3	-	0.7	mV/Volt	1	milistrain	25	mV	3.3	Volts
AB8	55	-5.25	33.6	1	0	0	Bridge5-7	-	1.4	mV/Volt	1	milistrain	25	mV	3.3	Volts
AB9	47.3	-5.25	33.6	1	0	0	Bridge5-6	-	1.4	mV/Volt	1	milistrain	25	mV	3.3	Volts
AL10	44.8	-5.25	36.1	1	0	0	Bridge3-0	-	1.4	mV/Volt	1	milistrain	25	mV	3.3	Volts
AL11	44.8	-5.25	39.95	1	0	0	Bridge3-1	-	1.4	mV/Volt	1	milistrain	25	mV	3.3	Volts
AL12	44.8	-5.25	43.8	1	0	0	Bridge3-2	-	1.4	mV/Volt	1	milistrain	25	mV	3.3	Volts
A1	108.5	5.25	33.2	0	1	0	Bridge2-0	-	2.0	mV/Volt	1	milistrain	25	mV	3.3	Volts
A2	105.6	5.25	31.6	0	1	0	Bridge2-7	-	2.0	mV/Volt	1	milistrain	25	mV	3.3	Volts
A3	104	5.25	28.7	0	1	0	Bridge2-2	-	2.0	mV/Volt	1	milistrain	25	mV	3.3	Volts
A4	104	5.25	25.4	0	1	0	Bridge2-3	-	2.0	mV/Volt	1	milistrain	25	mV	3.3	Volts
A5	105.6	5.25	22.6	0	1	0	Bridge2-4	-	2.0	mV/Volt	1	milistrain	25	mV	3.3	Volts
A6	108.5	5.25	20.9	0	1	0	Bridge2-5	-	2.0	mV/Volt	1	milistrain	25	mV	3.3	Volts
A7	111.7	5.25	20.9	0	1	0	Bridge9-0	-	2.0	mV/Volt	1	milistrain	25	mV	3.3	Volts
A8	114.6	5.25	22.6	0	1	0	Bridge9-1	-	2.0	mV/Volt	1	milistrain	25	mV	3.3	Volts
A9	116.2	5.25	25.4	0	1	0	Bridge9-2	-	2.0	mV/Volt	1	milistrain	25	mV	3.3	Volts
A10	116.2	5.25	28.7	0	1	0	Bridge9-3	-	2.0	mV/Volt	1	milistrain	25	mV	3.3	Volts
A11	114.6	5.25	31.6	0	1	0	Bridge9-4	-	2.0	mV/Volt	1	milistrain	25	mV	3.3	Volts
A12	111.7	5.25	33.2	0	1	0	Bridge9-5	-	2.0	mV/Volt	1	milistrain	25	mV	3.3	Volts
A13	108.5	-5.25	33.2	1	0	0	Bridge11-0	-	1.4	mV/Volt	1	milistrain	25	mV	3.3	Volts
A14	105.6	-5.25	31.6	1	0	0	Bridge11-1	-	1.4	mV/Volt	1	milistrain	25	mV	3.3	Volts
A15	104	-5.25	28.7	1	0	0	Bridge11-2	-	1.4	mV/Volt	1	milistrain	25	mV	3.3	Volts

Table 2.3: The list of the sensors used for model instrumentation.

Sensor (XDCR) ID	X (cm)	Y (cm)	Z (cm)	i	j	k	Interface Channel	Serial Number	Sensitivity	Sensitivity Units	XDCR Range	XDCR Units	DAQ Range	DAQ Units	Excitation Value	Excitation Units
A16	104	-5.25	25.4	1	0	0	Bridge11-3	-	1.4	mV/Volt	1	milistrain	25	mV	3.3	Volts
A17	105.6	-5.25	22.6	1	0	0	Bridge11-4	-	1.4	mV/Volt	1	milistrain	25	mV	3.3	Volts
A18	108.5	-5.25	20.9	1	0	0	Bridge11-6	-	1.4	mV/Volt	1	milistrain	25	mV	3.3	Volts
A19	111.7	-5.25	20.9	1	0	0	Bridge4-0	-	1.4	mV/Volt	1	milistrain	25	mV	3.3	Volts
A20	114.6	-5.25	22.6	1	0	0	Bridge4-1	-	1.4	mV/Volt	1	milistrain	25	mV	3.3	Volts
A21	116.2	-5.25	25.4	1	0	0	Bridge4-6	-	1.4	mV/Volt	1	milistrain	25	mV	3.3	Volts
A22	116.2	-5.25	28.7	1	0	0	Bridge4-3	-	1.4	mV/Volt	1	milistrain	25	mV	3.3	Volts
A23	114.6	-5.25	31.6	1	0	0	Bridge4-4	-	1.4	mV/Volt	1	milistrain	25	mV	3.3	Volts
A24	111.7	-5.25	33.2	1	0	0	Bridge4-5	-	1.4	mV/Volt	1	milistrain	25	mV	3.3	Volts
LP301	55.1	24.25	49.8	0	0	-1	HOC 1-0	301	997.4	mV/Volt	3	inch	5	Volts	5	Volts
LP435	24.4	-1.35	49.8	0	0	-1	HOC 1-1	435	995.5	mV/Volt	4	inch	5	Volts	5	Volts
LP421	141.8	-2.05	49.8	0	0	-1	HOC 1-4	421	991.7	mV/Volt	4	inch	5	Volts	5	Volts
LP305	110.1	-24.25	49.8	0	0	-1	HOC 1-5	305	991.3	mV/Volt	3	inch	5	Volts	5	Volts
LP304	55.1	-24.25	49.8	0	0	-1	HOC 1-6	304	1029.6	mV/Volt	3	inch	5	Volts	5	Volts
LP221	South Wall	-	41.9	1	0	0	HOC 1-7	221	987.2	mV/Volt	2	inch	5	Volts	5	Volts
LP224	South Wall	-	30.5	1	0	0	HOC 2-0	224	982.7	mV/Volt	2	inch	5	Volts	5	Volts
LP232	South Wall	-	19.1	1	0	0	HOC 2-1	232	982.5	mV/Volt	2	inch	5	Volts	5	Volts
LP409	82.4	-1.75	49.8	0	0	-1	HOC 2-2	409	996.5	mV/Volt	4	inch	5	Volts	5	Volts
LP302	110.1	24.25	49.8	0	0	-1	HOC 2-3	302	1004.3	mV/Volt	3	inch	5	Volts	5	Volts
MB10	72.6	19.6	10	1	0	0	-	-	-	-	-	-	-	-	-	-
MB11	92.6	19.6	10	-1	0	0	-	-	-	-	-	-	-	-	-	-
MB12	82.6	19.6	10	1	0	0	-	-	-	-	-	-	-	-	-	-
C5	110.1	19.6	17.8	1	0	0	-	-	-	-	-	-	-	-	-	-
C6	100.1	19.6	17.8	-1	0	0	-	-	-	-	-	-	-	-	-	-
B1	45.4	19.4	27.1	1	0	0	-	-	-	-	-	-	-	-	-	-
B2	55.9	19.4	27.1	1	0	0	-	-	-	-	-	-	-	-	-	-
B3	66	19.4	27.1	-1	0	0	-	-	-	-	-	-	-	-	-	-
MS7	72.6	20.2	46.3	1	0	0	-	-	-	-	-	-	-	-	-	-
MS8	82.6	20.2	46.3	-1	0	0	-	-	-	-	-	-	-	-	-	-
MS9	92.6	20.2	46.3	-1	0	0	-	-	-	-	-	-	-	-	-	-

2.6 Ground motions

A total of 25 shaking events were applied at approximately $N = 21g$ centrifugal acceleration. Shaking was applied transverse to the culverts' long axes in the north-south direction. The sequence of the type of motions used to shake the model, including step-, earthquake-, and sinusoidal-functions are provided in Table 2.4.

Three earthquake ground motions are used in this study, which are obtained from the PEER ground motion database. The characteristics of these motions—i.e., target earthquake motions—are provided in Table 2.5. Figure 2.18 shows the 5%-damped spectral accelerations and the Arias intensity time series of the target earthquake motions.

Since the shake table on the centrifuge cannot perfectly reproduce a target motion, some signal modification needs to applied. This is typically achieved by first computing a command motion in which the high frequency content is increased relative to the target motion. This accounts for a loss of high-frequency content due to the mechanics of the shake table feedback control system. The achieved motion is then compared to the target motion, and the command motion is adjusted. Through an iterative process, the achieved base motions in the present tests were similar to, but not perfectly equivalent with, the target motions. For this reason, we suggest always using the measured base motions when interpreting the test data. The 5%-damped spectral accelerations and the Arias intensities of the measured base motions for the earthquakes (i.e., motions #03 to #11) are shown in Figure 2.19.

Sine-sweep motions were also used to shake the model the prototype frequencies of up to 25 Hz. As mentioned before, it was expected that soil-structure interaction effects would be more significant at higher frequencies. Two types—namely, constant acceleration and constant-velocity—target motions were used. It was found that constant velocity motions provided command inputs with richer high-frequency energy content.

The model was also excited with stepped-sine signals with discrete frequencies of 1.25, 1.85, 2.5, 3.75, 5, 7.5, 10, 17.5, and 25 Hz. At each iteration, the amplitudes of the stepped-sine functions at different frequencies were updated so that the amplitude of measured accelerations at the soil surface (as recorded by sensor AFH30) were nearly the same at all discrete frequencies considered. It should be noted that ideally a sine sweep function could be used for this purpose. However, calibration of the command input using sine sweep functions was not straightforward. This is why stepped sine functions were applied. Shaking the models with motions with the same surface acceleration amplitude permits observation of the frequency-dependence of the structural response.

Table 2.4: The sequence of the input motions used for shaking the model.

Event #	Command input type	Amp. factor applied to target motion	Command input file name	Measured data file name
1	Step function	0.6	01-Step.txt	01_0114201614211314281446.5rpm
2	Step function	1.5	02-Step.txt	02_0114201614211314462346.6rpm
3	Earthquake MUL279	0.1	03-RSN953_NORTHR_MUL279.shk	03_0114201614211315113246.3rpm
4	Earthquake SMT090	0.1	04-RSN1077_NORTHR_STM090.shk	04_0114201614211315320546.3rpm
5	Earthquake HEC000	0.33	05-HEC000.shk	05_0114201614211315443346.2rpm
6	Earthquake MUL279	0.5	03-RSN953_NORTHR_MUL279.shk	06_0114201614211315504546.2rpm
7	Earthquake SMT090	0.5	04-RSN1077_NORTHR_STM090.shk	07_0114201614211315555646.3rpm
8	Earthquake HEC000	1	05-HEC000.shk	08_0114201614211315592546.3rpm
9	Earthquake MUL279	1	03-RSN953_NORTHR_MUL279.shk	09_0114201614211316035346.3rpm
10	Earthquake SMT090	1	04-RSN1077_NORTHR_STM090.shk	10_0114201614211316285946.5rpm
11	Earthquake HEC000	3	05-HEC000.shk	11_0114201614211316325346.5rpm
12	Sine sweep 1 (constant acceleration)	1	12-input_command.txt	12_0114201614211316452846.4rpm
13	Sine sweep 1 (constant acceleration)	3	13-input_command.txt	13_0114201614211316494946.4rpm
14	Sine sweep 2 (constant acceleration)	1	14-sw-25to500-0.3g-iter00	14_0115201609420211375246.6rpm
15	Sine sweep 3	0.5	15-sw-25to500-0.1g-iter01	15_0115201609420212001846.5rpm
16	Sine sweep 3	0.1	16-sw-25to500-0.1g-iter01	16_0115201609420212184246.2rpm
17	Stepped sine 1 (iteration 0)	1	17-sine-0.1g-iter00	17_0115201609420212531246.4rpm
18	Stepped sine 2 (iteration 1)	1	18-sine-0.1g-iter01	18_0115201609420213453146.3rpm
19	Stepped sine 3 (iteration 2)	1	19-sine-0.1g-iter02	19_0115201609420213580946.3rpm
20	Stepped sine 4 (iteration 3)	1	20-sine-0.1g-iter03	20_0115201609420214370146.4rpm
21	Stepped sine 5 (iteration 4)	3	21-sine-0.1g-iter04	21_0115201609420214545146.4rpm
22	Stepped sine 6 (iteration 5)	3	22-sine-0.1g-iter05	22_0115201609420215145546.4rpm
23	Stepped sine 7 (iteration 6)	5	23-sine-0.1g-iter06	23_0115201609420215231946.5rpm
24	Sine sweep 4 (constant velocity)	0.5	24-ExponentialSineSweep.shk	24_0115201609420215314346.3rpm
25	Sine sweep 4 (constant velocity)	0.75	25-ExponentialSineSweep.shk	25_0115201609420215411846.3rpm

Table 2.5: Characteristics of the earthquake ground motions used in this study.

Earthquake	Year	Station	Component	Magnitude	R_{jb} (km)	V_{s30} (m/s)
Northridge	1994	Beverly Hills	MUL279	6.69	9.44	355.81
Northridge	1994	Santa Monica City Hall	STM090	6.69	17.28	336.20
Hector Mine	1999	Hector	HEC000	7.13	10.35	726.00

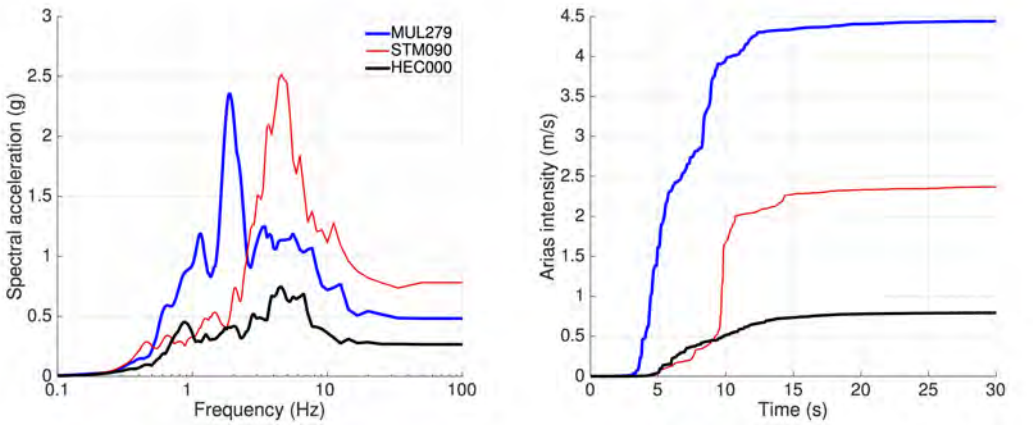

Figure 2.18: 5%-damped spectral acceleration and Arias intensity time series of the earthquake motions used in this study.

2.7 Known limitations

After excavation, we noticed that one of the wires of the BT3 bridge was slightly damaged, which may have affected the recorded data. Moreover, BL8 and AR5 bridges were not wired correctly. We also noticed that 6 ICPs inside the pipe specimen—which were labeled as 11, 12, 13, 14, 15, and 16—were detached from the structure. However, after checking the signals visually, it seemed that these detachments had happened after the shaking events.

It should be noted that we have not excluded data from any sensors that did not function properly in the archived data.

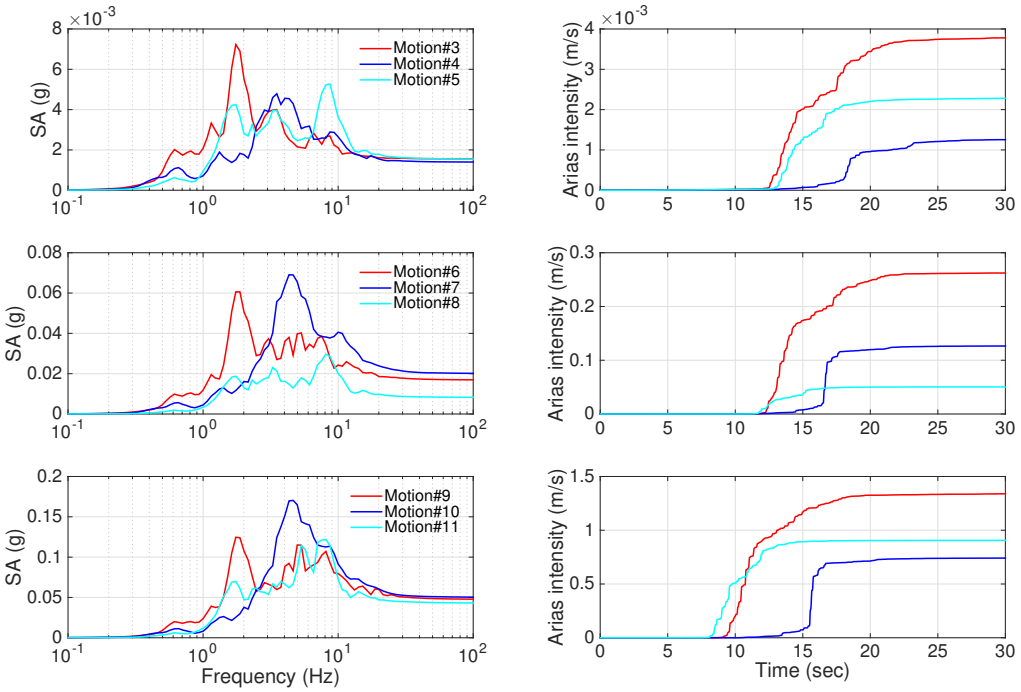

Figure 2.19: 5%-damped spectral acceleration and Arias intensity time series of the measured base motions for shake events #03 to #11.

Chapter 3

Data archiving and processing

3.1 Data archiving and interactive data report

Experimental data are often documented as static reports that present relevant metadata—such as model sketches, sensor lists, event sequences, etc.—and provide plots and tables of recorded data. Such reports provide guidance to researchers who wish to use the data, but the reports themselves do not provide any level of interaction that would enhance the utility of posted data.

The data report prepared for this project is an *interactive* report written up as a `Jupyter` notebook (e.g., Pérez and Granger, 2007) that is housed in `DesignSafe.ci` (Rathje et al., 2017), which is the repository that also houses the data. `Jupyter` notebooks combine code blocks, in which the data may be opened, processed, interrogated, and plotted, with markdown blocks that contain descriptions of the data. The text and figures in the report are written in HTML and co-exist with Python code that directly interacts with the experimental data. Specific innovative features of the data report include:

1. An interactive data plotter with which users can select a specific event from a drop-down menu, and subsequently plot data from any desired sensor. Users can also zoom and pan desired portions of the data and click to extract specific data points of importance (e.g., the maximum value of a specific data quantity). Users can also directly save a PNG file to their computer of any desired data plot.

2. An interactive model sketch, which is embedded as an `iframe` object linked to an Autodesk 360 drawing object. Users can zoom in and out to see various portions of the model configuration and can measure desired dimensions using the interactive tools.

3. Tables containing sensor lists, event sequences, etc., which are directly rendered from comma separated value files, and presented in HTML format using the jQuery javascript. This eliminates the potential for a mismatch between the data report and the table maintained by the research team.

The `Jupyter` notebook may be opened by any user with a `DesignSafe.ci` account to explore the dataset and may also be used as a template for users who wish to adapt it to their own datasets. A preview of the report is shown in Figure 3.1.

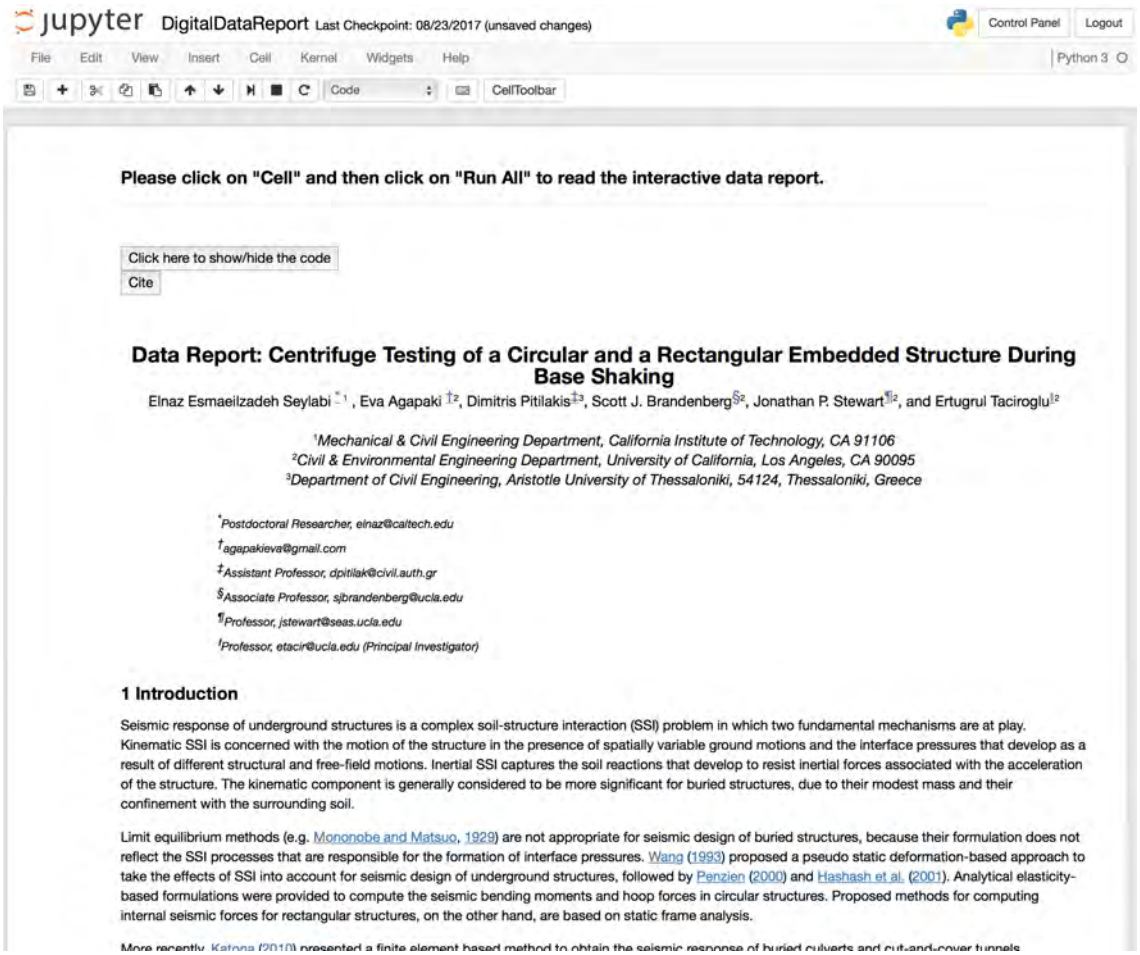

Figure 3.1: A preview of the interactive data report housed in `DesignSafe.ci`.

3.2 Data processing

3.2.1 Bender element signal processing

Shear wave velocity is obtained by measuring the travel time of the wave between two bender elements. The travel time between the two receivers in each elevation was used herein, because peripheral sources of phase-lag cancel each other when making receiver-to-receiver measurements, whereas they may cause errors in source-to-receiver measurements (Lee and Santamarina, 2005). Obtaining good quality signals in large centrifuge experiments is complicated because mechanical vibrations often have larger amplitudes than the shear waves generated by the bender elements. These vibrations are reduced by digital filtering and signal stacking to improve signal-to-noise ratio (Brandenberg et al., 2006), and occur predominantly at frequencies lower than the bender element signals.

Three basic approaches have been identified for determining the shear wave travel time: (*i*) observational techniques of the "start-to-start" and "peak-to-peak" signal in the source and receivers, (*ii*) cross-correlation (CC) of the signals, and (*iii*) a cross-power spectrum calculation of the signals (Yamashita et al., 2009). The last two approaches are techniques that are applied in time and frequency domains, respectively. The first technique involves visual selection of travel times, which is often subjective, particularly for source-to-receiver measurements. We apply the second (CC) technique to automate the travel time picks; and the continuous CC of two signals $x(t)$ and $y(t)$ can be computed as follows:

$$CC_{xy}(\tau) = \lim_{T\to\infty} \frac{1}{T} \int_0^T x(\tau)y(t+\tau)\mathrm{d}t \tag{3.1}$$

where T is the signal time record and $x(t)$ and $y(t)$ are two received signals.

A sample signal of the four arrays and the procedure we used to process it is given in Figure 3.2. Figure 3.2a shows the recorded signals from the two receiver benders for one of the four element arrays installed in our model for a dataset close to the step function pulse imposed. The signals were truncated to 2^N number of data points, so that a Fast Fourier Transform (FFT) could be performed. Four signals are plotted in Figure 3.2a, with two signals for each receiver bender element. The source bender element is pulsed with a positive step wave, then with a negative step wave and results for each are shown. High-amplitude, low-frequency noise is superposed on the bender element signals, because the centrifuge induces significant vibrations during spinning. Furthermore, the bender element voltages all exhibit a sudden increase when the source is excited due to electrical coupling. To reduce the influence of these factors, first the mean of positive and negative signals is computed for each bender element. Then, the initial portion of the signal associated with electrical coupling is truncated. Finally, the signals are baseline corrected by subtracting a seventh-order polynomial fit to the signal. The resulting post-processed signals used

for cross-correlation are shown in Figure 3.2c, and the cross-correlation versus time-lag is shown in Figure 3.2d. The travel time is taken as the time-lag associated with the peak of the absolute value of the cross-correlation. It is possible for the negative peak to be larger than the positive peak depending on the orientation of the bender elements, which was not recorded in these experiments.

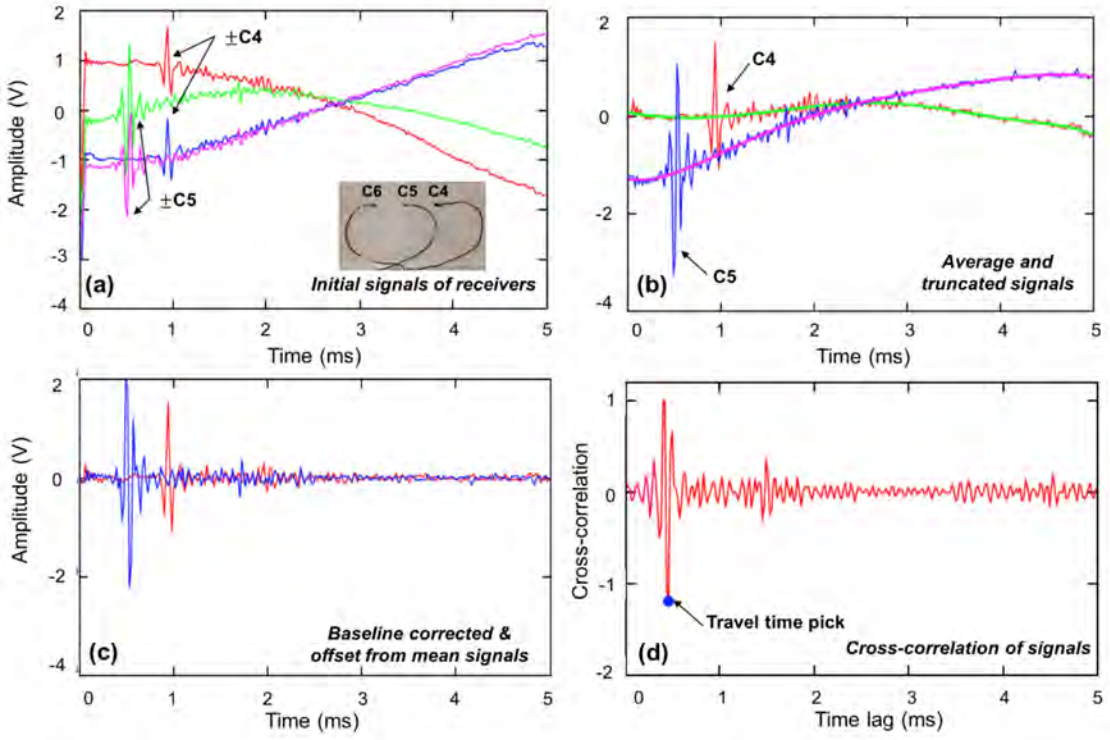

Figure 3.2: Example procedure to process bender element receivers' data (C4, C5) below the pipe (C-array).

The cross-correlation procedure cannot always produce accurate travel times when the two received signals differ due to wave dispersion, or when there are differences in the responses of the bender elements. Thus, *ad hoc* procedures are often required. For example, travel time for the array of bender elements located below the rectangular box (B array) was selected in the present study visually by observing the peak-to-peak travel time, because the peak in the cross-correlation signal did not correspond to the correct offset. Furthermore, the shallow free-field bender element array (MS array) required special attention, because the bender elements do not function as well at low confining pressures. In this case, the signals were processed by a cosine taper, and were filtered using a high-pass Butterworth filter in lieu of baseline correction.

Table 3.1 shows the obtained shear wave velocities at different depths of the container. Shear wave velocity is known to be a function of mean effective stress (σ'_m) (see, e.g., Hardin and Drnevich, 1970) for granular soils. Agapaki et al. (2016) regressed the data using three different functions, two of which were power laws that resulted in $V_s = 0$ at $\sigma'_m = 0$ (Hardin and Drnevich, 1970; Roesler, 1979), and the third was a form that permits $V_s > 0$ at $\sigma'_m = 0$. The regressions are illustrated in Figure 3.3. The form that best fits the data was given by

$$V_s(\text{m/s}) = 141.6 + 92.1 \left(\frac{\sigma'_m}{p_a} \right)^{0.35} . \tag{3.2}$$

where p_a is the atmospheric pressure.

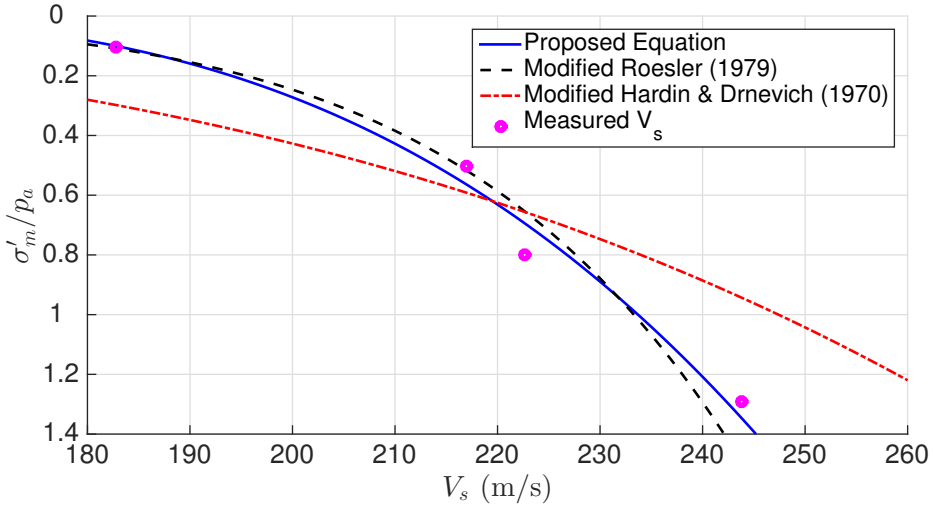

Figure 3.3: Relationship between V_s and σ'_m.

Table 3.1: Shear wave velocities obtained from bender element arrays' signal processing.

Bender element array	Depth ratio (z/H)	V_s (m/s)
Array MS	0.061	182.8
Array B	0.450	216.9
Array C	0.639	222.6
Array MB	0.797	243.8

3.2.2 Initial data processing

The initial data processing was performed in two steps. First, we determined the initial offset (or the reference points) of all the sensors. To achieve this, we used the signals recorded during the spin-up, prior to any base shaking, while the centrifugal acceleration was increased from 0 to about $N_g = 21g$. Plotting the measured signals against the total acceleration, i.e. $a_t = \sqrt{(N_g^2 + 1)}$, it was possible to extract the zero-crossing location of the fitted curve with $a_t = 0$, which was then taken as the initial offset for the measurement of that sensor. An example of the developed `Jupyter` notebook is shown in Figure 3.4 where a 3rd-order polynomial was fitted first, and was extrapolated to the data range of sensor BL7 (measuring bending strain on the box structure). After this first step, we truncated the measured signals to extract their meaningful portions for further signal processing and data interpretation. An screenshot of the developed `Jupyter` notebook is shown in Figure 3.5.

3.2.3 Processing of the acceleration signals

Generally, we needed to process acceleration time-series prior to data interpretation and numerical analyses. An screenshot of the developed `Jupyter` notebook for acceleration signal processing is shown in Figure 3.6. We considered three steps for acceleration signal processing:

1. Baseline correction: this was usually needed to remove constant, linear, or higher-order polynomial trends in the measured signals.
2. Tapering: this was needed to make sure that the measured signals tended to zero at the beginning and at the end of the time-series.
3. Filtering: this was needed to remove spurious frequencies from the measured signals. We used the band-pass Buttherworth filter in both forward and reverse directions to avoid altering the signals' phases.

As shown in Figure 3.6, the polynomial order, the period of the taper function, the orders of the bandpass filter and its associated frequencies can be defined by the user; and the processed data can be saved for further analysis.

3.2.4 Processing of the strain signals

For processing of the strain data, we considered the following steps:

1. Static offset: as shown in Figures 3.7 and 3.8, the signal time-series did not start from zero. This was because that the specimens deformed statically under the soil

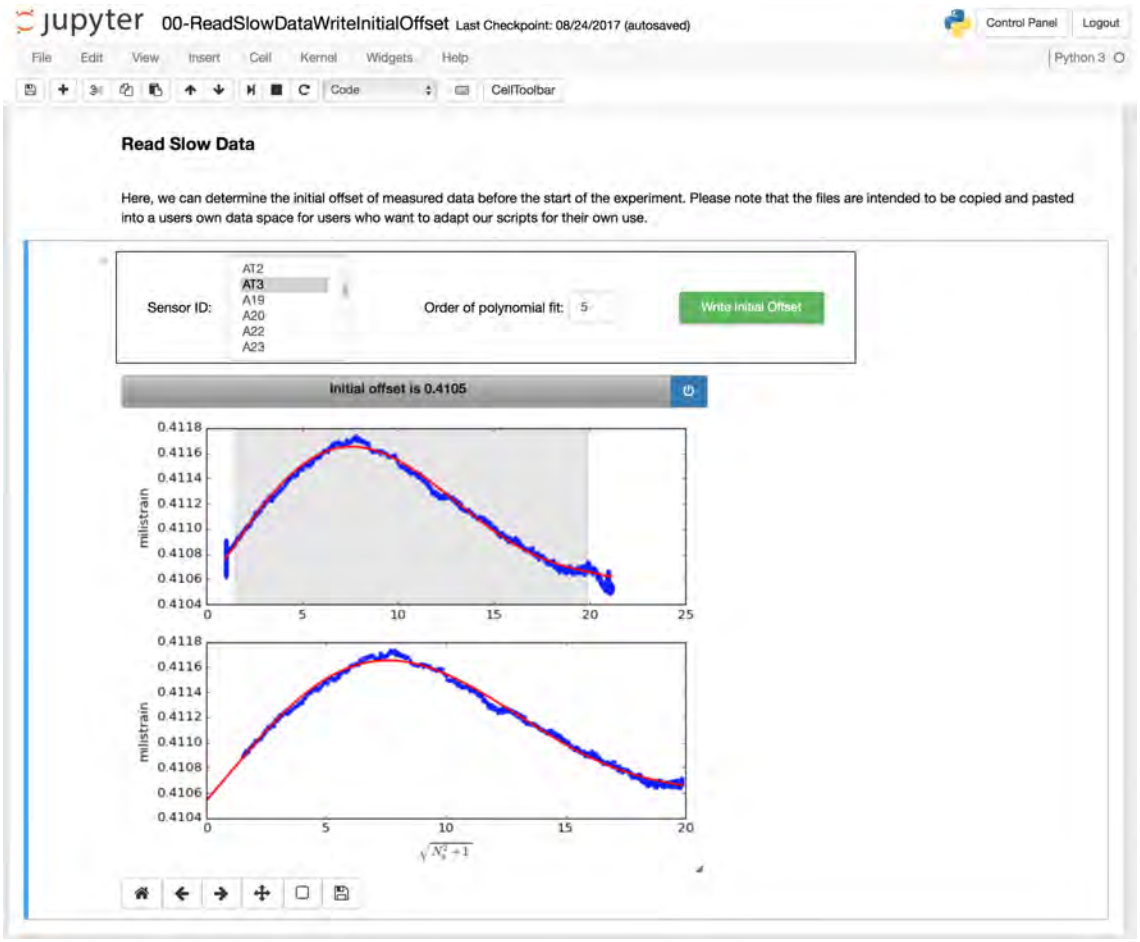

Figure 3.4: An screenshot of the developed `Jupyter` notebook for reading the sensor's initial offsets.

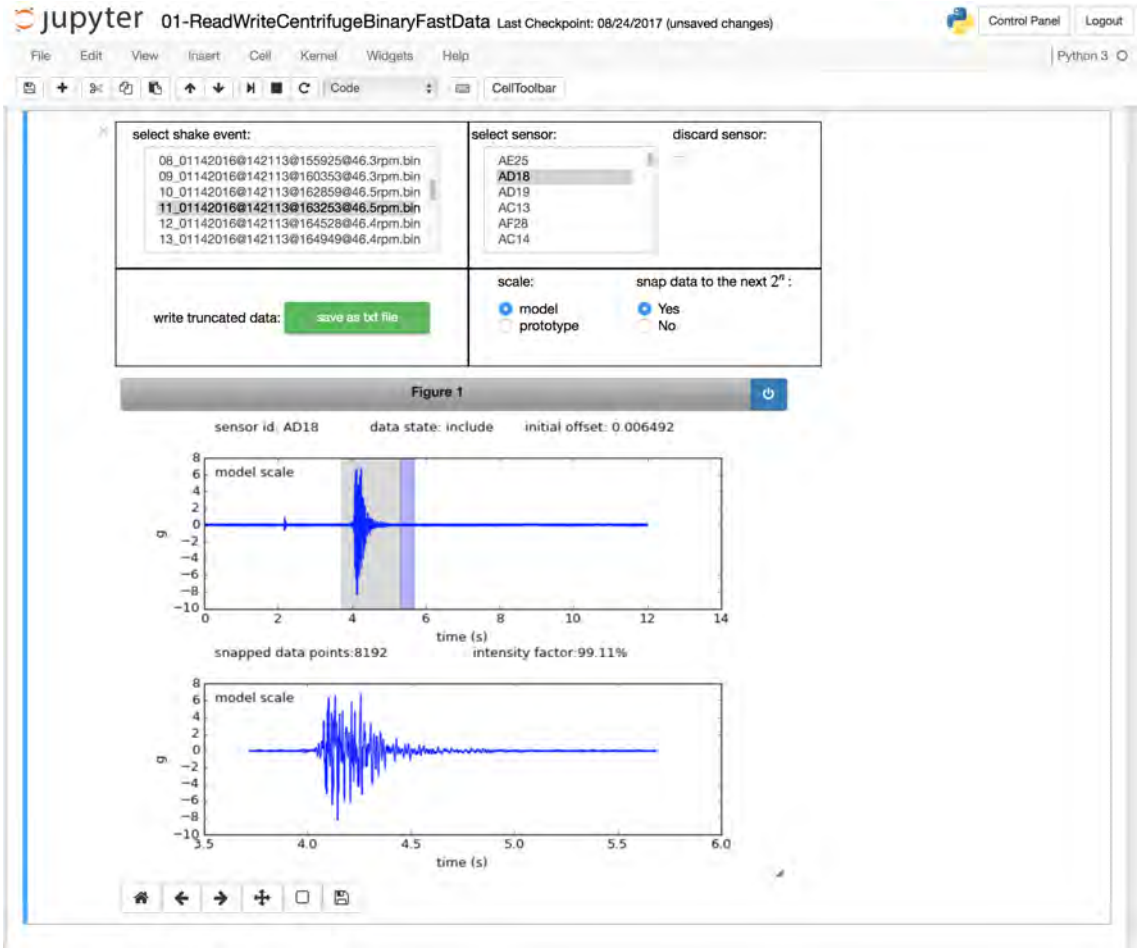

Figure 3.5: An screenshot of the developed `Jupyter` notebook for signal truncation.

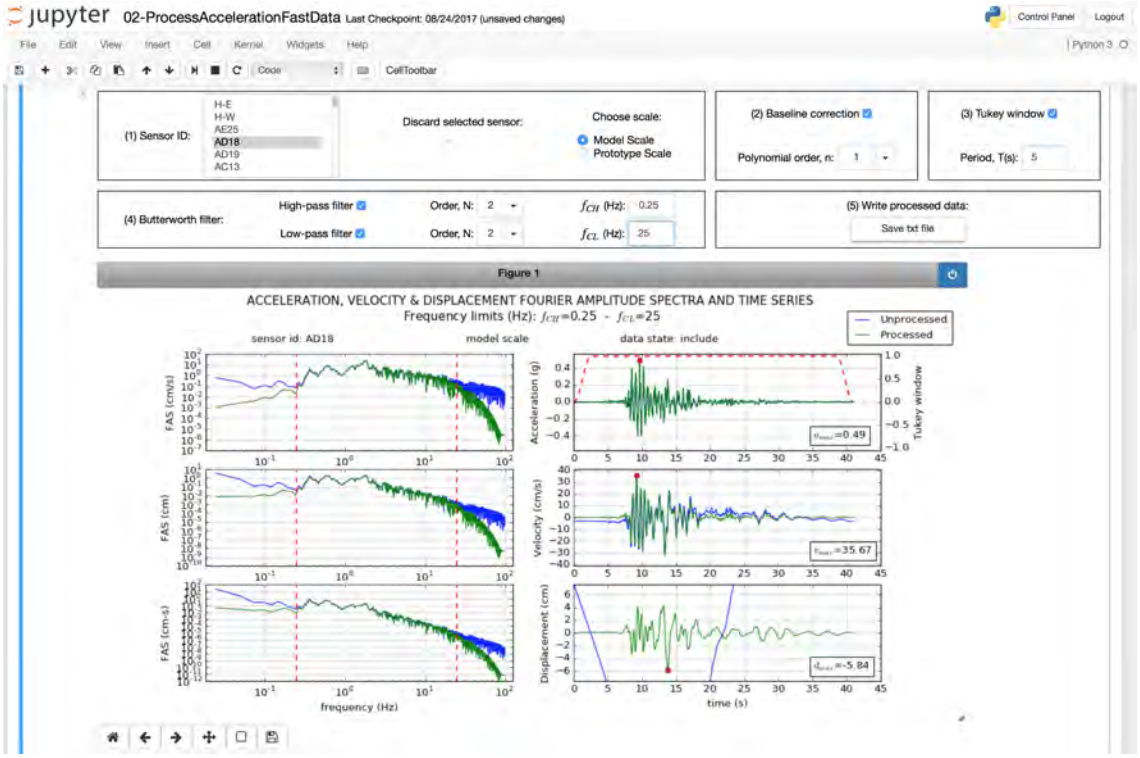

Figure 3.6: An screenshot of the developed `Jupyter` notebook for signal processing of acceleration time series.

overburden pressure, even when no base shaking was applied. In order to determine the static offset at the beginning of each strain signal, we computed the mean value of the first 100 data points as shown in the figures.

2. Linear detrending and tapering:We first removed the linear trend in the signal. This was done to consider only the dynamic increments in the signals (the underlying linear trend was probably due to unknown sensor drift, or physical compaction of soil). Then, we applied a taper function to make sure that the signal reaches zero at the beginning and at the end of the time-series.

3. Filtering: again, we applied a bandpass Buttherworth filter in both forward and reverse directions to the strain data. We set the corner frequencies as 0.25 and 25 Hz in prototype scale.

Application examples of the aforementioned steps on strain data are shown in Figures 3.7 and 3.8.

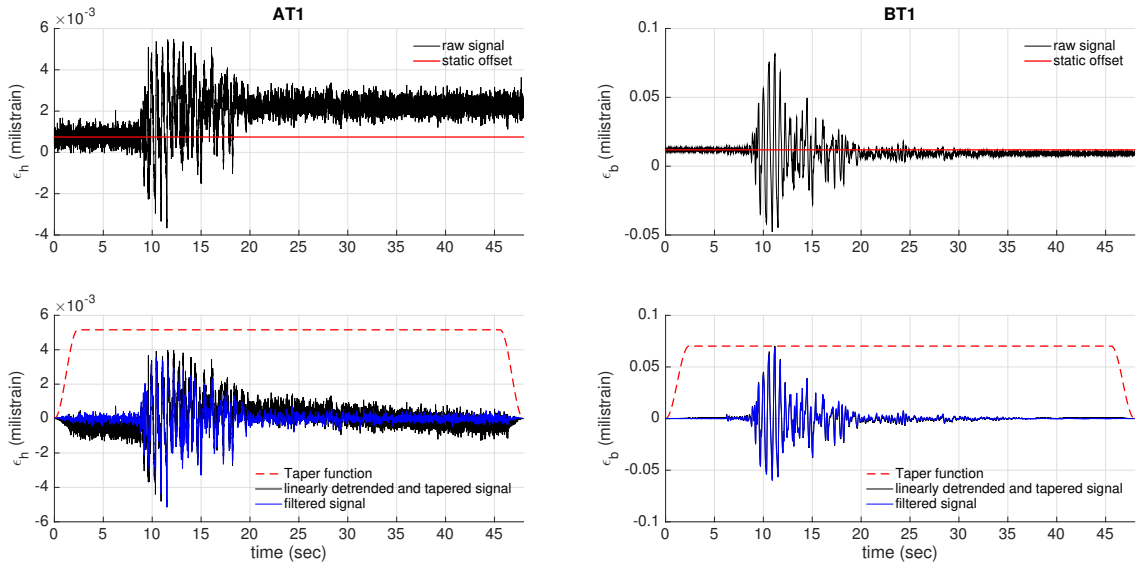

(a) Axial strain

(b) Bending strain

Figure 3.7: An example of strain signal processing performed on signals recorded on the rectangular structure during base shaking #9.

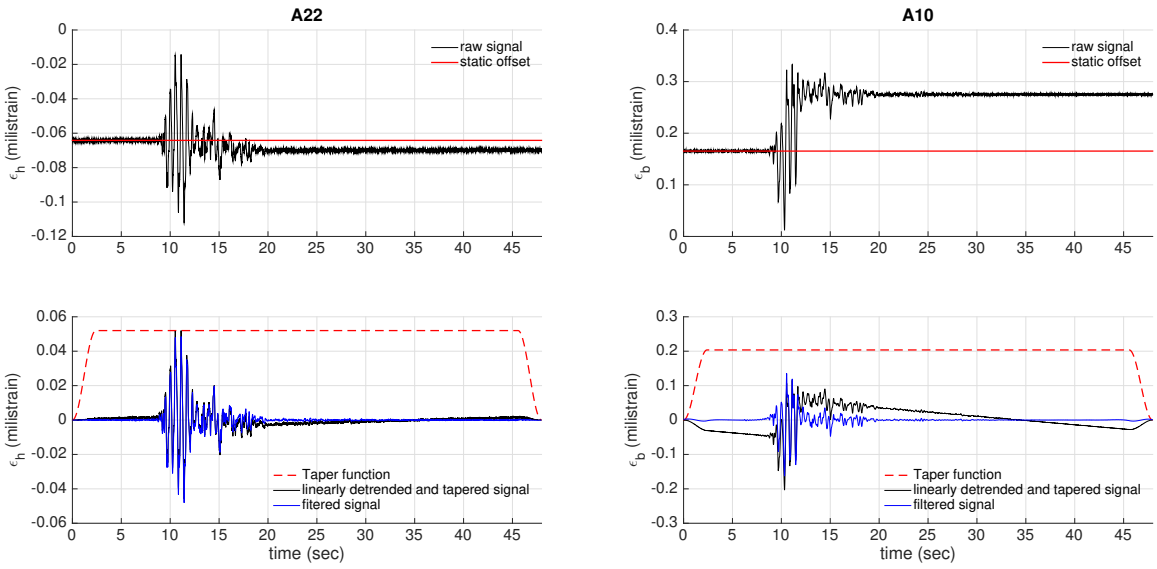

(a) Axial strain

(b) Bending strain

Figure 3.8: An example of strain signal processing performed on signals recorded on the circular structure during base shaking #9.

Chapter 4

The NCHRP 611 approach

The current AASHTO LRFD Bridge Design Specifications do not cover the seismic response of buried structures; and only the recent National Cooperative Highway Research Program (NCHRP) Report 611—titled "Seismic Analysis and Design of Retaining Walls, Buried Structures, Slopes, and Embankments"—offers various recommendations on the topic. As culvert structures in transportation applications generally have a limited length, their potential failure modes are due to their transverse deformations under transient ground shaking—namely, ovaling and racking of circular and rectangular culverts, respectively (Anderson et al., 2008)—, which are illustrated in Figure 4.1.

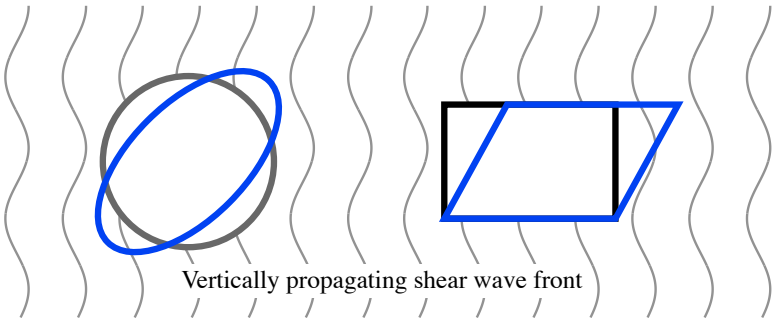

Figure 4.1: Ovaling and racking deformation of the circular and rectangular cross sections.

4.1 Ovaling of a circular culvert

It is widely accepted that plane strain models provide reasonable approximations to the failure modes of circular culverts, as their most critical mode is the ovaling deformation

mode (Kontoe et al., 2014). Transient ovaling effects in circular culverts can be quantified by the change in their diameters, which can then be used to obtain reasonable estimates of the peak seismically induced internal forces. For flexible culverts, buckling is the most critical failure mode, which is governed by the thrust force. For rigid culverts, on the other hand, the lining deformation, bending, thrust, and the resulting strains are all important parameters to evaluate (Anderson et al., 2008).

Currently, four analytical closed-form solutions are available (Wang, 1993b; Penzien, 2000a; Park et al., 2009; Bobet, 2010), which are all based on the assumption that, under seismic loading, the tunnel lining acts as an elastic beam subject to a uniform shear strain field of amplitude $\gamma_{\max}$, wherein the inertial soil-lining interaction effects are ignored. As enumerated by Kontoe et al. (2014), the dynamic interaction can become important when (i) the dimensions of the tunnel cross-section is comparable to the wavelengths of the seismic loading, (ii) the tunnel is relatively shallow, and (iii) the structure is significantly stiffer than the surrounding soil.

The methodology provided in NCHRP Report 611 (Anderson et al., 2008) is based on the solution provided by Wang (1993b). An engineer needs to execute the following steps to determine the seismic demands due to ovaling of the circular culvert:

1. *Estimate the free-field ground strains (γ_{max}) at the top and bottom elevations of the culvert structure*: For highway culverts with burial depths less than 50 ft, γ_{max} may be estimated using the equation below:

$$\gamma_{max} = \frac{\tau_{max}}{G_m}, \quad \tau_{max} = (\text{PGA}/g)\sigma_v R_d \tag{4.1}$$

   where G_m is the effective-strain-compatible shear modulus of the surrounding soil, PGA is the peak ground acceleration, σ_v is the overburden pressure at the depth corresponding to the invert of the culvert, and R_d is a depth-dependent stress reduction factor given by

$$R_d = \begin{cases} 1 - 0.00233z & z < 30\text{ft} \\ 1.174 - 0.00814z & 30\text{ft} \leq z \leq 75\text{ft} \end{cases} \tag{4.2}$$

   and z is the depth to the midpoint of the culvert. One may also estimate γ_{max} by performing free-field site response analysis.

2. *Calculate of the flexibility and compressibility ratios*: Compressibility ($C^{\bigcirc}$) and flexibility ($F^{\bigcirc}$) ratios are used to determine the relative stiffness of the culvert lining with respect to the surrounding ground (Wang, 1993b), and can be computed as:

$$F^{\bigcirc} = \frac{E_m(1-\nu_1^2)R^3}{6E_1I_1(1+\nu_m)} \tag{4.3}$$

$$C^{\bigcirc} = \frac{E_m(1-\nu_1^2)R}{E_1A_1(1+\nu_m)(1-2\nu_m)} \tag{4.4}$$

where E_m is the strain-compatible elastic modulus, and ν_m is the Poisson's ratio of the surrounding soil. The terms R, E_1, ν_1, A_1, t and I_1 respectively denote nominal radius, elastic modulus, Poisson's ratio, cross-sectional area, thickness, and moment of inertia of the culvert lining. For $F^{\bigcirc} < 1$, the lining is considered to be stiffer than the surrounding soil while for $F^{\bigcirc} > 1$, it is expected that the lining deforms more than the free-field.

3. *Estimate the lining deformation and seismic demands*: For estimation of the lining diameter change (ΔD_{EQ}) and the resulting moment (M), it is recommended to consider a full-slip interface assumption, which allows normal stresses without normal separation and tangential forces. On the other hand, for estimation of the resulting thrust (T), a no-slip interface assumption is recommended. Therefore,

$$\Delta D_{\mathrm{EQ}} = \pm\frac{1}{3} k_1 F^{\bigcirc} \gamma_{\max} D \tag{4.5}$$

$$M^{\bigcirc} = -\frac{1}{6} k_1 \frac{E_m}{1+\nu_m} R^2 \gamma_{\max} \cos 2(\theta + \frac{\pi}{4}) \quad \text{(full-slip)} \tag{4.6}$$

$$T^{\bigcirc} = -k_2 \frac{E_m}{2(1+\nu_m)} R \gamma_{\max} \cos 2(\theta + \frac{\pi}{4}) \quad \text{(no-slip)} \tag{4.7}$$

where

$$k_1 = 12 \frac{1-\nu_m}{2F^{\bigcirc} + 5 - 6\nu_m}\,, \tag{4.8}$$

$$k_2 = 1 + \frac{F^{\bigcirc}(1-2\nu_m)(1-C^{\bigcirc}) - 0.5(1-2\nu_m)^2 C^{\bigcirc} + 2}{F^{\bigcirc}[(3-2\nu_m) + (1-2\nu_m)C^{\bigcirc}] + C^{\bigcirc}[2.5 - 8\nu_m + 6\nu_m^2] + 6 - 8\nu_m}\,. \tag{4.9}$$

4.2 Racking of a rectangular culvert

Contrary to circular culverts, no closed form solution is available for quantifying the racking deformations in rectangular culverts. The procedure provided in NCHRP Report 611 is based on the pseudo-static method proposed by Wang (1993b), which again does not take inertial interaction effects into account. The following steps are recommended therein to estimate the seismic demands due to racking of a rectangular culvert.

1. *Estimate of the free-field ground strains (γ_{max}) at the elevation of the culvert structure*: γ_{max} can be computed following the procedure provided for circular culverts in §4.1.

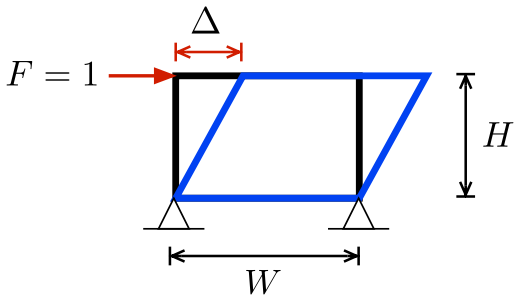

Figure 4.2: Racking stiffness of the rectangular culvert.

2. *Estimate the differential free-field relative displacement* ($\Delta_{\text{freefield}}$) *at the corresponding top and bottom elevations of the rectangular structure.* That is:

$$\Delta_{\text{freefield}} = H\gamma_{max} \tag{4.10}$$

where H is the height of the structure. As seen in Equation (4.10), it is assumed that the racking is due to a uniform shear strain field. This assumption is the same as that used for ovaling of circular culverts.

3. *Calculate the racking stiffness* (K_s) *of the structure*: This value can be computed through a simple structural frame analysis by applying a unit horizontal force at the roof of the structure, while its base is restrained as shown in Figure 4.2 and reading the resulting lateral displacement Δ. That is,

$$K_s = \frac{1}{\Delta}. \tag{4.11}$$

4. *Calculate the flexibility ratio*: The flexibility ratio $F^{\square}$ is the measure of the relative stiffness of the structure to the surrounding soil and can be estimated as follows.

$$F^{\square} = \frac{G_m}{K_s}\frac{W}{H} \tag{4.12}$$

where W is the width of the culvert structure as shown in Figure 4.2.

5. *Estimate the racking ratio*: The racking ratio $R^{\square}$ determines the ratio of the actual racking deformation of the structure with respect to the free-field racking deformation of the surrounding soil and can be defined as:

$$R^{\square} = \frac{2F^{\square}}{1 + F^{\square}}\,. \tag{4.13}$$

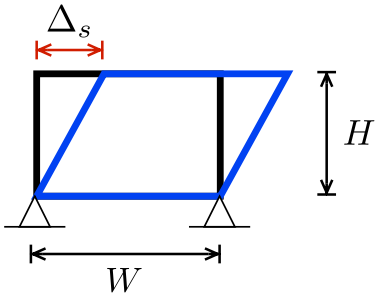

Figure 4.3: Imposition of the racking displacement to determine the resulting internal forces and moments from structural frame analysis.

6. *Estimate the racking deformation of the structure*: Using the racking ratio and the free-field relative displacements, the racking deformation Δ_s can be computed as follows:

$$\Delta_s = R^{\square} \Delta_{\text{freefield}} \,. \tag{4.14}$$

7. *Determine the seismic demands*: Internal forces and the resulting strains can be computed by imposing the racking deformation at the roof of the structure as shown in Figure 4.3, and by performing a structural frame analysis.

Chapter 5

Comparison of centrifuge results with the NCHRP 611 method

In this chapter, comparisons of seismic demands obtained from centrifuge test data with those calculated using the NCHRP 611 method (see Chapter 4) are presented.

5.1 NCHRP 611 method

In order to compute seismic demands using the NCHRP 611 methodology, we first need to estimate the free field maximum strain γ_{max} in the soil deposit as well as the corresponding effective compatible shear modulus G_m. Then, the seismic demands can be computed following the steps outlined in Chapter 4.

5.1.1 Estimation of G_m at the elevation of the culvert structures

In Chapter 3, we provided details of a signal processing procedure for obtaining shear wave velocities at different elevations of the soil deposit inside the container using bender element sensors. Esmaeilzadeh Seylabi et al. (2018) also used a Bayesian approach to infer the shear wave velocity profile using data measured by the far-field accelerometer array {AA1,AC12,AD18,AE25,AF28} during low-amplitude earthquake motions (i.e., motions #3, #4, and #5) with maximum input acceleration of $\sim 0.015g$. The resulting estimated shear wave velocity profile was given as,

$$V_s \text{ (m/s)} = 16.905 + 192.976 \left(\frac{z}{H}\right)^{0.331}, \tag{5.1}$$

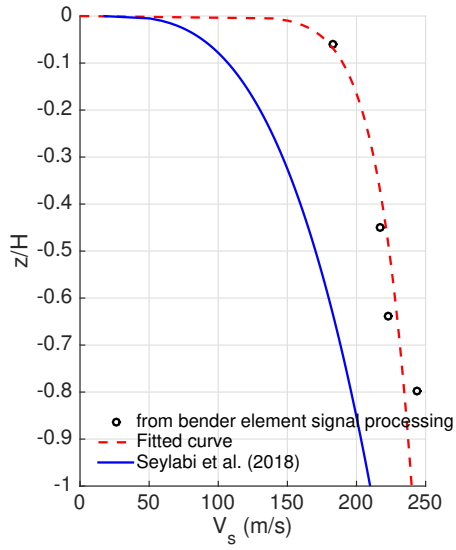

Figure 5.1: Shear wave velocity profile obtained from post-processing of the bender element signals and from a Bayesian estimation method.

which is shown in Figure 5.1 along with the curve fitted through the data points obtained from bender element signal processing. As it will be shown in Chapter 6, using this new shear wave velocity profile will result in acceleration responses that are highly correlated with experimentally recorded ones. Therefore, in the subsequent analyses, we will use Equation (5.1) for computing the shear wave velocity associated with small soil strains. Then, one may also compute the maximum shear modulus G_{max} as follows:

$$G_{max} = \rho V_s^2 \tag{5.2}$$

where ρ is the density of the soil deposit, which is equal to 1733 kg/m^3 for the present case.

The maximum shear modulus may be an appropriate representation of G_m for only low-amplitude motions for which the soil nonlinearity is negligible and the shear strains are very small (i.e., $\sim 10^{-5}$). Therefore, we also need to use a representative modulus reduction curve along with the computed G_{max} to estimate the effective strain compatible shear modulus G_m at elevations of the tested culvert structures. Based on available soil properties for the Ottawa sand, one may use the empirical equations given by Menq (2003) to estimate the modulus reduction curve. That is,

$$\frac{G}{G_{max}} = \frac{1}{1 + (\gamma/\gamma_r)^a} \tag{5.3}$$

where

$$\gamma_r = 0.12 C_u^{-0.6} \left(\frac{\sigma'_m}{p_a}\right)^{0.5 C_u^{-0.15}}, \qquad a = 0.86 + 0.1 \log\left(\frac{\sigma'_m}{p_a}\right) \tag{5.4}$$

and C_u is the coefficient of uniformity, which, for Ottawa sand, is equal to 1.73. In order to decrease the uncertainties emanating from the use of empirical equations, Esmaeilzadeh Seylabi et al. (2018) used an approach to estimate the modulus reduction curve from far-field acceleration data, which was similar to what was used for inferring the shear wave velocities from the same data. A multi-axial cyclic plasticity model by Borja et al. (2000) was used to model the nonlinear/inelastic behavior of the soil deposit. The mean value of the estimated soil model parameters are as follows [1].

$$h = \left[0.107 + 0.474 \left(\frac{z}{H}\right)^{4.581}\right] G_{\max},\ m = 1.579,\ R = 0.0028\ G_{\max},\ H_0 = 0\,, \tag{5.5}$$

Figure 5.2 displays the resulting modulus reduction curves from both approaches at the elevations of the rectangular and circular structures. Finally, with using the estimated G/G_{max} curves and the G_{max} profile, we can compute the effective-strain-compatible shear modulus G_m for a given maximum shear strain in each event.

5.1.2 Estimation of γ_{max} at the elevation of the culvert structures

For shallow structures one may use the procedure provided in Chapter 4 to estimate γ_{max}. However, in order to use that procedure, we need to know the effective compatible shear modulus G_m, which itself is a function of γ_{max}. Therefore, in order to use the NCHRP 611 method, we need to obtain it iteratively as follows:

1. To start the procedure (iteration $i = 0$), we need to have initial guesses for the maximum shear strains at the elevation of the rectangular and circular culverts. In order to compute the maximum strain at the elevation of the rectangular culvert, i.e. $\gamma^{\square}_{max,0}$, we use the acceleration measurements at AF28 and AE25, which correspond to the elevations at the roof and invert levels of the culvert. The displacement responses at these elevations can be computed by double integration of the acceleration time-series. Then, the relative free-field displacement history $\Delta u^{\square}_{\text{free-field}}$ can be computed as follows.

$$\Delta u^{\square}_{\text{free-field}}(t) = u^{\text{AF28}}(t) - u^{\text{AE25}}(t)\,. \tag{5.6}$$

[1] Details of the nonlinear soil model and definitions of its parameters are provided later in Chapter 6. It should also be noted here that our prior studies on centrifuge experiments involving structures embedded in dry sands have demonstrated that this soil model exhibits very good performance in predicting the main features of soil and embedded structure responses under broadband/seismic excitations (Zhang et al., 2017).

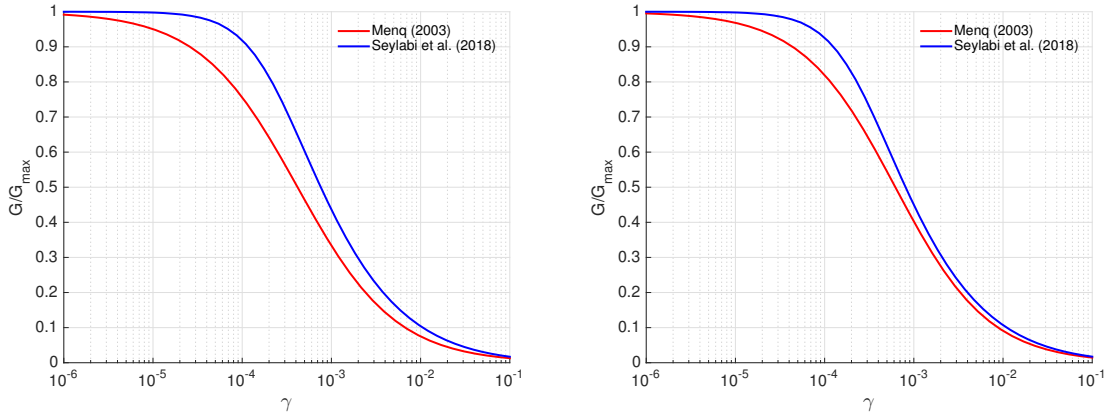

(a) At the elevation of the rectangular culvert, $z/H = 0.19$

(b) At the elevation of the circular culvert, $z/H = 0.46$

Figure 5.2: Shear modulus reduction curves obtained from the empirical equations by (Menq, 2003) and from the Bayesian estimation (Esmaeilzadeh Seylabi et al., 2018) at the elevations of the rectangular and circular culvert structures.

Since NCHRP 611 considers the purely uniform shear in estimation of the seismic demands, $\gamma^{\square}_{max,0}$ can be computed dividing the maximum relative free-field displacement, i.e. $\Delta^{\square}_{\text{free-field}}$, by the height of the culvert structure H. That is,

$$\gamma^{\square}_{max,0} = \frac{\Delta^{\square}_{\text{free-field}}}{H} \,. \tag{5.7}$$

For the circular culvert, we use the acceleration measurements at AE27 and AC17 to determine the relative free-field displacement at the elevation of the structure. That is,

$$\Delta u^{\bigcirc}_{\text{free-field}}(t) = u^{\text{AE27}}(t) - u^{\text{AC17}}(t) \,. \tag{5.8}$$

Again, the maximum strain at the elevation of the circular culvert can be computed by dividing the maximum relative free-field displacement $\Delta^{\bigcirc}_{\text{free-field}}$ by the height (diameter) of the structure D. Therefore,

$$\gamma^{\bigcirc}_{max,0} = \frac{\Delta^{\bigcirc}_{\text{free-field}}}{D} \,. \tag{5.9}$$

2. For iteration i, we can predict G_m for the rectangular and circular culverts using $\gamma_{max,i-1}$ and Figure 5.2. Then, we can correct the maximum shear strain $\gamma_{max,i}$ using Equation 4.1.

3. We need to repeat step 2 until $|\gamma_{max,i} - \gamma_{max,i-1}| <= \text{TOL}$ for the predefined tolerance TOL.

Figures 5.3, 5.4 and 5.5 show the iterative procedure for base shakings #3, #6, and #9, respectively. The resulting maximum shear strains are also tabulated in Table 5.1. As shown, in all cases the use of the iterative procedure results in higher maximum shear strains compared to those obtained from dividing the relative free field displacements at elevations of the rectangular and circular structures by the height of the structure.

As mentioned before, NCHRP 611 also suggests using 1D site response analysis to compute the maximum shear strain. In order to investigate the accuracy of NCHRP 611 equations against this refined procedure, we performed 1D wave propagation analysis, using the multiaxial cyclic plasticity model. The resulting maximum strain profiles for all nine input motions are shown in Figure 5.6 and the strain values at elevations of the culverts are provided in Table 5.1 (i.e., $\gamma^{\square}_{max,1D}$ and $\gamma^{\bigcirc}_{max,1D}$). As shown, the shear profile is not constant with depth (especially for medium and high amplitude motions) and its curvature is a function of soil behavior and input motion characteristics. Moreover, the values of maximum strain obtained from 1D wave propagation analysis are considerably smaller than those obtained from the iterative procedure and are close to those obtained from the experimental data (i.e., our initial guesses for the iterative procedure). The effect of this difference will be studied in the subsequent sections.

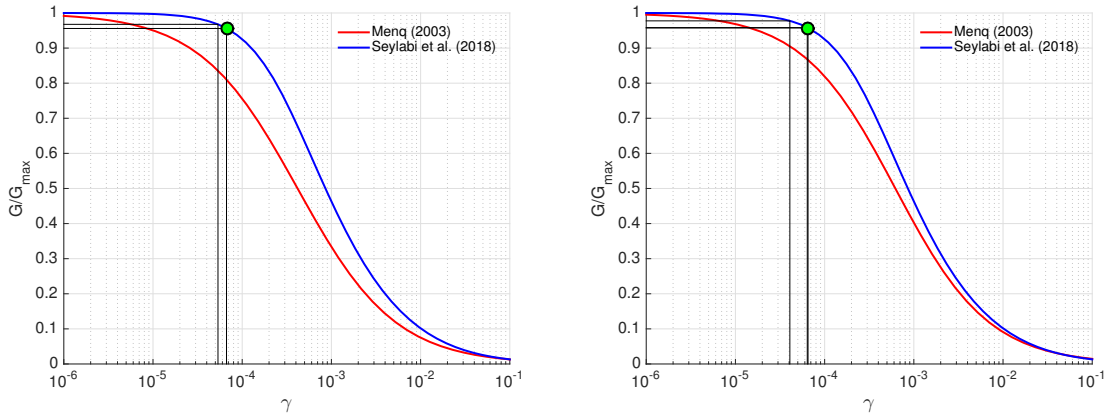

(a) At the elevation of the rectangular structure

(b) At the elevation of the circular structure

Figure 5.3: Iterations for computing γ_{max} at the elevation of the rectangular and circular structures when subjected to the base shaking #3.

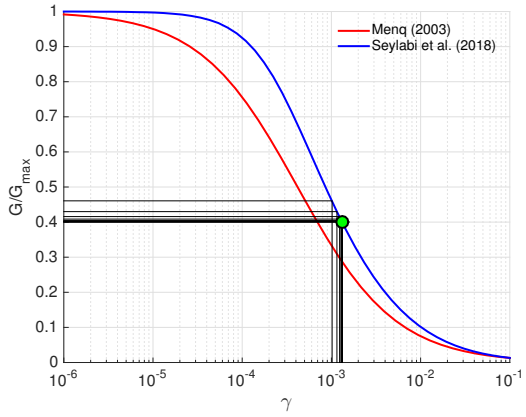

(a) At the elevation of the rectangular structure

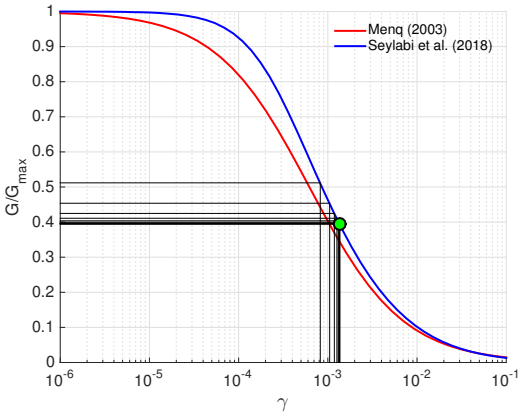

(b) At the elevation of the circular structure

Figure 5.4: Iterations for computing γ_{max} at the elevation of the rectangular and circular structures when subjected to the base shaking #6.

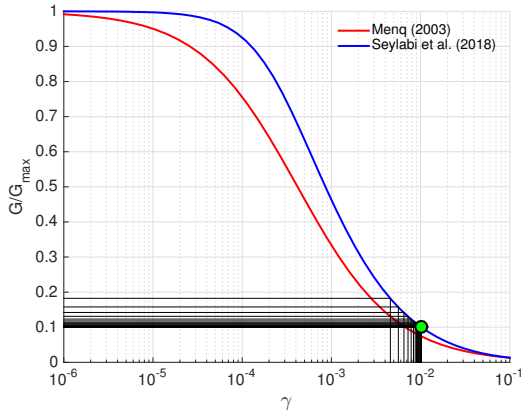

(a) At the elevation of the rectangular structure

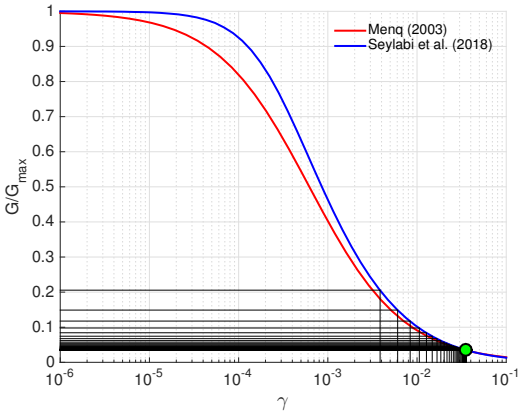

(b) At the elevation of the circular structure

Figure 5.5: Iterations for computing γ_{max} at the elevation of the rectangular and circular structures when subjected to the base shaking #9.

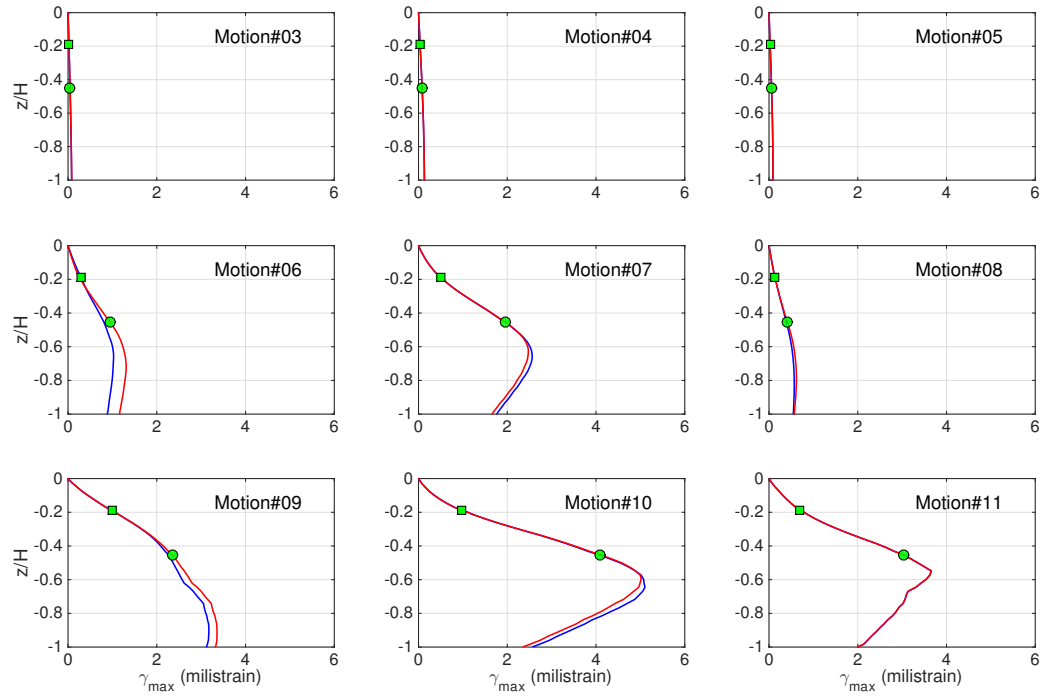

Figure 5.6: Maximum shear strain profile obtained from 1D wave propagation analyses.

Table 5.1: The computed maximum free field shear strains at the elevation of the rectangular and circular structures.

Motion #	$\gamma^{\square}_{max,0}$ (milistrain)	$\gamma^{\square}_{max}$ (milistrain)	$\gamma^{\square}_{max,1D}$ (milistrain)	$\gamma^{\bigcirc}_{max,0}$ (milistrain)	$\gamma^{\bigcirc}_{max}$ (milistrain)	$\gamma^{\bigcirc}_{max,1D}$ (milistrain)
3	0.054	0.067	0.020	0.041	0.066	0.046
4	0.092	0.127	0.036	0.075	0.124	0.082
5	0.061	0.086	0.025	0.043	0.080	0.059
6	1.019	1.495	0.298	0.823	1.504	0.943
7	1.235	1.882	0.497	1.082	2.477	1.950
8	0.381	0.612	0.138	0.313	0.815	0.412
9	4.580	9.108	0.993	3.855	18.181	2.355
10	3.553	16.993	0.983	2.508	7.022	4.088
11	2.156	8.280	0.702	1.702	7.660	3.039

5.1.3 Seismic strains of the rectangular culvert

As mentioned in Chapter 4, for determination of the flexibility ratio, we need to compute the racking stiffness K_s. To this end, we modeled the rectangular structure in ANSYS and analyzed it under the unit horizontal force. This resulted in $K_s = 26882$ kN/m. We consider W and H to be equal to 4.3 m and 2.7 m, respectively, in prototype scale. After computing the flexibility and racking ratios, we can compute the resulting racking displacement and impose it on top of the structure to obtain internal forces and moments from a simple frame analysis. We performed this analysis in ANSYS.

5.1.4 Seismic strains of the circular culvert

As mentioned in Chapter 4, we first need to determine the flexibility and compressibility ratios to determine the internal forces in the circular culvert (see Equations 4.3 and 4.4). After obtaining G_m, one can compute the effective-strain-compatible Young's modulus of the surrounding soil using the following equation

$$E_m = 2G_m(1 + \nu_m) \tag{5.10}$$

where ν_m is the Poisson's ratio of the soil and is equal to 0.3 for the present case. I_1 and A_1 are the moment of inertia and area of the cross-section, and are equal to $1/12t_1^3$ and t_1, respectively, for the unit length of the circular culvert with the thickness of t_1. After the determination of $F^{\bigcirc}$ and $C^{\bigcirc}$, we can calculate the internal forces and the resulting strains for each test. In-plane bending strain ($\epsilon_b^{\bigcirc}$) and in-plane axial (hoop) strain ($\epsilon_h^{\bigcirc}$) are related to the internal bending ($M^{\bigcirc}$) and thrust ($T^{\bigcirc}$) as follows:

$$\epsilon_b^{\bigcirc} = \frac{M^{\bigcirc} t_1}{2E_1 I_1}, \quad \epsilon_h^{\bigcirc} = \frac{T^{\bigcirc}}{A_1}\,. \tag{5.11}$$

5.2 Static and dynamic increments of measured strains

As mentioned in Chapter 2, we use the full bridge arrangement to measure the in-plane bending and in-plane axial strains at different points along the edges of the structures. Prior to interpretation and comparisons, the strain data need to be processed, the procedural details of which are provided in §3.2.4 of Chapter 3.

In the following sections, we provide the strain results for both the static offset at the beginning of each base shaking and the corresponding dynamic increment. It should be noted that for the rectangular structure, the results for only the bending strains are provided. This is mainly because the recorded in-plane axial strains were too small, even for the large amplitude motions (see Figure 3.7).

5.3 Comparison of the in-plane bending strains for the rectangular culvert

In order to compare the experimental bending strain data against those computed using the NCHRP 611 method, we need to obtain the maximum bending strain profiles. To this end, we use the processed strain data from each event to determine the maximum bending strain among all recorded bending strains on the rectangular structure as well as the time it occurs. Then, we read the value of bending strains at *all* locations at the time that the maximum bending strain has occurred. Figure 5.8 displays the bending strain comparisons for each base shaking. In each sub-figure, the static offset of the experimental strains at the beginning of the shaking is shown on the left. On the other hand, the maximum dynamic increment (red bars) along with those obtained from the NCHRP 611 method (blue bars) are shown on the right. It should be noted that different scaling factors are used among different events. Therefore, these figures provide only a qualitative understanding of differences between the experimental data and the NCHRP 611 analysis results.

In order to compare the actual bending strain values, we compute the maximum bending strain for each event. Table 5.2 summarizes the values of the important parameters including the flexibility and racking ratios, and the maximum bending strains. We observe that:

- The application sequence of base shakings had negligible effects on the maximum value of the static strain offset. However, the static offset profile has slightly changed (specifically, along the invert and bottom sides of the culvert walls).
- Since the box structure remained elastic, $F^{\square}$ is proportional to G_m. Therefore, as the surrounding soil becomes softer, the flexibility ratio—and therefore the racking ratio—decreases.
- In all cases, the NCHRP 611 method overestimates the maximum bending strain.
- The experimental bending strain profiles along the walls, roof, and invert vary almost linearly, and conform to the bending strain profile obtained from static frame analysis.

In order to have a closer look at how the maximum bending strain is related to different parameters of interest (PoIs), we plot each PoI against the maximum bending strains obtained from the centrifuge data directly, and the NCHRP method. This is shown in Figure 5.7. Although the range of $\epsilon_b^{\text{Centrifuge}}$ is different from the range of $\epsilon_b^{\text{NCHRP}}$, visually they both follow similar trends, especially with respect to γ_{max} and R.

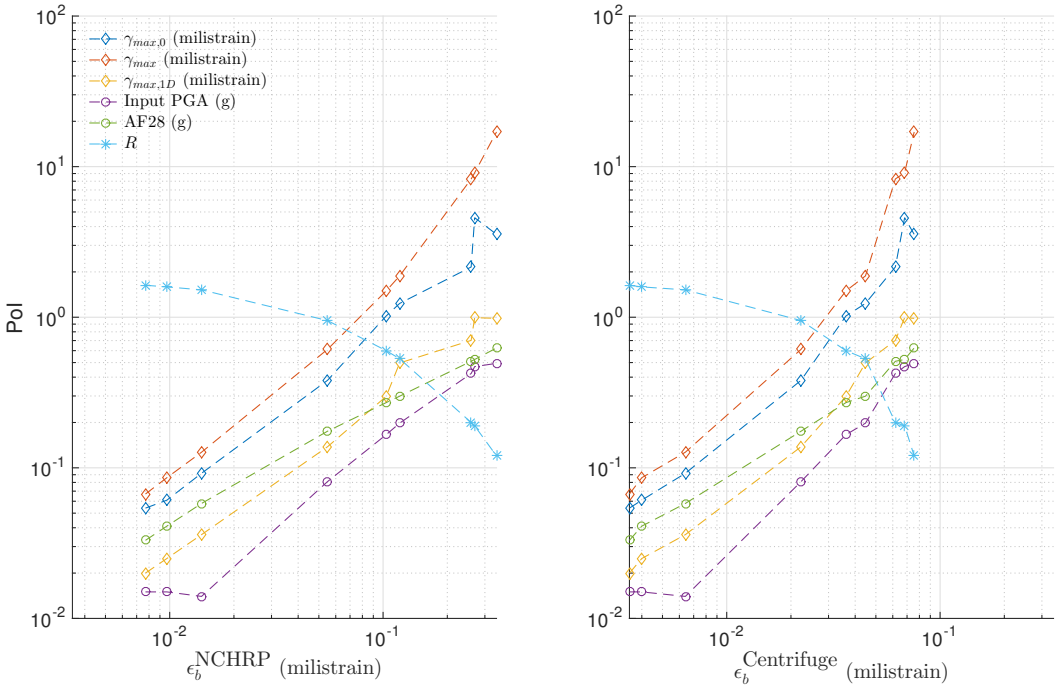

Figure 5.7: Variation of different PoIs with maximum bending strain of the rectangular structure.

Table 5.2: Comparison of the maximum bending strains of the rectangular structure.

Motion #	Input (g)	AF28 (g)	G_m/G_{max}	V_s (m/s)	$\gamma^{\square}_{max}$ (milistrain)	$F^{\square}$	$R^{\square}$	$\epsilon^{\square}_b$ (milistrain) NCHRP	$\epsilon^{\square}_b$ (milistrain) Centrifuge, Static	$\epsilon^{\square}_b$ (milistrain) Centrifuge, Dynamic	$e_b^{\text{NCHRP}}/e_b^{\text{Centrifuge}}$
3	0.015	0.033	0.954	125.8	0.07	1.63	1.24	0.0077	0.0337	0.0035	2.17
4	0.014	0.058	0.890	121.6	0.13	1.52	1.21	0.0141	0.0335	0.0064	2.21
5	0.015	0.041	0.934	124.5	0.09	1.59	1.23	0.0097	0.0334	0.0040	2.42
6	0.166	0.271	0.352	76.5	1.50	0.60	0.75	0.1034	0.0334	0.0362	2.86
7	0.198	0.299	0.309	71.6	1.88	0.53	0.69	0.1196	0.0328	0.0447	2.68
8	0.081	0.175	0.555	96.0	0.61	0.95	0.97	0.0549	0.0325	0.0223	2.46
9	0.470	0.524	0.112	43.1	9.11	0.19	0.32	0.2687	0.0324	0.0682	3.94
10	0.494	0.625	0.071	34.4	16.99	0.12	0.22	0.3401	0.0332	0.0756	4.50
11	0.423	0.510	0.120	44.6	8.28	0.20	0.34	0.2587	0.0331	0.0617	4.20

Table 5.3: Comparison of the maximum bending strains of the circular structure.

Motion #	Input (g)	AF33 (g)	G_m/G_{max}	V_s (m/s)	$\gamma^{\bigcirc}_{max}$ (milistrain)	$F^{\bigcirc}$	$\epsilon^{\bigcirc}_b$ (milistrain) NCHRP	$\epsilon^{\bigcirc}_b$ (milistrain) Centrifuge, Static	$\epsilon^{\bigcirc}_b$ (milistrain) Centrifuge, Dynamic	$e_b^{\text{NCHRP}}/e_b^{\text{Centrifuge}}$
3	0.015	0.030	0.958	162.2	0.066	129.0	0.0041	0.1471	0.0024	1.72
4	0.014	0.054	0.905	158.9	0.122	123.7	0.0075	0.1489	0.0046	1.64
5	0.015	0.037	0.945	161.1	0.080	127.2	0.0049	0.1510	0.0026	1.89
6	0.166	0.262	0.362	99.8	1.504	48.8	0.0904	0.1542	0.0700	1.29
7	0.198	0.323	0.271	86.3	2.477	36.5	0.1473	0.2167	0.0824	1.79
8	0.081	0.196	0.500	117.2	0.815	67.3	0.0494	0.2356	0.0249	1.99
9	0.470	0.608	0.070	43.7	18.181	9.4	0.9640	0.2415	0.3604	2.67
10	0.494	0.466	0.138	61.6	7.022	18.6	0.4013	0.3311	0.2521	1.59
11	0.423	0.476	0.129	59.6	7.660	17.4	0.4355	0.3363	0.1528	2.85

Table 5.4: Comparison of the maximum hoop strains of the circular structure.

Motion #	Input (g)	AF33 (g)	G_m/G_{max}	V_s (m/s)	$\gamma^{\bigcirc}_{max}$ (milistrain)	$C^{\bigcirc}$	$\epsilon^{\bigcirc}_h$ (milistrain) NCHRP	$\epsilon^{\bigcirc}_h$ (milistrain) Centrifuge, Static	$\epsilon^{\bigcirc}_h$ (milistrain) Centrifuge, Dynamic	$e_h^{\text{NCHRP}}/e_h^{\text{Centrifuge}}$
3	0.015	0.030	0.958	162.2	0.066	0.1119	0.0019	0.0698	0.0020	0.96
4	0.014	0.054	0.905	158.9	0.122	0.1073	0.0034	0.0700	0.0038	0.90
5	0.015	0.037	0.945	161.1	0.080	0.1103	0.0023	0.0699	0.0024	0.96
6	0.166	0.262	0.362	99.8	1.504	0.0423	0.0167	0.0699	0.0298	0.56
7	0.198	0.323	0.271	86.3	2.477	0.0317	0.0207	0.0779	0.0290	0.72
8	0.081	0.196	0.500	117.2	0.815	0.0584	0.0124	0.0792	0.0112	1.11
9	0.470	0.608	0.070	43.7	18.181	0.0081	0.0404	0.0792	0.0782	0.52
10	0.494	0.466	0.138	61.6	7.022	0.0161	0.0303	0.0823	0.0632	0.48
11	0.423	0.476	0.129	59.6	7.660	0.0151	0.0310	0.0942	0.0443	0.70

5.4 Comparison of the in-plane bending strains for the circular culvert

We use the same approach here for the circular culvert as we did for obtaining the bending strain of the rectangular structure. Figure 5.10 displays the static offset and dynamic increment of bending strain data recorded during different base shakings. Again, the bending strain data obtained from the NCHRP 611 method are included in the figures for comparison. As mentioned before, since the scaling factors that are used are not the same, these figures only provide a qualitative means of comparison as well as how the static and dynamic strain profiles vary with different motions. Table 5.3 summarizes the maximum values of the bending strains along with PoIs, and their relationships are illustrated in Figure 5.9. We observe that:

- The static strain offset increases as the model is subjected to more base shakings. This may be partially due to the densification of the soil around of the structure.
- In all cases, the flexibility ratio is greater than 1; and its value decreases as the surrounding soil becomes softer. Therefore, for low-amplitude motions, ovaling should be the dominant mode of deformation of the structure. On the other hand, as $F^{\bigcirc}$ decreases, the relative stiffness of the structure with respect to the surrounding soil increases, which would result in more (dynamic) SSI effects and therefore more complex behavior. The bending strain profiles shown in the figures ascertain this observation.
- In general, the NCHRP method overestimates the bending strains.
- Again, although the range of $\epsilon_b^{\text{NCHRP}}$ and $\epsilon_b^{\text{Centrifuge}}$ differ, they vary similarly with PoIs, especially with $F^{\bigcirc}$ and $\gamma_{max,0}$.

5.5 Comparison of the hoop strains for the circular culvert

We obtained the hoop strain profiles following the same procedure as before, which are shown in Figure 5.12. The summary of the PoIs and maximum hoop strain values are provided in Table 5.4 and Figure 5.11. We observe that:

- The static hoop strain offset is less sensitive than the static bending strain to the application sequence of the base shakings.
- The computed compressibility ratios are less than 1 in all cases. Again, as the soil becomes softer, the relative stiffness of the structure with respect to the surrounding soil increases, and therefore, the compressibility ratio decreases. This can lead to more complex hoop strain profiles under higher amplitude base shakings.

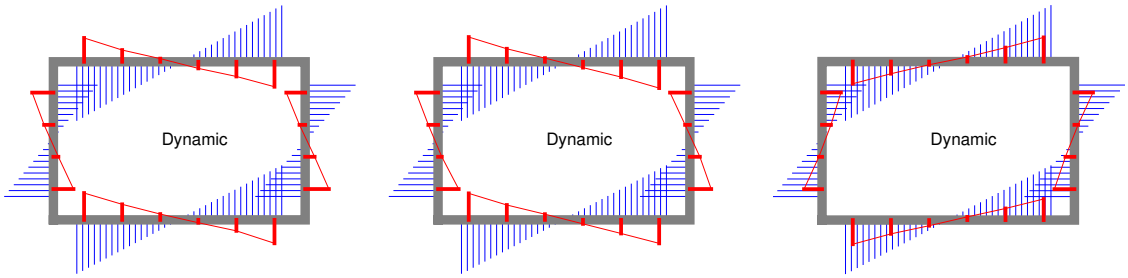

(a) Motion #3 (b) Motion #4 (c) Motion #5

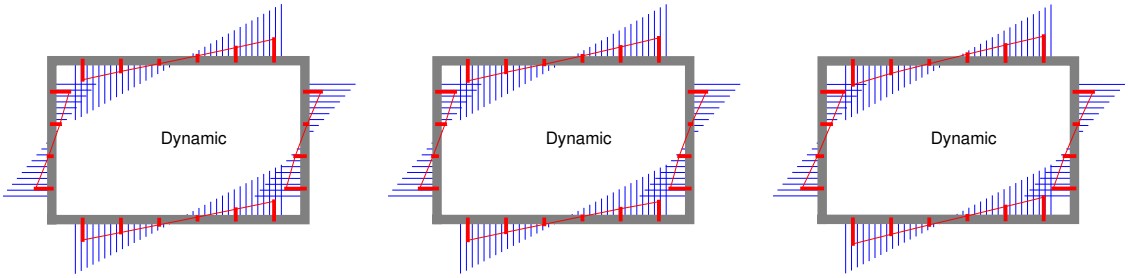

(d) Motion #6 (e) Motion #7 (f) Motion #8

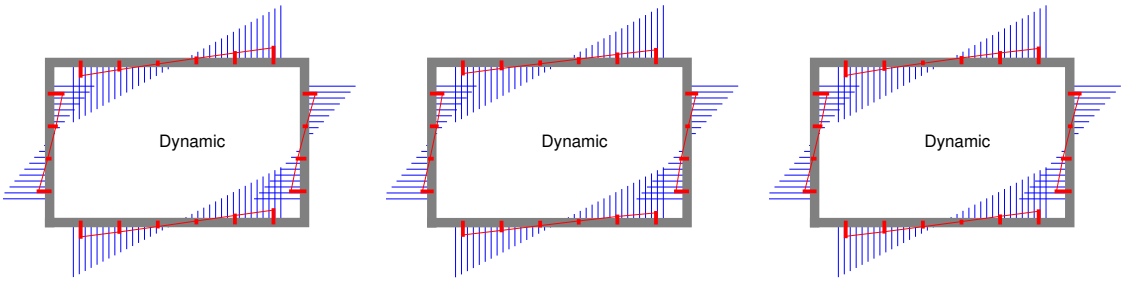

(g) Motion #9 (h) Motion #10 (i) Motion #11

Figure 5.8: Comparison of the experimental in-plane dynamic bending strains in the rectangular culvert with those from the NCHRP 611 method.

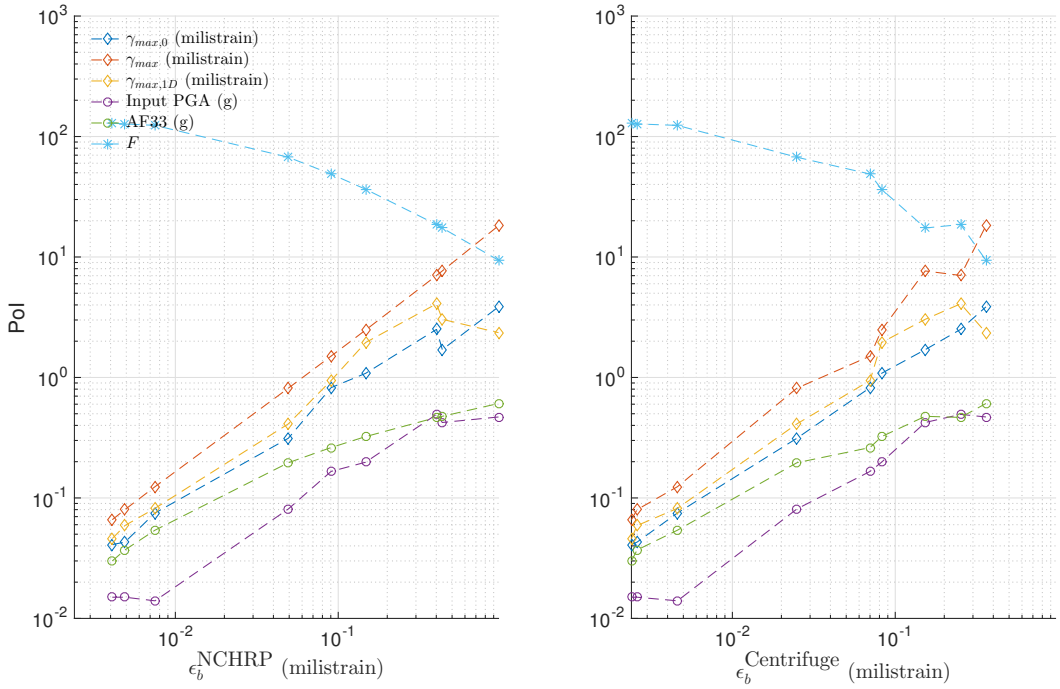

Figure 5.9: PoI correlation with maximum bending strain of the circular structure.

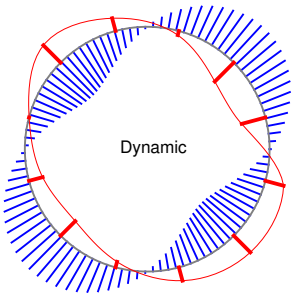

(a) Motion #3

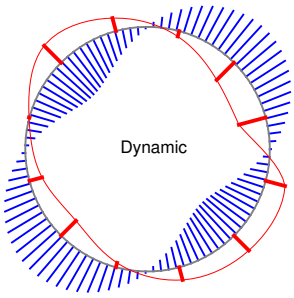

(b) Motion #4

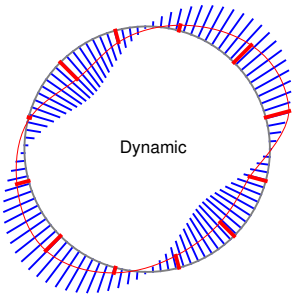

(c) Motion #5

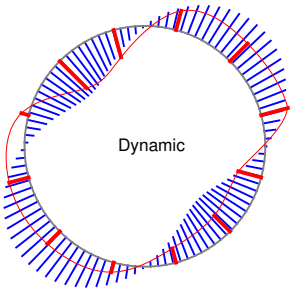

(d) Motion #6

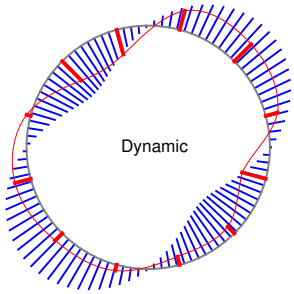

(e) Motion #7

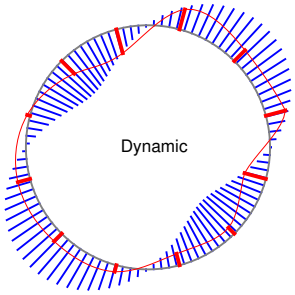

(f) Motion #8

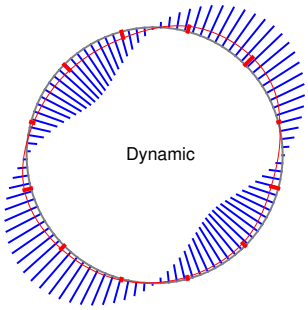

(g) Motion #9

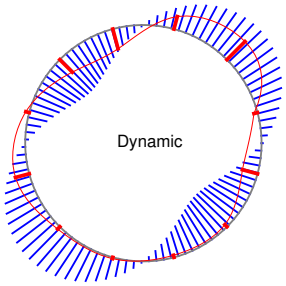

(h) Motion #10

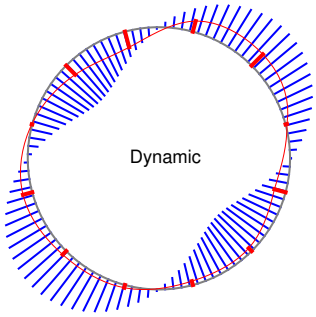

(i) Motion #11

Figure 5.10: Comparison of the experimental in-plane dynamic bending strains in the circular culvert against those from the NCHRP 611 method.

- In general, the NCHRP method underestimates the hoop strains. This is while the NCHRP analysis method suggests the use of the full-slip condition in computing the thrust as a conservative approach to take care of amplifications due to dynamic SSI effects. However, we observe that this conservative solution still underestimates the hoop strains in the circular structure.
- The variations of $\epsilon_h^{\text{NCHRP}}$ and $\epsilon_h^{\text{Centrifuge}}$ with PoIs are similar, especially with respect to C.

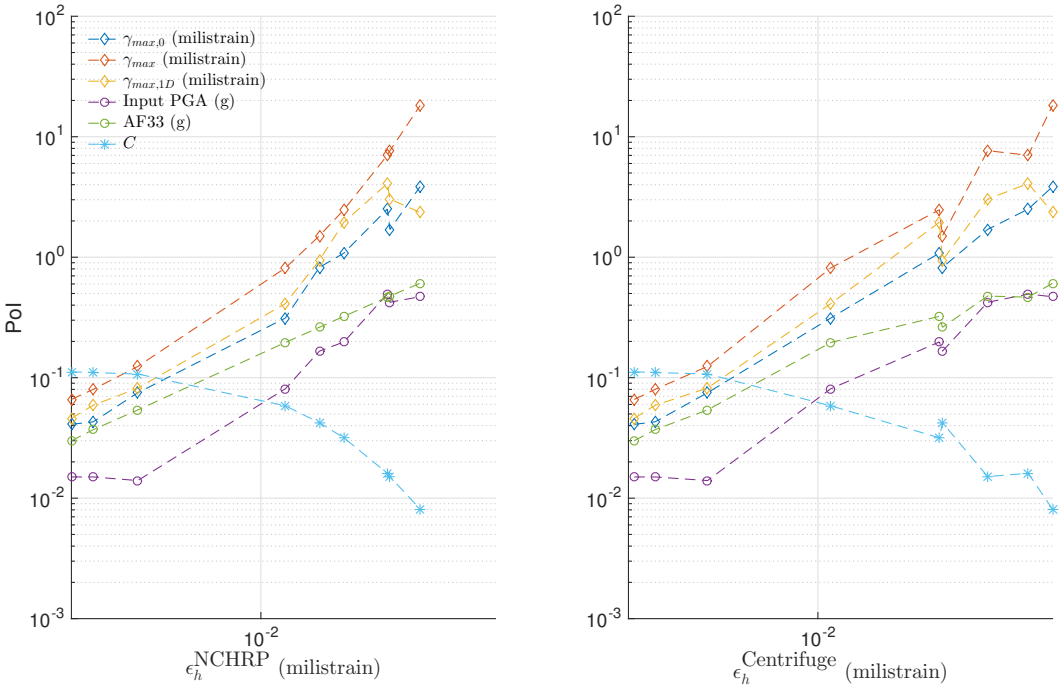

Figure 5.11: PoI correlation with maximum hoop strain of the circular structure.

5.6 The racking of the rectangular structure

As shown, the bending strains computed using the NCHRP 611 method have a direct relationship to the racking displacements imposed on the roof of the structure. In order to see how the computed Δ_s differs from the actual racking of the tested structure, we also computed the experimental racking from the recorded accelerations on the structure. That

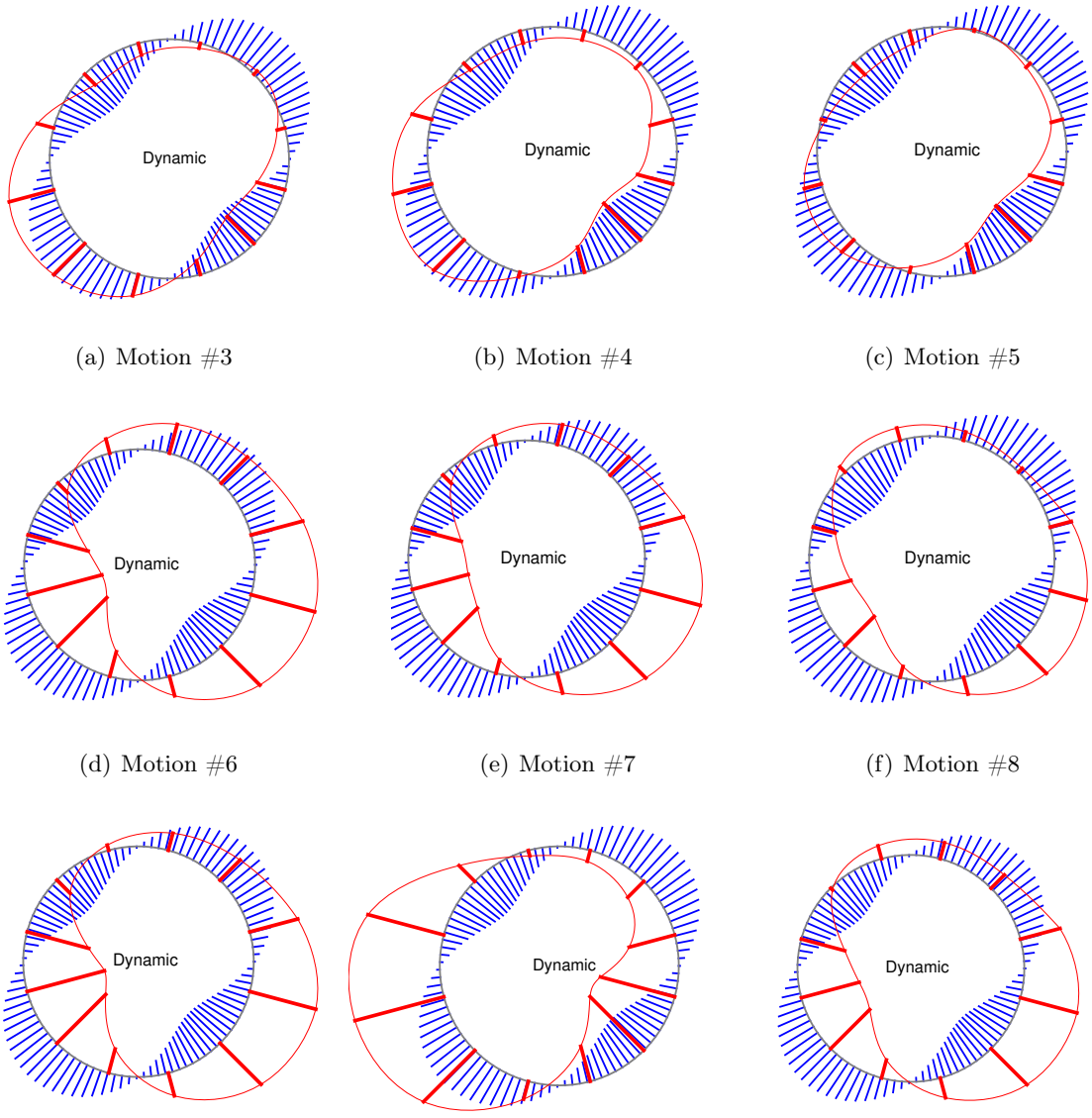

(a) Motion #3 (b) Motion #4 (c) Motion #5

(d) Motion #6 (e) Motion #7 (f) Motion #8

(g) Motion #9 (h) Motion #10 (i) Motion #11

Figure 5.12: Comparison of the experimental dynamic hoop strains in the circular culvert with those from the NCHRP 611 method.

is,

$$\Delta^{\square}_{\text{s,left}} = u_7(t) - u_1(t) \tag{5.12}$$

$$\Delta^{\square}_{\text{s,right}} = u_3(t) - u_6(t) \tag{5.13}$$

where $u_i(t)$ for $i = \{1, 3, 6, 7\}$ are obtained from double integration of the processed acceleration data. Figure 5.13 displays the time series of the resulting racking deformations along the left and right walls of the structure along with the maximum racking deformations that we obtained through the NCHRP 611 method. As shown, the racking displacements along the left and right walls conform to each other and their maximum values are considerably smaller than the NCHRP Δ_s.

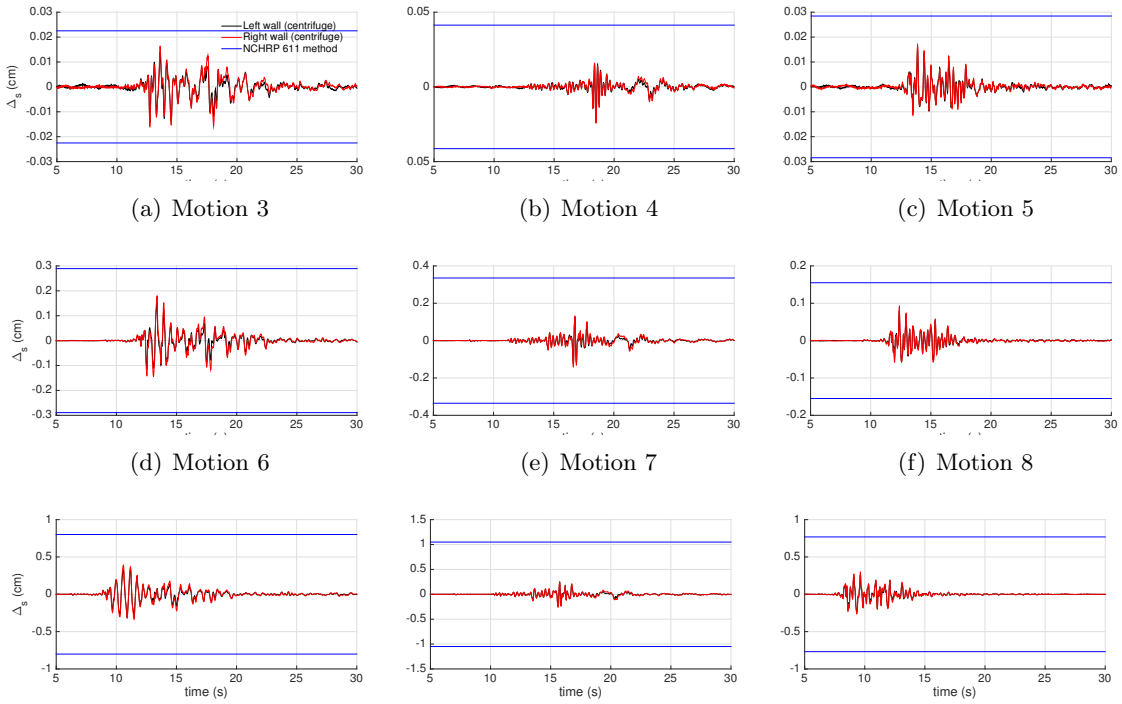

(a) Motion 3 (b) Motion 4 (c) Motion 5

(d) Motion 6 (e) Motion 7 (f) Motion 8

(g) Motion 9 (h) Motion 10 (i) Motion 11

Figure 5.13: Comparison of the rectangular structure racking displacements obtained from recorded accelerations on the structure and from the NCHRP 611 method.

5.7 Comparison of the von Mises stresses

In order to quantify the stress level in culvert cross sections, we also computed the von Mises equivalent stress. This stress invariant is a typical metric used in the strength-based design of metal components, and could also be applied to culverts. Using a scalar invariant such as von Mises stress for comparisons of different methods is desirable in that it combines discrepancies in all of the predicted-vs-measured stress/strain components into single measure.

Assuming a plane strain condition[2]:

$$\sigma_{11} = E\epsilon_{11}, \sigma_{22} = 0, \sigma_{33} = \frac{\nu E}{(1+\nu)(1-2\nu)}\epsilon_{11}, \sigma_{12} = \sigma 13 = \sigma 23 = 0\,, \tag{5.14}$$

and therefore,

$$\sigma_{vm} = \sqrt{\sigma_{11}^2 + \sigma_{33}^2 - \sigma_{11}\sigma_{33}}\,. \tag{5.15}$$

Using the above equation and considering $\nu = 1/3$ and $E = 68.95$ GPa for Aluminum, Table 5.5 provides the resulting von Mises stresses σ_{vm} for each motion.

Table 5.5: Comparison of the Von Mises stress in the culvert structures.

Motion #	$\sigma^{\bigcirc}_{vm}$ (MPa) NCHRP (1)	$\sigma^{\bigcirc}_{vm}$ (MPa) NCHRP-1D (2)	$\sigma^{\bigcirc}_{vm}$ (MPa) Centrifuge (3)	$\sigma^{\square}_{vm}$ (MPa) NCHRP (4)	$\sigma^{\square}_{vm}$ (MPa) NCHRP-1D (5)	$\sigma^{\square}_{vm}$ (MPa) Centrifuge (6)	$\sigma^{\bigcirc}_{vm}$ (1/3) (7)	$\sigma^{\bigcirc}_{vm}$ (2/3) (8)	$\sigma^{\square}_{vm}$ (4/6) (9)	$\sigma^{\square}_{vm}$ (5/6) (10)
3	0.4	0.3	0.2	0.5	0.2	0.2	2.0	1.5	2.5	1.0
4	0.7	0.5	0.4	0.9	0.3	0.4	1.8	1.25	2.3	0.75
5	0.4	0.3	0.2	0.6	0.2	0.2	2.0	1.5	3.0	1.0
6	6.6	4.4	4.7	6.7	2.0	2.2	1.4	0.9	3.0	0.9
7	10.4	8.4	5.5	7.8	3.0	2.8	1.9	1.5	2.8	1.1
8	3.8	2.1	1.7	3.6	1.0	1.4	2.2	1.2	2.6	0.7
9	62.4	10.0	22.8	17.4	5.1	4.2	2.7	0.4	4.1	1.2
10	26.8	16.4	16.0	22.1	5.1	4.7	1.7	1.0	4.7	1.1
11	29.0	12.6	10.0	16.8	4.0	3.8	2.9	1.3	4.4	1.1

5.8 Effects of using $\gamma_{max,1D}$ for computing bending and hoop strains and racking displacements via the NCHRP 611 method

As shown in the previous sections, using the NCHRP 611 method with the iterative procedure to compute γ_{max} resulted in the over-estimation of bending strains in both rectangular

[2]It should be noted that in general σ_{22} is not zero and its effects should be considered in computing the von Mises stress.

and circular culverts. We repeated the NCHRP 611 procedure using $\gamma_{max,1D}$ as the input. As mentioned before, we computed $\gamma_{max,1D}$ for each case by performing nonlinear 1D wave propagation analyses in ABAQUS using soil model parameters obtained form the Bayesian approach. We will use these parameters for our numerical simulations, as it will be discussed in detail in Chapter 6.

Figures 5.14, 5.15 and 5.16 provide the dynamic bending strain profiles for the rectangular culvert, dynamic bending strain profiles for the circular culvert, and the dynamic hoop strain profiles for the circular culvert, respectively. Figure 5.17 displays the comparison of the racking displacements in the rectangular culvert. As seen, using the more-refined procedure to compute maximum free field shear strain resulted in bending strain profiles that are closer to those measured in the centrifuge experiments, and tended to underestimate the profiles in many cases. This trend is even worse for the hoop strains. Table 5.6 summarizes the resulting maximum strain ratios compared to those we obtained using the NCHRP 611 iterative procedure. Moreover, as shown in Figure 5.17, the racking displacements have also become in the same order of those computed from the experimental data. This shows the importance of the choice for γ_{max} if/when we want to use the NCHRP 611 method to compute the seismic demands in culvert structures.

Table 5.6: Maximum bending and hoop strain ratio comparisons when we use the NCHRP 611 iterative procedure and the more-refined 1D site response analysis to compute the free shear strain.

Motion	$e_b^{\square}$, using $\gamma_{\max}$	$e_b^{\square}$, using $\gamma_{\max,1D}$	$e_b^{\bigcirc}$, using $\gamma_{\max}$	$e_b^{\bigcirc}$, using $\gamma_{\max,1D}$	$e_h^{\bigcirc}$, using $\gamma_{\max}$	$e_h^{\bigcirc}$, using $\gamma_{\max,1D}$
3	2.17	0.65	1.72	1.19	0.96	0.71
4	2.21	0.65	1.64	1.09	0.90	0.61
5	2.42	0.72	1.89	1.38	0.96	0.71
6	2.86	0.84	1.29	0.82	0.56	0.45
7	2.68	1.04	1.79	1.42	0.72	0.65
8	2.46	0.68	1.99	1.01	1.11	0.75
9	3.94	1.15	2.67	0.39	0.52	0.26
10	4.50	1.03	1.59	0.95	0.48	0.40
11	4.20	0.99	2.85	1.18	0.70	0.51

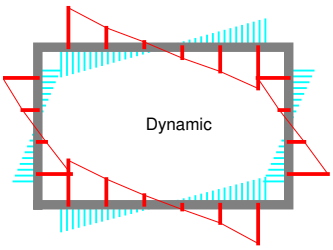

(a) Motion #3

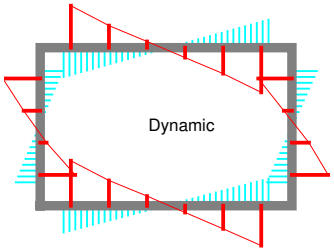

(b) Motion #4

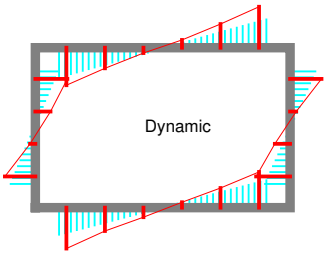

(c) Motion #5

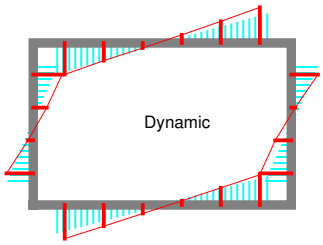

(d) Motion #6

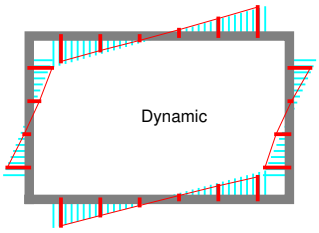

(e) Motion #7

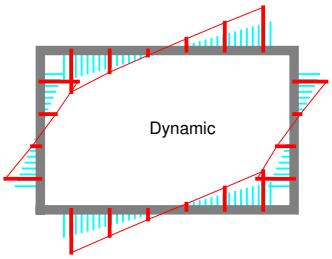

(f) Motion #8

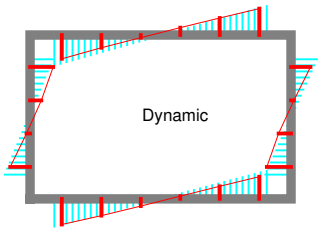

(g) Motion #9

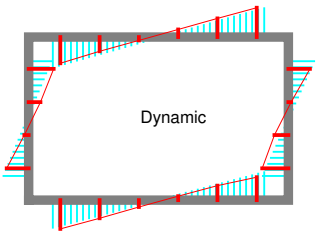

(h) Motion #10

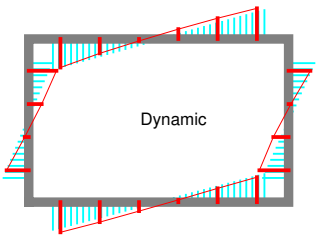

(i) Motion #11

Figure 5.14: Comparison of the experimental in-plane dynamic bending strains in the rectangular culvert against those from the NCHRP 611 method when $\gamma_{max,1D}$ is used as the input maximum free field shear strain.

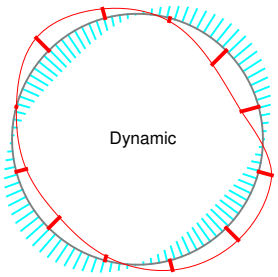

(a) Motion #3

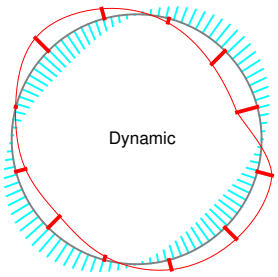

(b) Motion #4

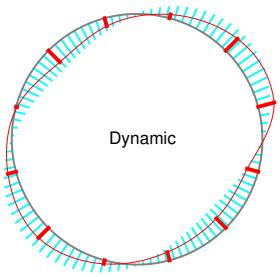

(c) Motion #5

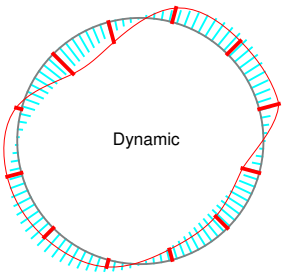

(d) Motion #6

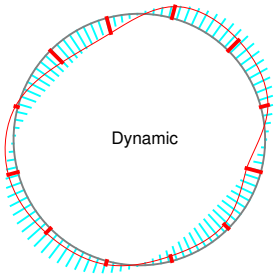

(e) Motion #7

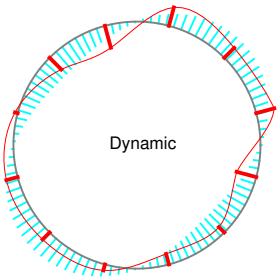

(f) Motion #8

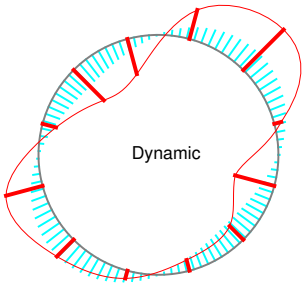

(g) Motion #9

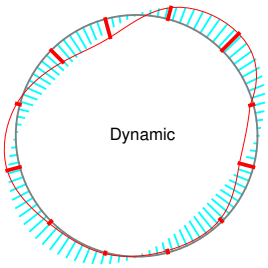

(h) Motion #10

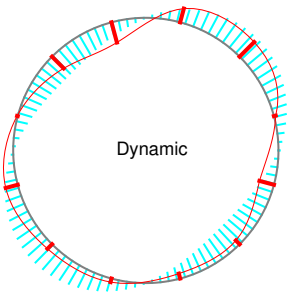

(i) Motion #11

Figure 5.15: Comparison of the experimental in-plane dynamic bending strains in the circular culvert against those from the NCHRP 611 method when $\gamma_{max,1D}$ is used as the input maximum free field shear strain.

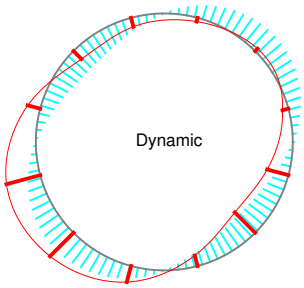

(a) Motion #3

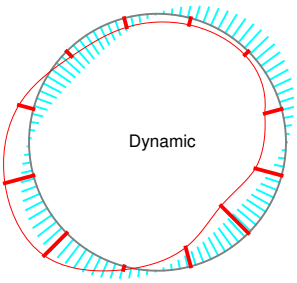

(b) Motion #4

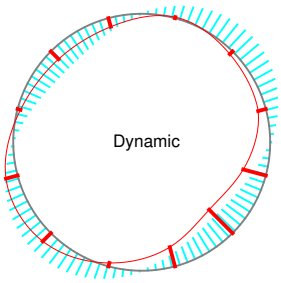

(c) Motion #5

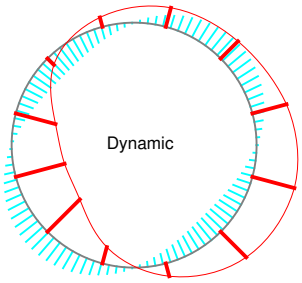

(d) Motion #6

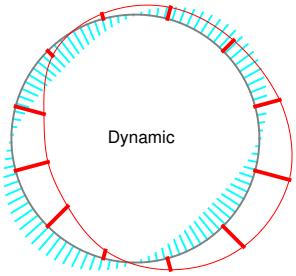

(e) Motion #7

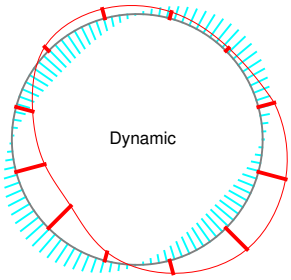

(f) Motion #8

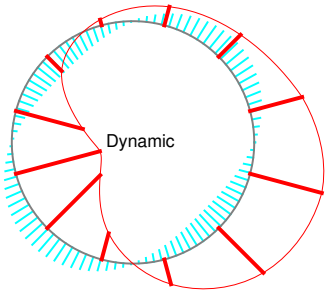

(g) Motion #9

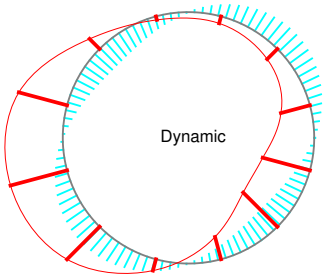

(h) Motion #10

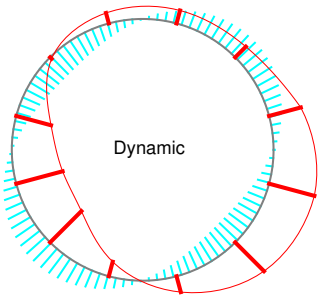

(i) Motion #11

Figure 5.16: Comparison of the experimental dynamic hoop strains in the circular culvert against those from the NCHRP 611 method when $\gamma_{max,1D}$ is used as the input maximum free field shear strain.

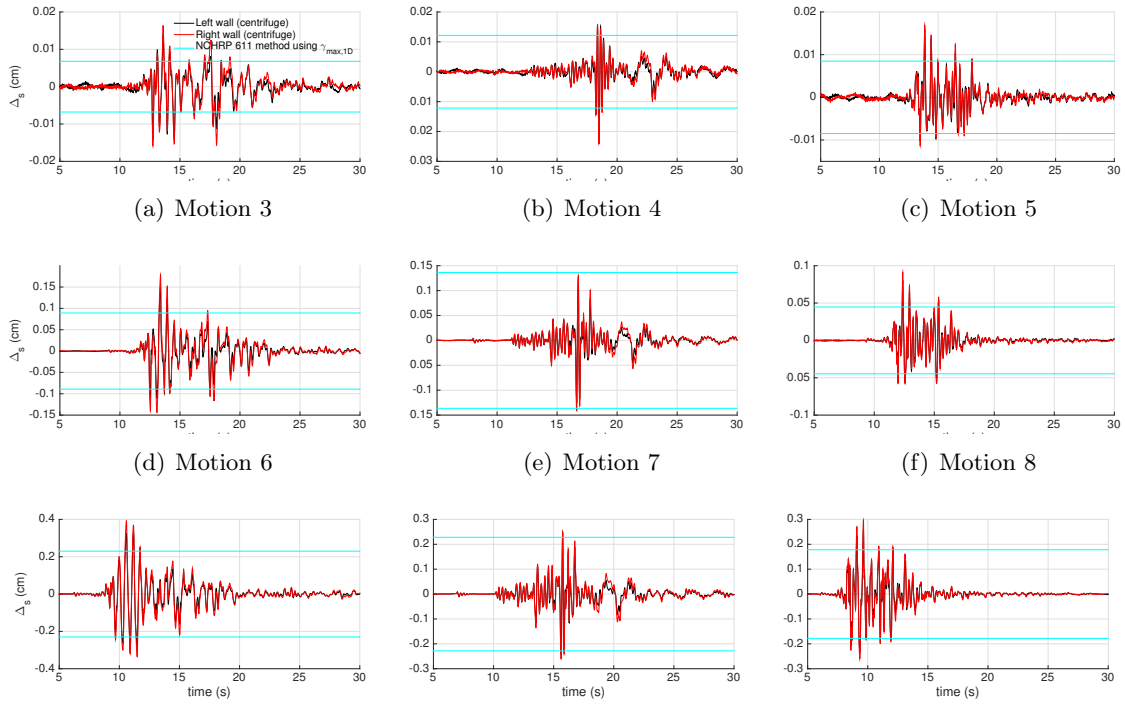

(a) Motion 3 (b) Motion 4 (c) Motion 5

(d) Motion 6 (e) Motion 7 (f) Motion 8

(g) Motion 9 (h) Motion 10 (i) Motion 11

Figure 5.17: Comparison of the rectangular structure racking displacement obtained from recorded accelerations on the structure and from the NCHRP 611 method using $\gamma_{max,1D}$ as the input.

Chapter 6

Finite element modeling & analysis of the centrifuge tests

In this chapter, we provide details of direct numerical modeling of the conducted centrifuge experiments and investigate the predictive capabilities of the calibrated finite element model to capture the key response parameters.

6.1 Development of the numerical model

In order to numerically study the dynamic SSI behavior of the centrifuge specimens, a two-dimensional (2D) finite element model was constructed in prototype scale based on the dimensions given in Figure 2.10. In experiments with earthquake excitations (i.e., motions 3 to 11), the scaling factor N ranges from $20.7g$ to $21.1g$. As such, we decided to use the same factor of $N = 21g$ for all numerical simulations in this report. As shown in Figure 6.1, the input motion is applied along the bottom boundary of the model, where the vertical degrees of freedom are fixed. We did not model the container explicitly. Instead, we imposed periodic boundary conditions along horizontal degrees of freedom at the left and right vertical edges of the soil domain while their vertical degrees of freedom are fixed, since a flexible shear beam container is used for the experiments. It should be noted that this configuration is used in the dynamic loading steps of analyses. In order to set up the initial stress conditions appropriately, we also performed a static analyses under gravity loading prior to each dynamic analysis. During the static analyses, we fixed the horizontal degrees of freedom at the left and right vertical edges of the discretized model, while leaving the vertical degrees of freedom free.

We used bilinear plane-strain elements for modeling the soil and the rectangular structure

and beam elements for modeling the circular structure. We also used frictional contact elements to model sliding at the soil-structure interface. Following Deng et al. (2016) and by considering the soil friction angle of $\phi_{\text{soil}} = 35$ degrees, the friction coefficient of the interface elements is computed as,

$$\tan\left(\phi_{\text{interface}}\right) = 0.7 \tan\left(\phi_{\text{soil}}\right) \approx 0.33\,. \tag{6.1}$$

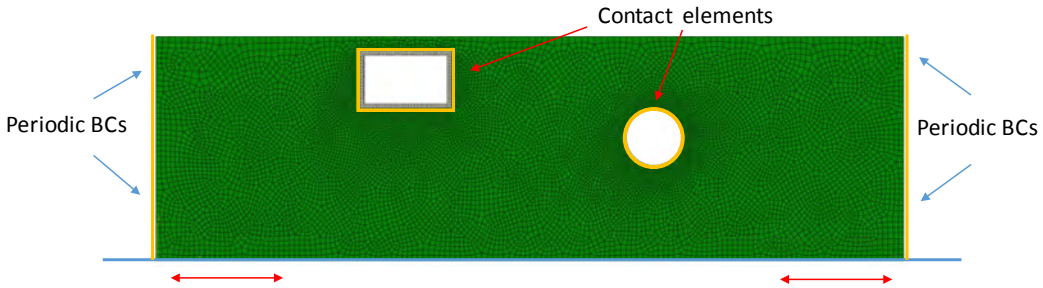

Figure 6.1: Mesh configuration of the finite element model used in numerical analysis.

As the structures were expected to behave linear elastically in all of the experiments, we used linear elastic material models for both culverts using the properties of Aluminum T60-61, which are $\gamma = 26.5$ kN/m^3, $E = 68.9$ GPa and $\nu = 0.33$. On other hand, for capturing the nonlinear soil behavior, which is a relatively dense dry Ottawa sand, we used a multi-axial cyclic plasticity model. Details of this model are provided next.

6.2 Multiaxial cyclic plasticity soil model: formulation, implementation and validation

It is well known that soil nonlinearity comes into effect even at very small strain levels (Dafalias and Popov, 1977). Therefore, it is generally necessary to model soil nonlinearity in any dynamic SSI analysis. One of the soil models that is widely used to capture the behavior of cohesionless soil deposits in numerical simulations is the pressure-dependent multi-yield-surface model by Yang et al. (2003). However, this model has too many parameters, which are required to capture the typical soils' large strain and post-liquefaction behavior, and this makes its calibration a formidable task. Since our experiments were in relatively dense dry sand, we decided to use a simpler soil model derived in total stress space, which features a small number of parameters. This model was the bounding surface multi-axial cyclic plasticity soil model by Borja and Amies (1994); Borja et al. (2000), which has a vanishing elastic region and viscous terms, which enable taking small-strain damping into account at the material point level.

6.2.1 Formulation

The total stress tensor $\boldsymbol{\sigma}$ of Borja's model consists of two major—namely, the inviscid ($\boldsymbol{\sigma}^{\mathbf{inv}}$) and the viscous ($\boldsymbol{\sigma}^{\mathbf{vis}}$)—parts, as given by

$$\boldsymbol{\sigma} = \boldsymbol{\sigma}^{\mathbf{inv}} + \boldsymbol{\sigma}^{\mathbf{vis}} \tag{6.2}$$

where

$$\begin{aligned} \boldsymbol{\sigma}^{\mathbf{inv}} &= \boldsymbol{C}^{\mathbf{e}} : (\boldsymbol{\epsilon} - \boldsymbol{\epsilon}^{\mathbf{p}}), \\ \boldsymbol{\sigma}^{\mathbf{vis}} &= \boldsymbol{D} : \dot{\boldsymbol{\epsilon}}, \end{aligned} \tag{6.3}$$

and $\boldsymbol{C}^{\mathbf{e}}$ and $\boldsymbol{D}$ are elastic stiffness and viscous damping tensors, respectively; $\boldsymbol{\epsilon}$ is the total strain tensor; $\boldsymbol{\epsilon}^{\mathbf{p}}$ is the plastic strain tensor, and $\dot{\boldsymbol{\epsilon}}$ is the total strain rate. In this study, a linear stiffness-proportional damping is adopted (Borja et al., 2000), which can be devised by defining $\boldsymbol{D}$ as

$$\boldsymbol{D} = \frac{2\xi_0}{\omega_0}\boldsymbol{C}^{\mathbf{e}} = a_1 \boldsymbol{C}^{\mathbf{e}} \tag{6.4}$$

where ω_0 is the frequency at which the small strain damping ratio is equal to ξ_0. The inviscid part of Borja's model is based on J2-bounding surface plasticity theory with a vanishing elastic region. The translation of the bounding surface with radius R is facilitated by the exponential hardening modulus

$$H' = h\kappa^m + H_0 \tag{6.5}$$

where h and m are the exponential hardening parameters and for $H_0 > 0$ the bounding surface also hardens kinematically (for further formulations details, see Borja and Amies, 1994; Borja et al., 2000).

To achieve an optimal rate of convergence for the Newton's method required in implicit dynamic time-stepping methods, the consistent tangent moduli are required (Simo and Hughes, 2000). Borja and Wu (1994) derived this fourth-order tensor as,

$$\boldsymbol{C}^{\mathbf{inv}}_{\mathbf{ep}} = \frac{d\boldsymbol{\sigma}^{\mathbf{inv}}_{n+1}}{d\boldsymbol{\epsilon}_{n+1}} = K\mathbf{1}\otimes\mathbf{1} + \psi\mathbf{I}_{\mathbf{dev}} + \frac{\partial\psi}{\partial\boldsymbol{\epsilon}_{n+1}} \otimes \Delta\boldsymbol{\epsilon}' \tag{6.6}$$

where $\mathbf{I}_{\mathbf{dev}} = \mathbf{I} - \frac{1}{3}\mathbf{1}\otimes\mathbf{1}$, is the deviatoric identity tensor and K is the bulk modulus. The parameter ψ is defined through the equation $\Delta\boldsymbol{\sigma}' = \psi\,\Delta\boldsymbol{\epsilon}'$, where $\Delta\boldsymbol{\sigma}'$ and $\Delta\boldsymbol{\epsilon}'$ denote the deviatoric stress and strain increments, respectively. The third term on the right-hand side of Eq. (6.6) renders $\boldsymbol{C}^{\mathbf{inv}}_{\mathrm{ep}}$ to be non-symmetric in general. However, as demonstrated by Borja and Wu (1994), the symmetric part of this consistent tangent stiffness tensor is often adequate to produce accurate solutions at superlinear convergence rates. Incidentally, a symmetric tangent also facilitates significant savings in computer memory requirements as

well as in flops for solving the system-level equilibirum equations. Furthermore, one can relate the viscous stress increment to the total strain increment as follows:

$$\boldsymbol{\sigma}^{\mathbf{vis}}_{n+1} = \boldsymbol{C}^{\mathbf{vis}}_{\mathbf{ep}} : \mathrm{d}\boldsymbol{\epsilon}_{n+1} = \frac{2\xi_0}{\omega_0}\boldsymbol{C}^{\mathbf{e}} : \dot{\boldsymbol{\epsilon}}_{n+1} = \frac{1}{\mathrm{dt}}\frac{2\xi_0}{\omega_0}\boldsymbol{C}^{\mathbf{e}} : \mathrm{d}\boldsymbol{\epsilon}_{n+1} \tag{6.7}$$

which yields,

$$\boldsymbol{C}^{\mathbf{vis}}_{\mathbf{ep}} = \frac{1}{\mathrm{d}t}\frac{2\xi_0}{\omega_0}\boldsymbol{C}^{\mathbf{e}}\,. \tag{6.8}$$

By only retaining the symmetric part of the consistent tangent of Borja's model, we obtain the total consistent tangent stiffness moduli as,

$$\boldsymbol{C}_{\mathbf{ep}} = \boldsymbol{C}^{\mathbf{inv}}_{\mathbf{ep,symm}} + \boldsymbol{C}^{\mathbf{vis}}_{\mathbf{ep}} = K\mathbf{1}\otimes\mathbf{1} + \psi\mathbf{I}_{\mathbf{dev}} + \frac{1}{\mathrm{d}t}\frac{2\xi_0}{\omega_0}\boldsymbol{C}^{\mathbf{e}} \tag{6.9}$$

where $\mathrm{d}t$ is the time increment chosen for the time discretization of $\dot{\boldsymbol{\epsilon}}_{n+1}$.

6.2.2 Implementation and validation

We implemented all variants of the model—namely, plastic, plastic with viscous damping, with symmetric or non-symmetric tangent, plane-strain, axisymmetric, and three-dimensional—in the commonly used commercial finite element analysis software ABAQUS (Hibbit et al., 2007), through its user-defined material (UMAT) subroutine interface.

For verification, we made comparisons of 1D wave propagation analysis results with those obtained using DEEPSOIL (Hashash et al., 2016), which is a well-known computer code for site response analysis that features linear, equivalent linear, and validated nonlinear soil models. Here, we opted to use its nonlinear module, which is based on a pressure-dependent hyperbolic model by Matasovic (1993). Reasonable—and otherwise unremarkable—soil and model parameters were chosen for these verification simulations: the height of the soil column was 28.9 m, $G_{\max} = 8$ MPa, $h = G_{\max}$, $m = 0.5$, $R = 50$ kPa, $\omega_0 = 4\pi$ rad/s, $\xi_0 = 1\%$, and $H_0 = 0$. Fig. 6.2 displays the acceleration time-series and the 5%-damped spectral accelerations obtained at the surface of the soil column, which was subjected to a Ricker wavelet with a central frequency that is equal to the natural frequency of the homogeneous soil layer considered. Fig. 6.3 displays the results obtained for the same soil column when it was subjected to an earthquake motion. As shown, for both cases, the results of the implemented soil model are in very good agreement with those obtained using DEEPSOIL, especially after adding the viscous damping term.

For studying the multi-axial capability of this soil model, we used a series of centrifuge experiments on buried reservoirs in dry Nevada sand and observed its superior performance against the nominally more complex pressure-dependent multi-yield surface soil model. Details of those comparisons are omitted for brevity and can be found in (Zhang et al., 2017).

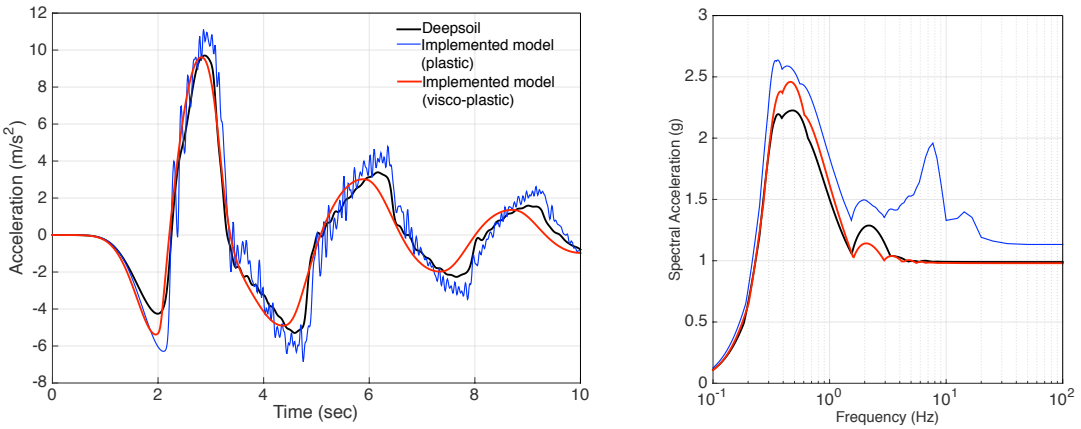

(a) Acceleration history (b) Spectral acceleration

Figure 6.2: 1D site response analysis: (a) acceleration history and (b) 5%-damped spectral acceleration subjected to the Ricker wavelet input.

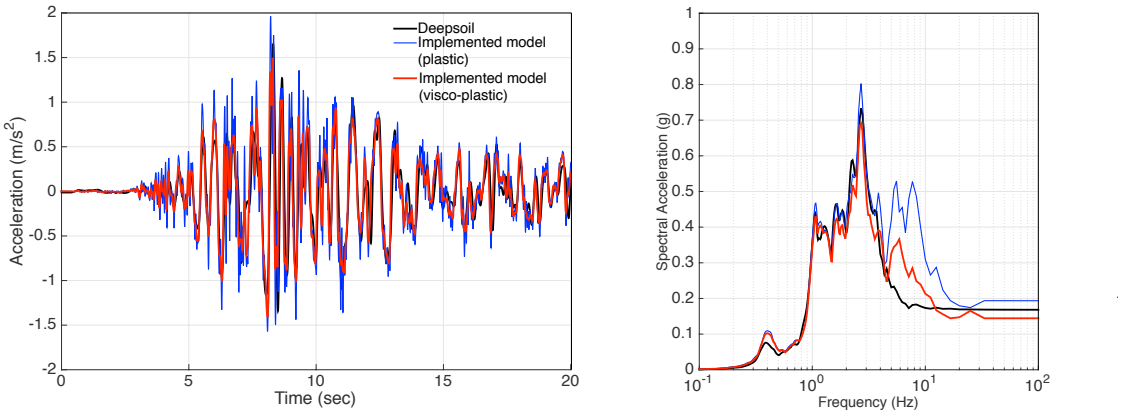

(a) Acceleration history (b) Spectral acceleration

Figure 6.3: 1D site response analysis: (a) acceleration history and (b) 5%-damped spectral acceleration subjected to earthquake input.

6.3 Calibration of the soil parameters from centrifuge data

Borja's model can be defined by small strain shear wave velocity profile, modulus reduction curves, small strain damping, and shear strength of the soil deposit at hand. It can be shown that under the simple shear test condition, the following relationship exists between the normalized shear modulus $G/G_{\max}$ and shear strain γ using Borja's model (Chao and Borja, 1998).

$$\frac{G}{G_{\max}} + \frac{3}{2\gamma}\int_0^{2G_i\gamma}\left[h\left(\frac{R/\sqrt{2}+G\gamma-\tau}{\tau}\right)^m + H_0\right]^{-1} \mathrm{d}\tau - 1 = 0. \tag{6.10}$$

Therefore, for the given $G/G_{\max}$ curve, one can obtain the unknown parameters h, m, R and H_0 by solving a series of nonlinear equations or via the least squares method (Zhang et al., 2017). As mentioned earlier in Chapter 5, we used a Bayesian approach to infer the shear wave velocity, $G/G_{\max}$ and the small strain viscous damping coefficient a_1 from free field acceleration measurements. Assuming a power function for the shear wave velocity profile and the hardening parameter h resulted in

$$V_s \text{ (m/s)} = 16.905 + 192.976\left(\frac{z}{H}\right)^{0.331} \tag{6.11}$$

and

$$h = \left[0.107 + 0.474\left(\frac{z}{H}\right)^{4.581}\right] G_{\max} \tag{6.12}$$

along with other parameters estimated as

$$m = 1.579,\ R = 0.0028\ G_{\max},\ a_1 = 0.0031\,. \tag{6.13}$$

We also assumed that $H_0 = 0$. Figure 6.4 displays the resulting calibrated shear wave velocity profile and the $G/G_{\max}$ curves for different depths, which are used in various numerical analyses of this report.

6.4 Numerical analyses

We used the calibrated soil model in finite element models of the centrifuge tests and performed numerical simulations using the earthquake excitations as input motions. To examine the predictive capabilities of the finite element models, we present the measured and numerically computed accelerations at various locations within the soil and on the specimen structures, the bending strains along the rectangular structure, and the bending and hoop strains along the circular structure in the following subsections.

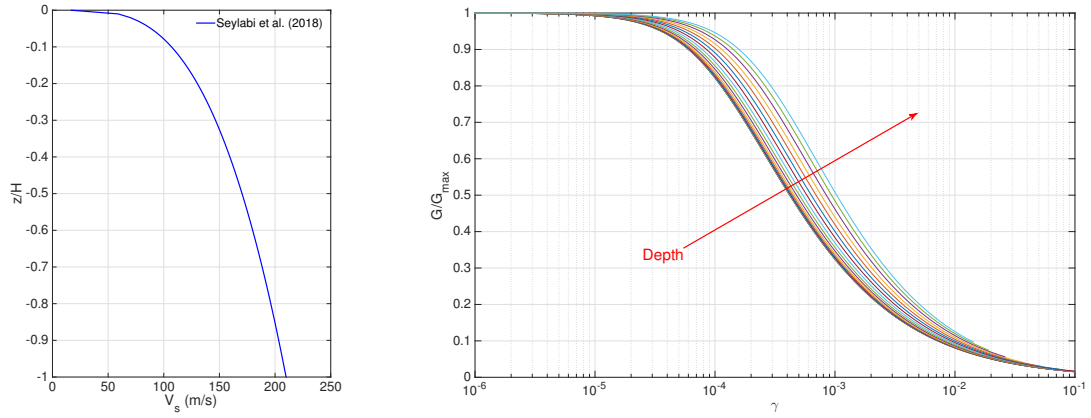

(a) Shear wave velocity profile

(b) $G/G_{\max}$ curves for different depth

Figure 6.4: Calibrated shear wave velocity profile and $G/G_{\max}$ curves over the depth.

6.4.1 Comparison of horizontal accelerations in soil

Figures 6.5-6.13 display comparisons of horizontal acceleration time-series and Fourier amplitudes for the left/southern acceleration array (i.e., locations AA1, AC12, AD18, AE25 and AF28). Figures 6.14-6.22 display similar data for the middle array (i.e., locations AAH5, AC16, ADH23, AE26 and AFH30). For the reader's convenience, we recall here that the motions 3-5 were low-amplitude, 6-8 were moderate amplitude, and 9-11 were high amplitude excitations (see Figure 2.19). As shown, the finite element models generally capture the time-series and the Fourier amplitude spectra of the measured accelerations for all motion amplitudes. It should be noted that we used only the left array acceleration data from motions #3 and #9 for calibrating the soil constitutive model parameters. Moreover, as shown, ICP AAH5 was only functional during motions 3, 4, and 5.

6.4.2 Comparison of horizontal accelerations of culvert specimens

Figures 6.23-6.31 display the comparisons for the time series and Fourier amplitude spectra of horizontal accelerations for the rectangular (locations 7 and 1) and circular (locations 16 and 14) culverts. Again, the agreement between the numerical and experimental results for all motions are generally very good.

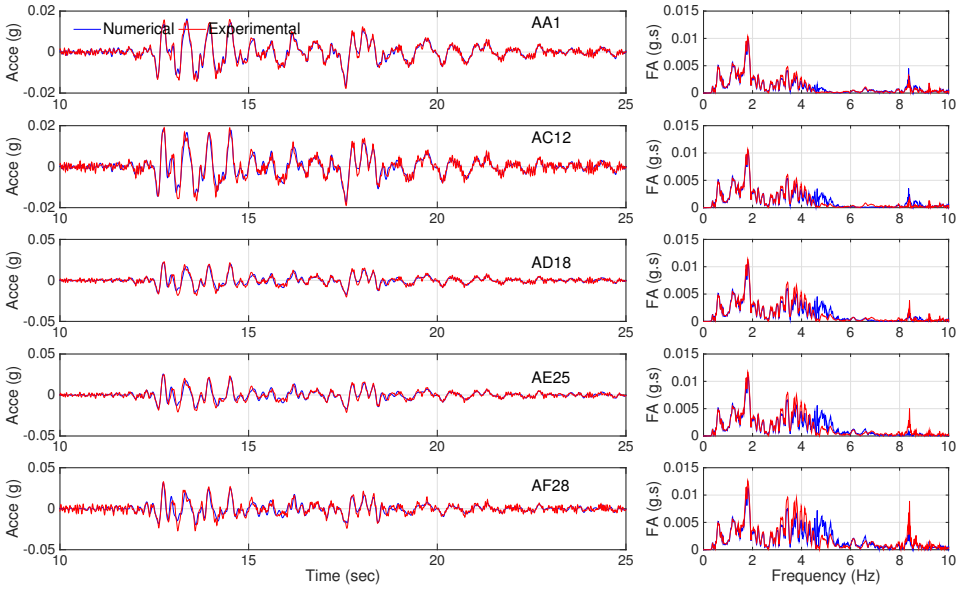

Figure 6.5: Time series and Fourier amplitude spectra of the accelerations recorded at the left array (AA1, AC12, AD18, AE25 and AF28) for motion #3.

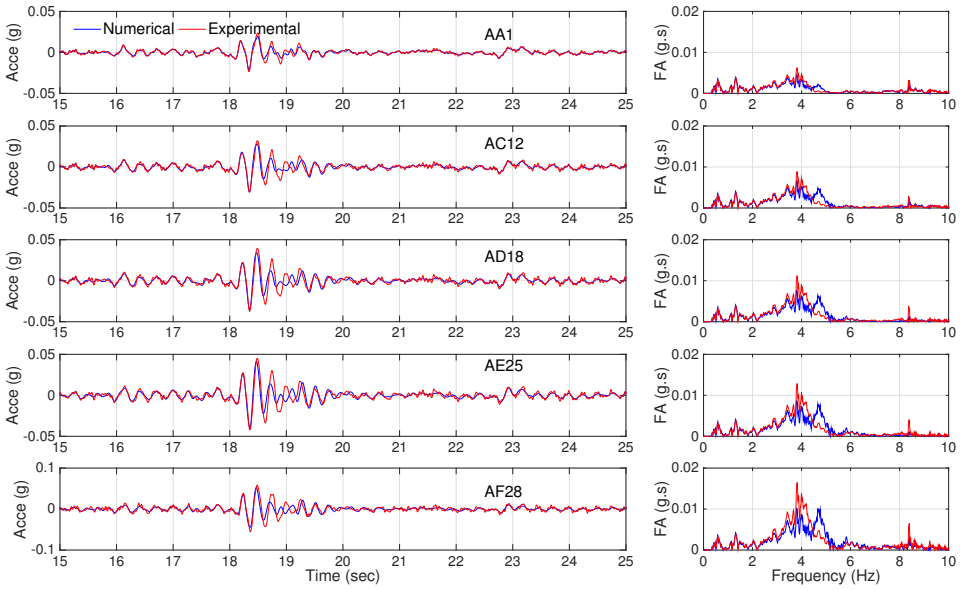

Figure 6.6: Time series and Fourier amplitude spectra of the accelerations recorded at the left array (AA1, AC12, AD18, AE25 and AF28) for motion #4.

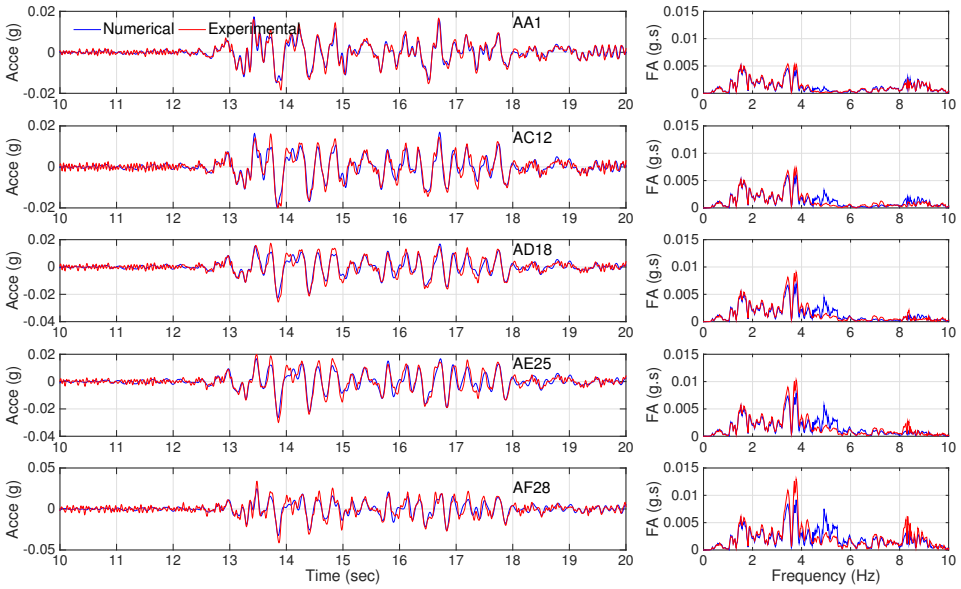

Figure 6.7: Time series and Fourier amplitude spectra of the accelerations recorded at the left array (AA1, AC12, AD18, AE25 and AF28) for motion #5.

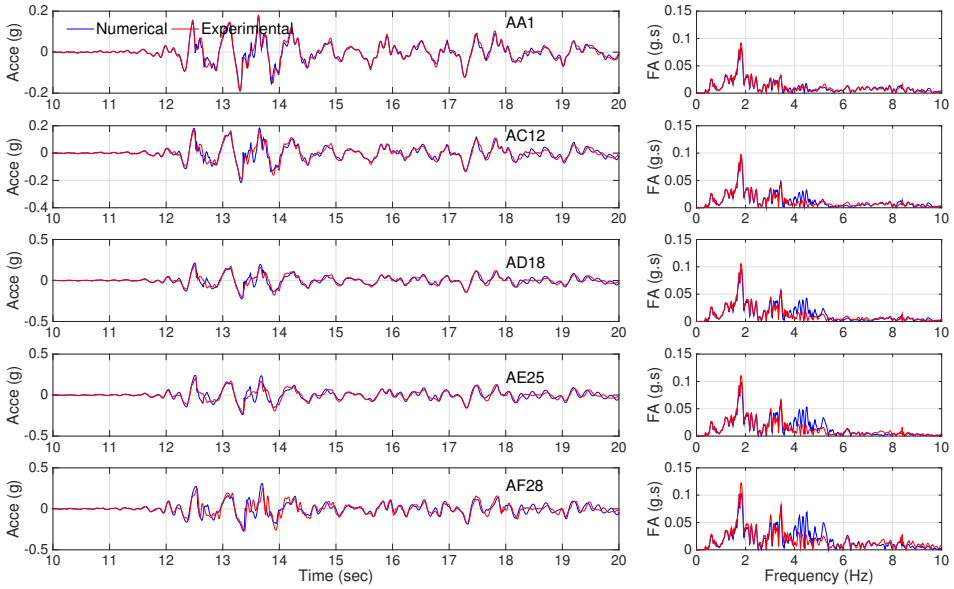

Figure 6.8: Time series and Fourier amplitude spectra of the accelerations recorded at the left array (AA1, AC12, AD18, AE25 and AF28) for motion #6.

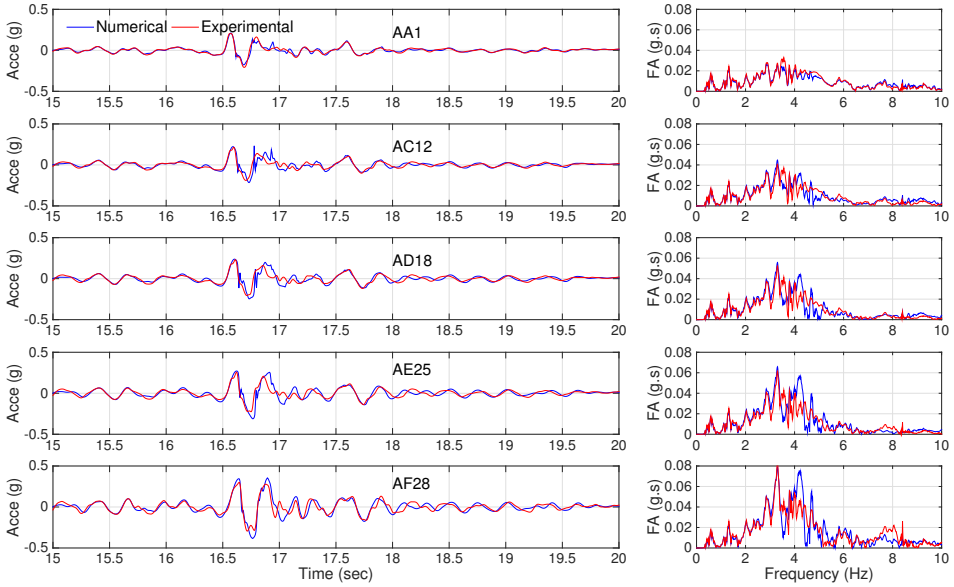

Figure 6.9: Time series and Fourier amplitude spectra of the accelerations recorded at the left array (AA1, AC12, AD18, AE25 and AF28) for motion #7.

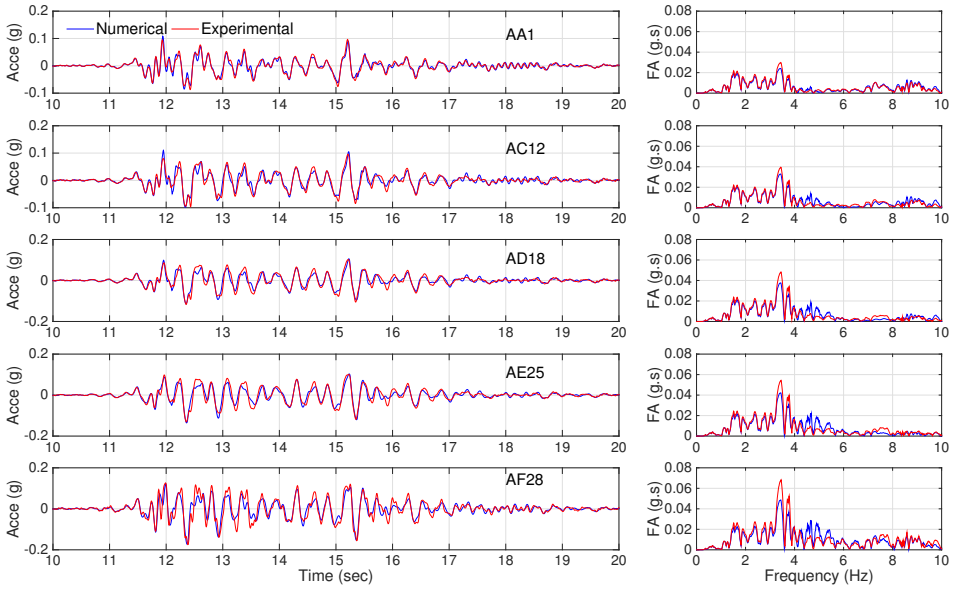

Figure 6.10: Time series and Fourier amplitude spectra of the accelerations recorded at the left array (AA1, AC12, AD18, AE25 and AF28) for motion #8.

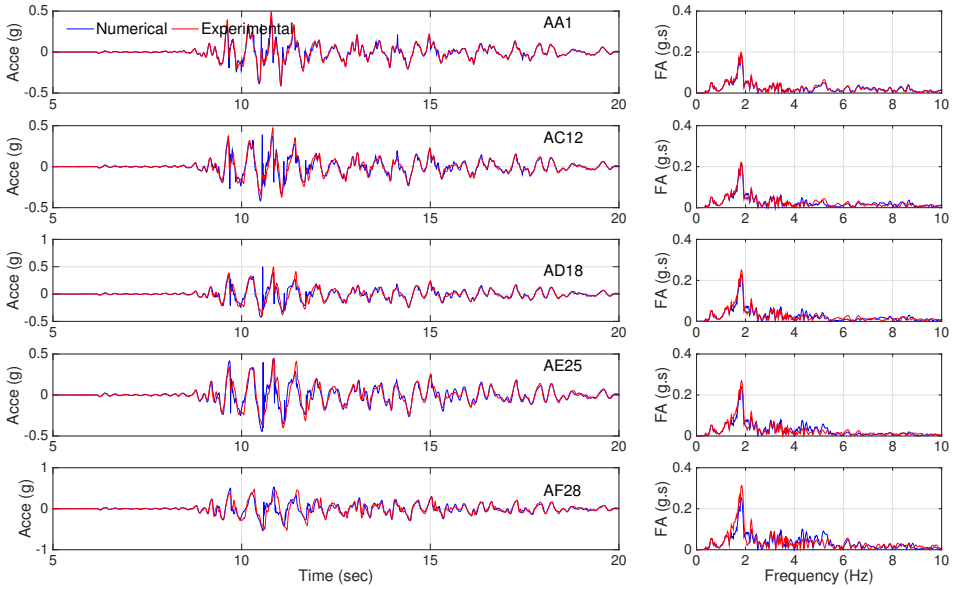

Figure 6.11: Time series and Fourier amplitude spectra of the accelerations recorded at the left array (AA1, AC12, AD18, AE25 and AF28) for motion #9.

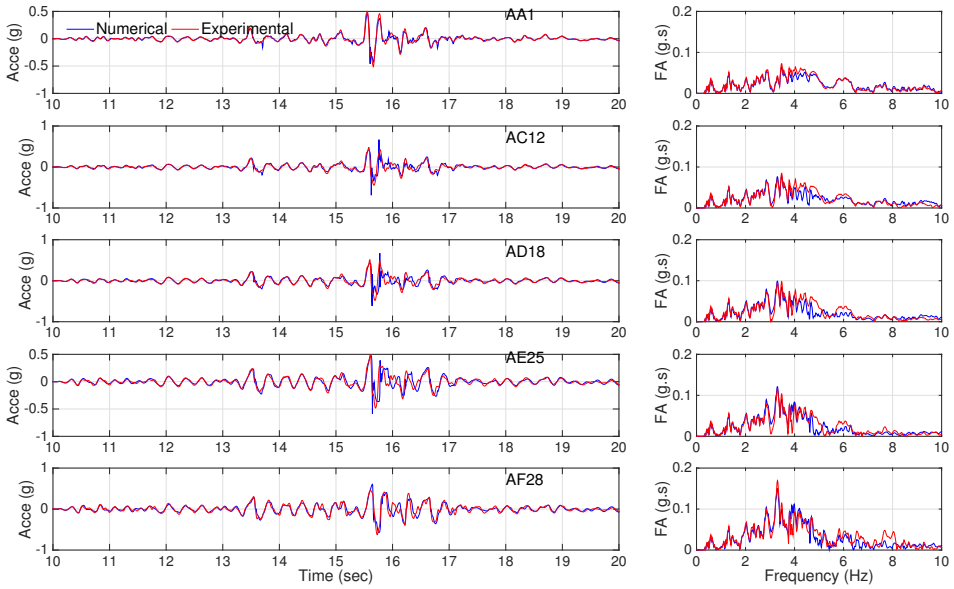

Figure 6.12: Time series and Fourier amplitude spectra of the accelerations recorded at the left array (AA1, AC12, AD18, AE25 and AF28) for motion #10.

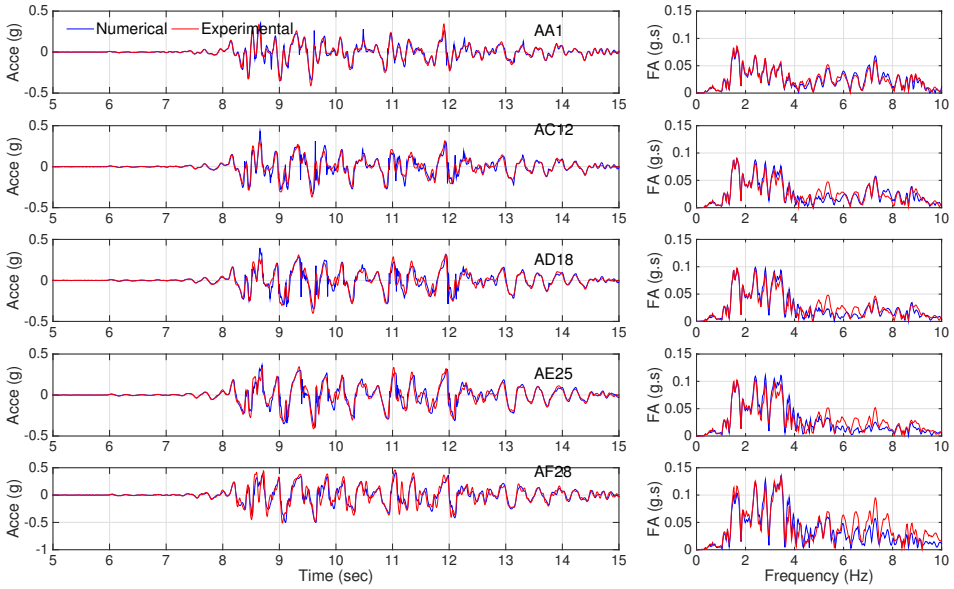

Figure 6.13: Time series and Fourier amplitude spectra of the accelerations recorded at the left array (AA1, AC12, AD18, AE25 and AF28) for motion #11.

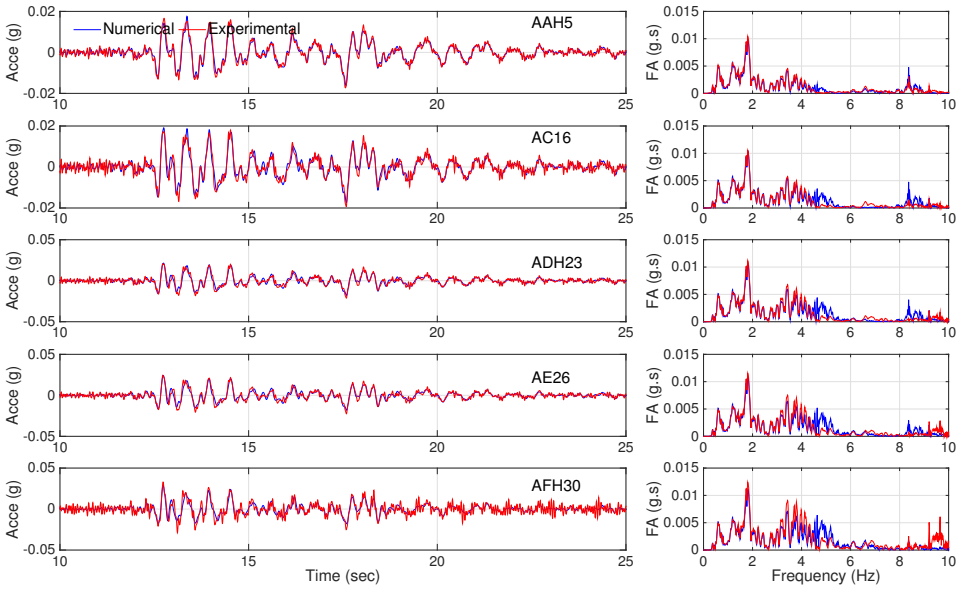

Figure 6.14: Time series and Fourier amplitude spectra of the accelerations recorded at the middle array (AAH5, AC16, ADH23, AE26 and AFH30) for motion #3.

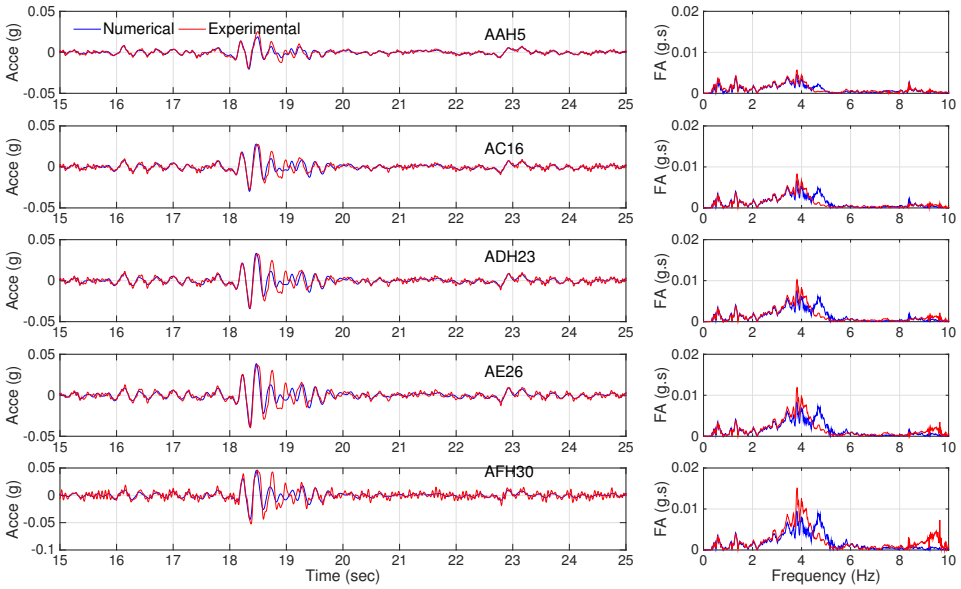

Figure 6.15: Time series and Fourier amplitude spectra of the accelerations recorded at the middle array (AAH5, AC16, ADH23, AE26 and AFH30) for motion #4.

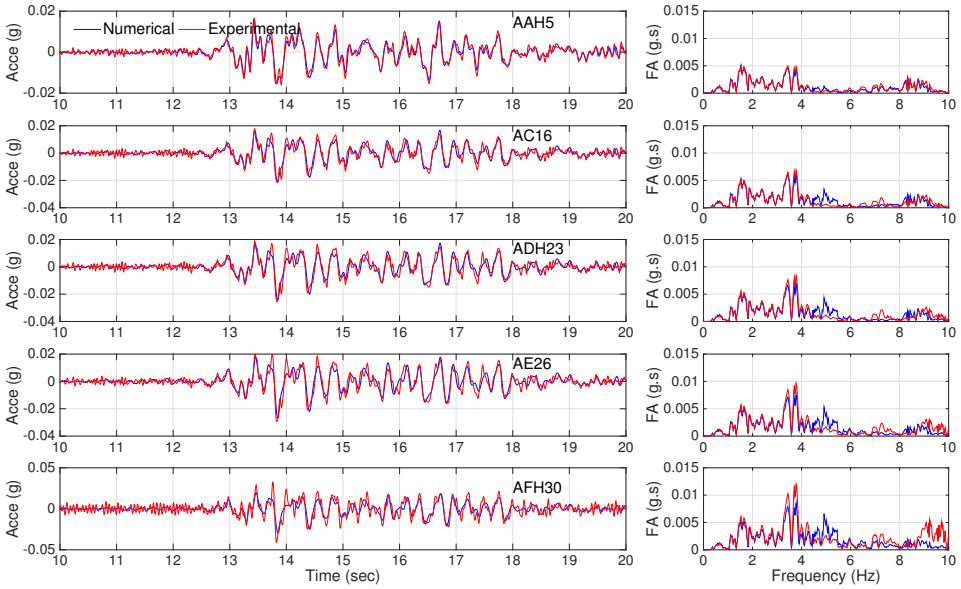

Figure 6.16: Time series and Fourier amplitude spectra of the accelerations recorded at the middle array (AAH5, AC16, ADH23, AE26 and AFH30) for motion #5.

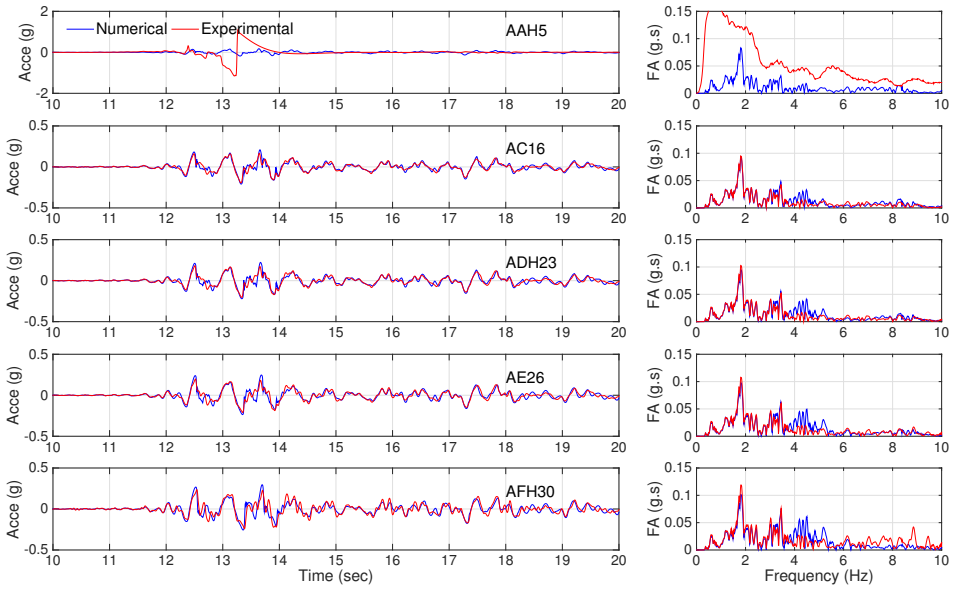

Figure 6.17: Time series and Fourier amplitude spectra of the accelerations recorded at the middle array (AAH5, AC16, ADH23, AE26 and AFH30) for motion #6.

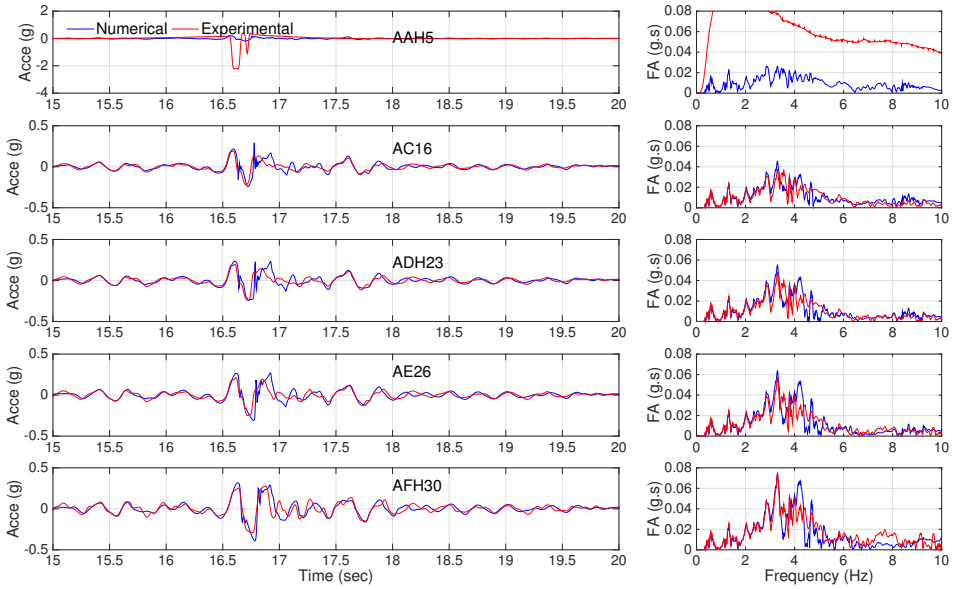

Figure 6.18: Time series and Fourier amplitude spectra of the accelerations recorded at the middle array (AAH5, AC16, ADH23, AE26 and AFH30) for motion #7.

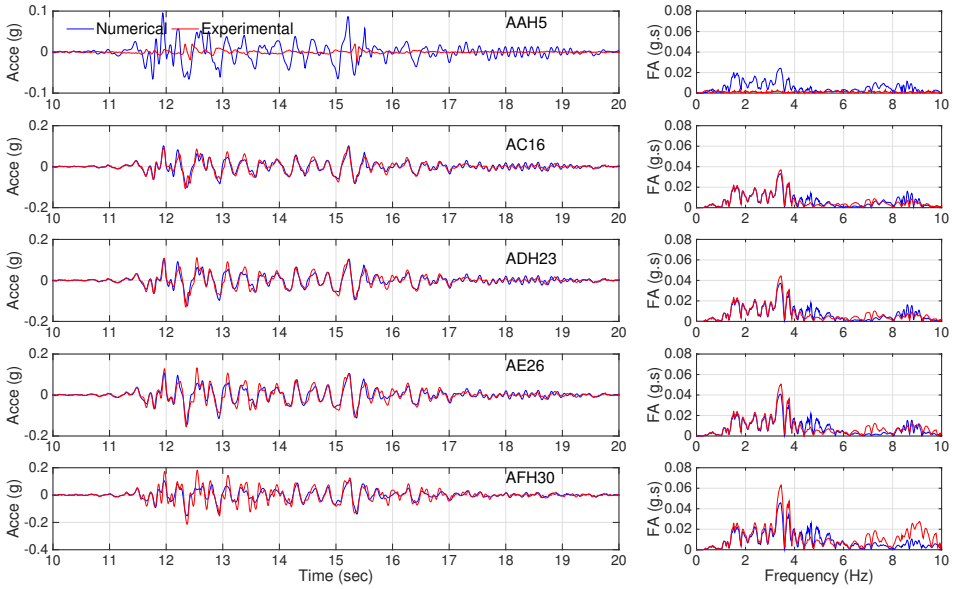

Figure 6.19: Time series and Fourier amplitude spectra of the accelerations recorded at the middle array (AAH5, AC16, ADH23, AE26 and AFH30) for motion #8.

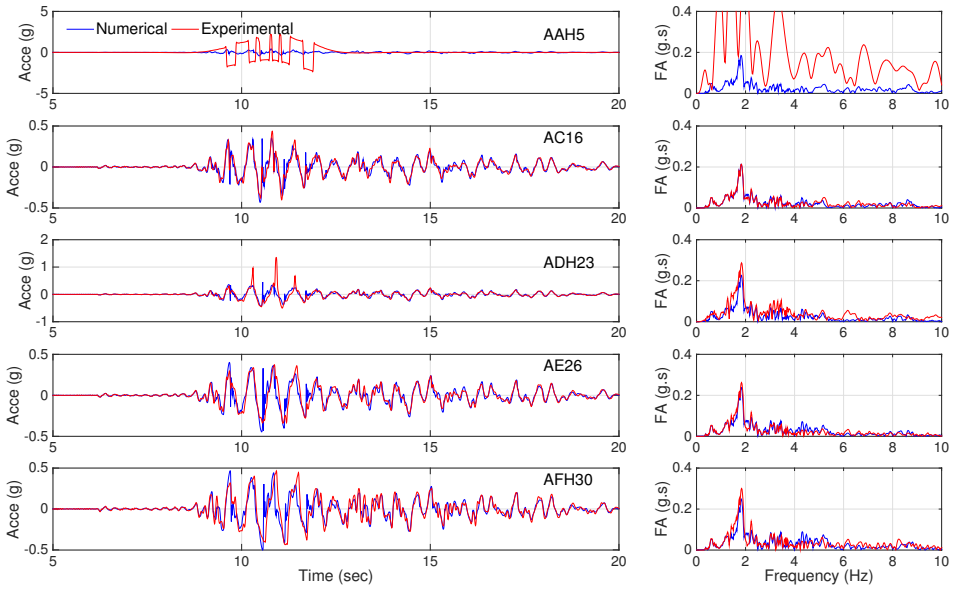

Figure 6.20: Time series and Fourier amplitude spectra of the accelerations recorded at the middle array (AAH5, AC16, ADH23, AE26 and AFH30) for motion #9.

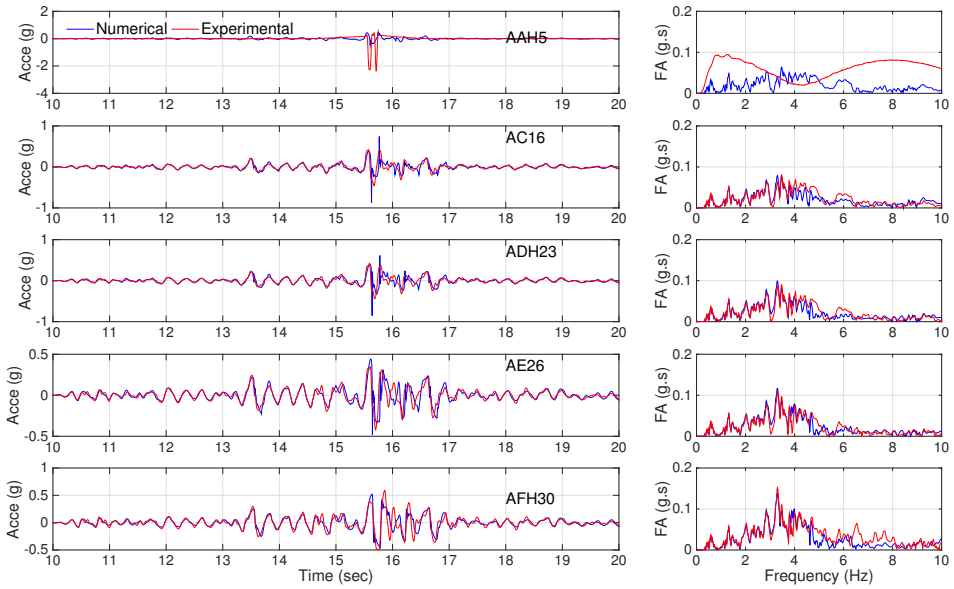

Figure 6.21: Time series and Fourier amplitude spectra of the accelerations recorded at the middle array (AAH5, AC16, ADH23, AE26 and AFH30) for motion #10.

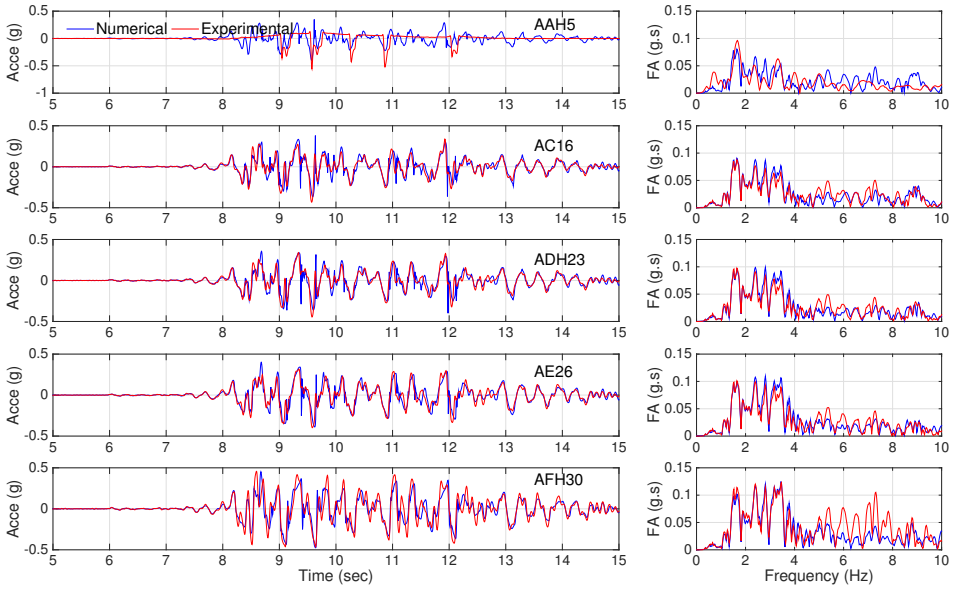

Figure 6.22: Time series and Fourier amplitude spectra of the accelerations recorded at the middle array (AAH5, AC16, ADH23, AE26 and AFH30) for motion #11.

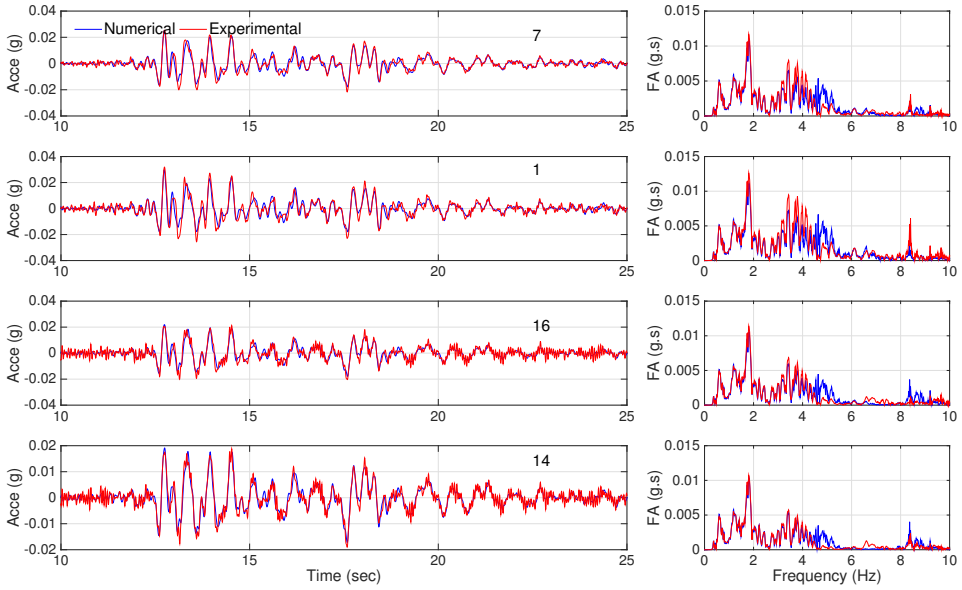

Figure 6.23: Time series and Fourier amplitude spectra of the horizontal accelerations recorded on the specimen structures (7, 1, 16 and 14) for motion #03.

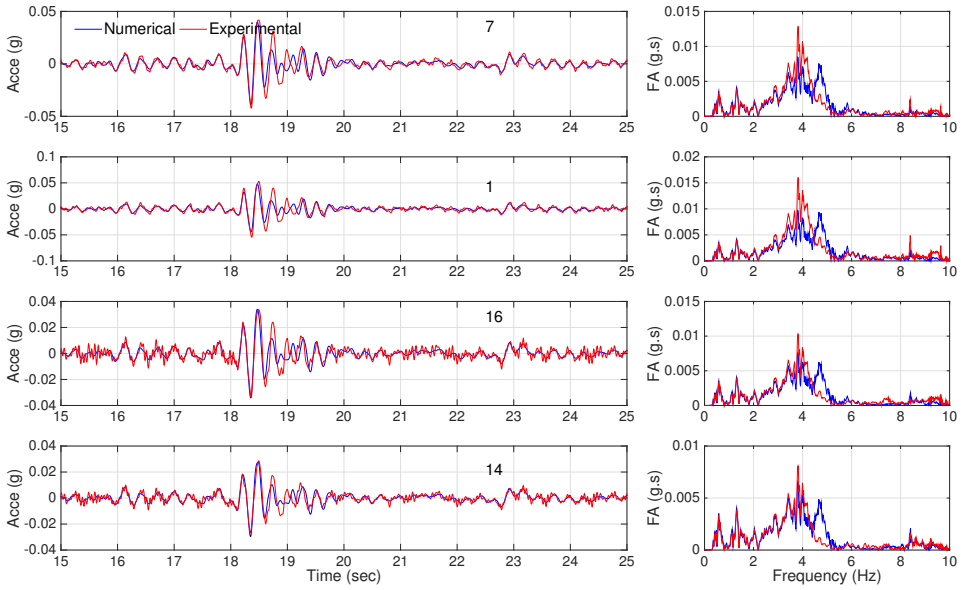

Figure 6.24: Time series and Fourier amplitude spectra of the horizontal accelerations recorded on the specimen structures (7, 1, 16 and 14) for motion #04.

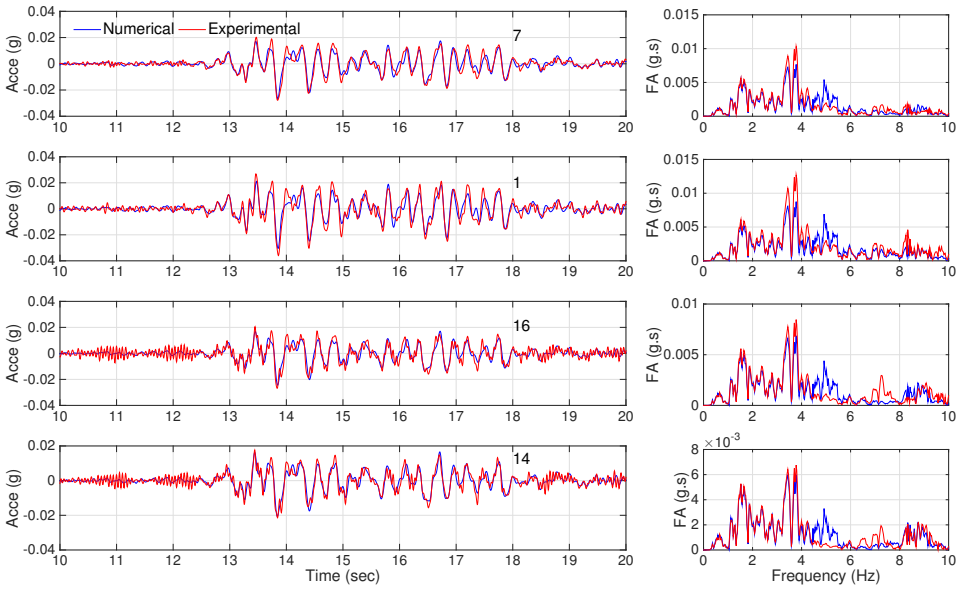

Figure 6.25: Time series and Fourier amplitude spectra of the horizontal accelerations recorded on the specimen structures (7, 1, 16 and 14) for motion #05.

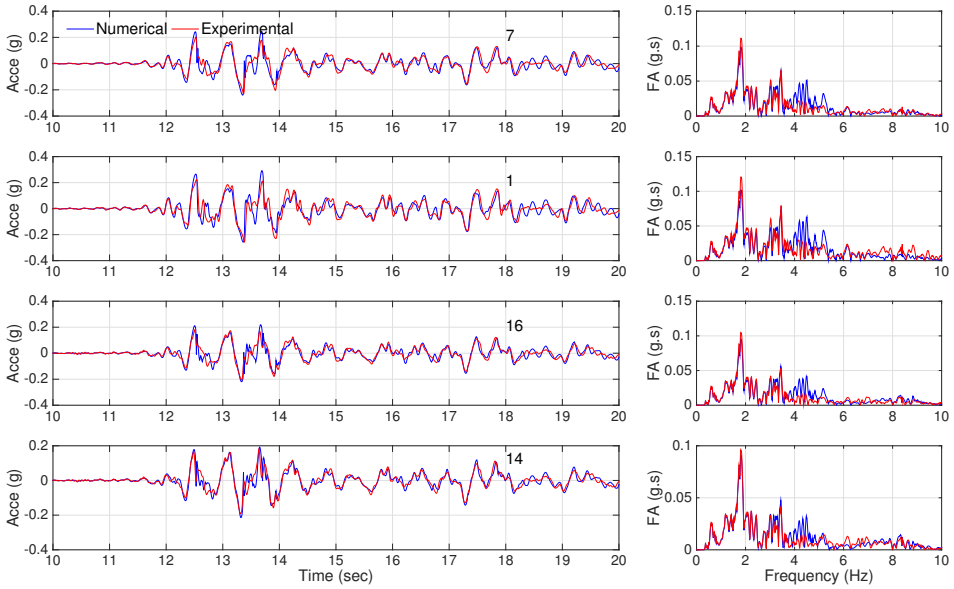

Figure 6.26: Time series and Fourier amplitude spectra of the horizontal accelerations recorded on the specimen structures (7, 1, 16 and 14) for motion #06.

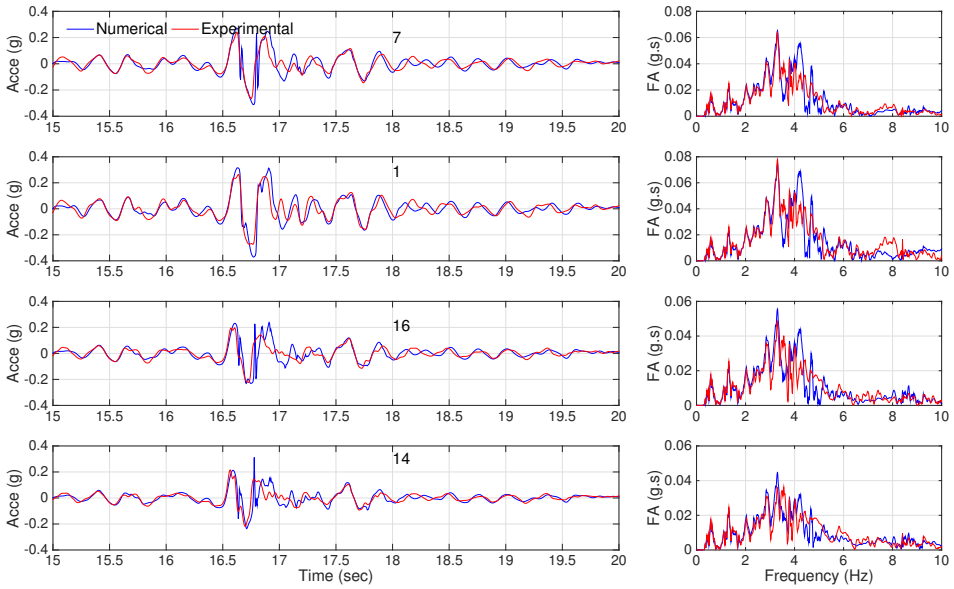

Figure 6.27: Time series and Fourier amplitude spectra of the horizontal accelerations recorded on the specimen structures (7, 1, 16 and 14) for motion #07.

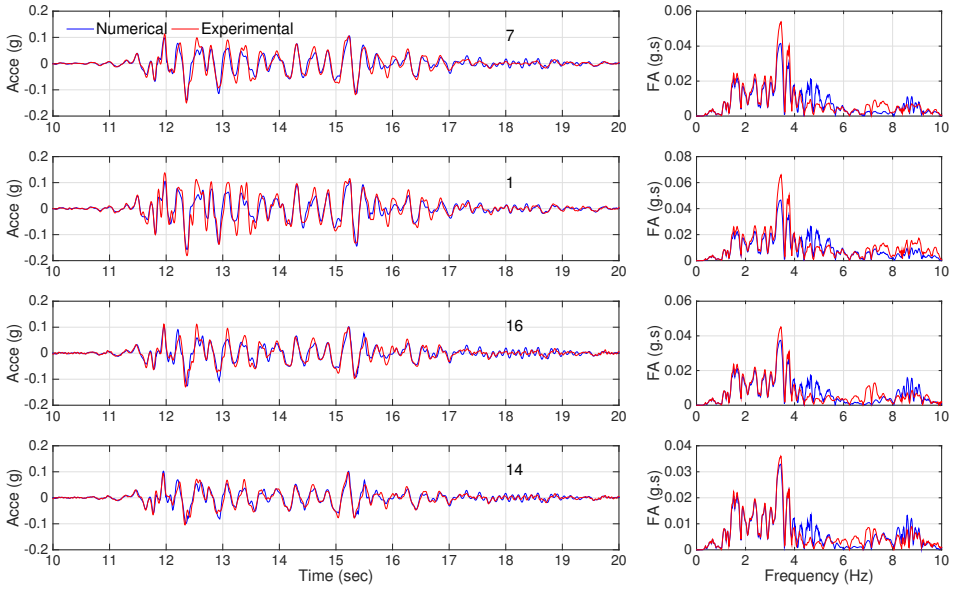

Figure 6.28: Time series and Fourier amplitude spectra of the horizontal accelerations recorded on the specimen structures (7, 1, 16 and 14) for motion #08.

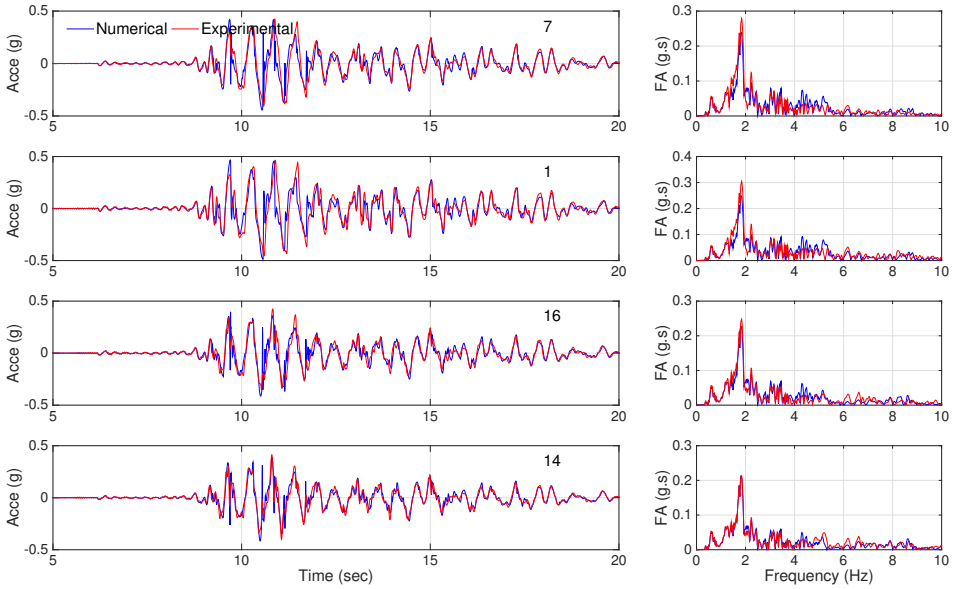

Figure 6.29: Time series and Fourier amplitude spectra of the horizontal accelerations recorded on the specimen structures (7, 1, 16 and 14) for motion #09.

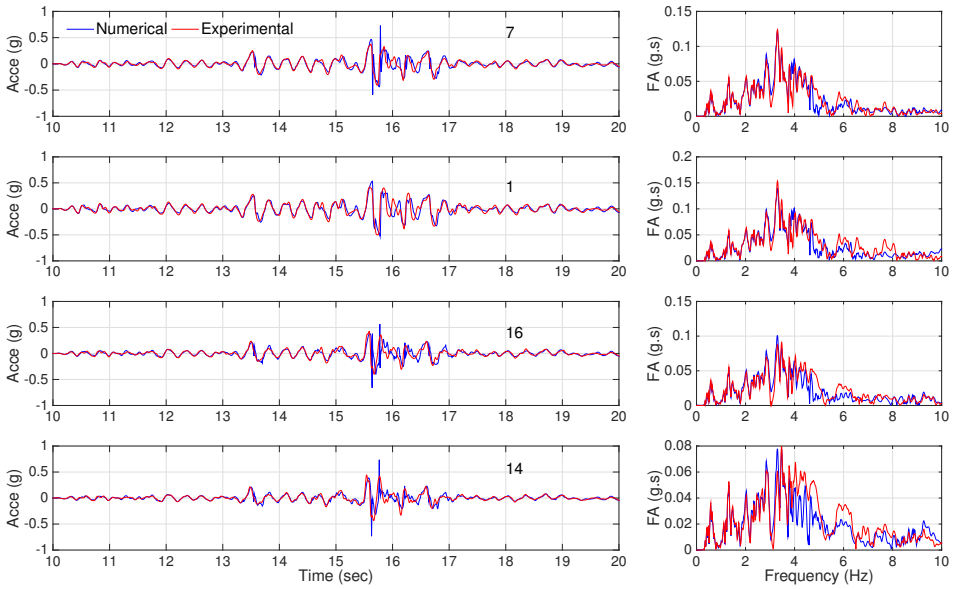

Figure 6.30: Time series and Fourier amplitude spectra of the horizontal accelerations recorded on the specimen structures (7, 1, 16 and 14) for motion #10.

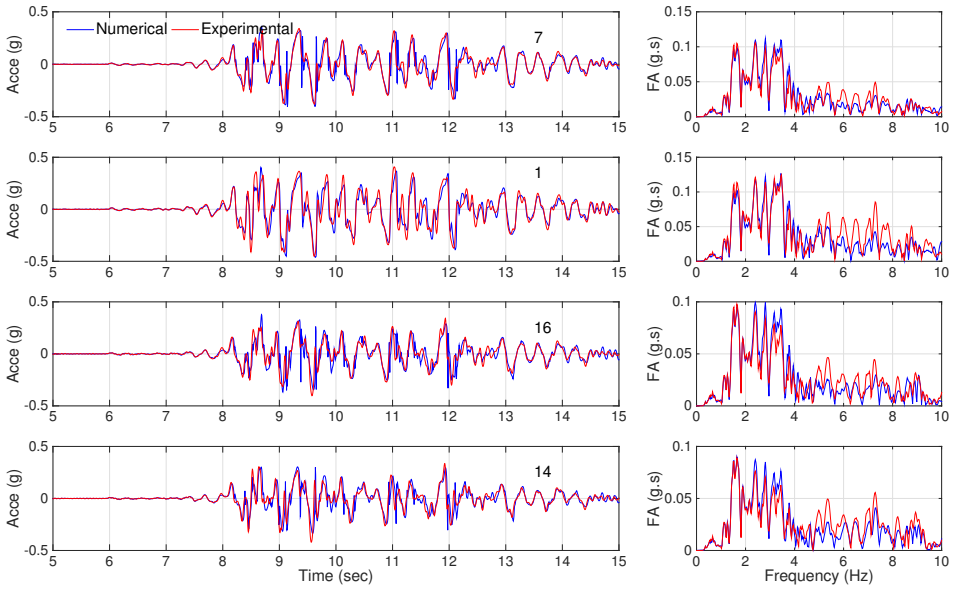

Figure 6.31: Time series and Fourier amplitude spectra of the horizontal accelerations recorded on the specimen structures (7, 1, 16 and 14) for motion #11.

6.4.3 Comparison of in-plane bending strains for rectangular culvert

To compare the maximum bending strain profiles, we used the processed strain data of each event to determine the maximum in-plane bending strains among all the recorded data on the rectangular structure and the time it occurred. Then, we read the value of bending strains at all locations at that particular time. We followed the same procedure to extract the bending strain profile from the numerical simulations. Figures 6.32-6.49 display the comparisons for the time series and Fourier amplitude spectra of the dynamic bending strains for the rectangular culvert, and Figures 6.50-6.58 display the comparisons for both static and dynamic bending strain profiles. Again, as shown, the numerical model was successful in capturing bending strain data for all (low, medium, high amplitude) base shaking events.

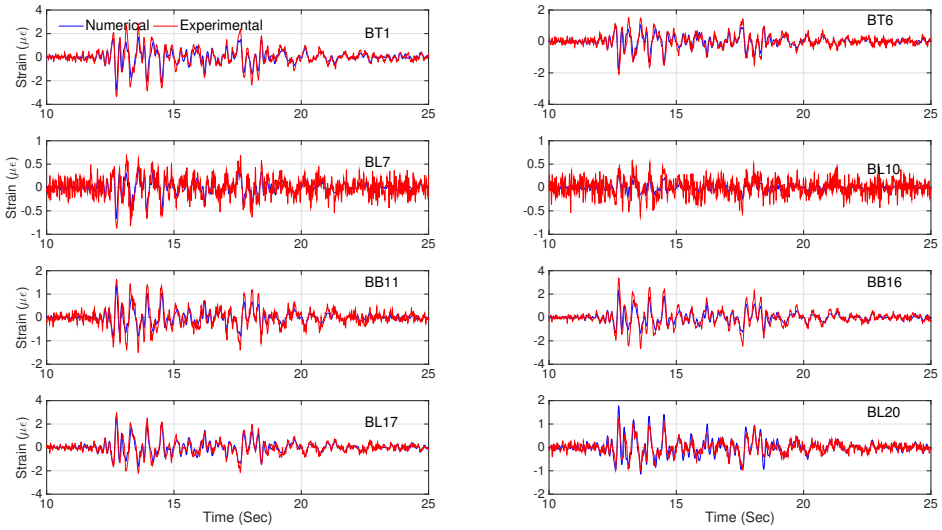

Figure 6.32: Comparison of the time series of the dynamic bending strains of the rectangular structure for motion #03.

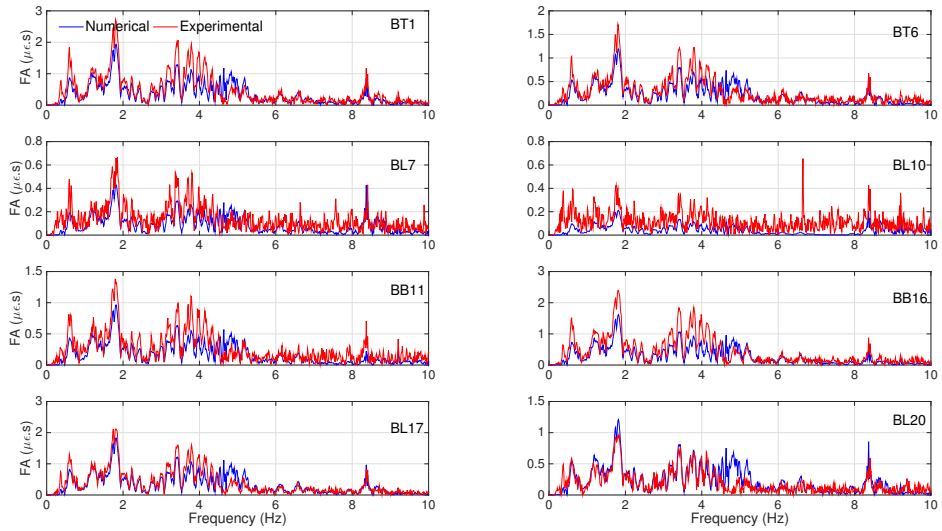

Figure 6.33: Comparison of the Fourier amplitude spectra of the rectangular structure for motion #03.

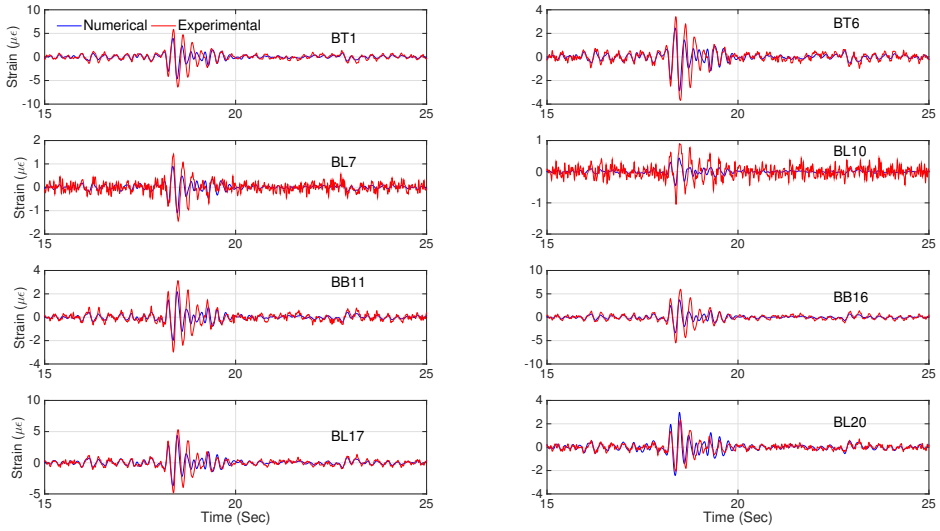

Figure 6.34: Comparison of the time series of the dynamic bending strains of the rectangular structure for motion #04.

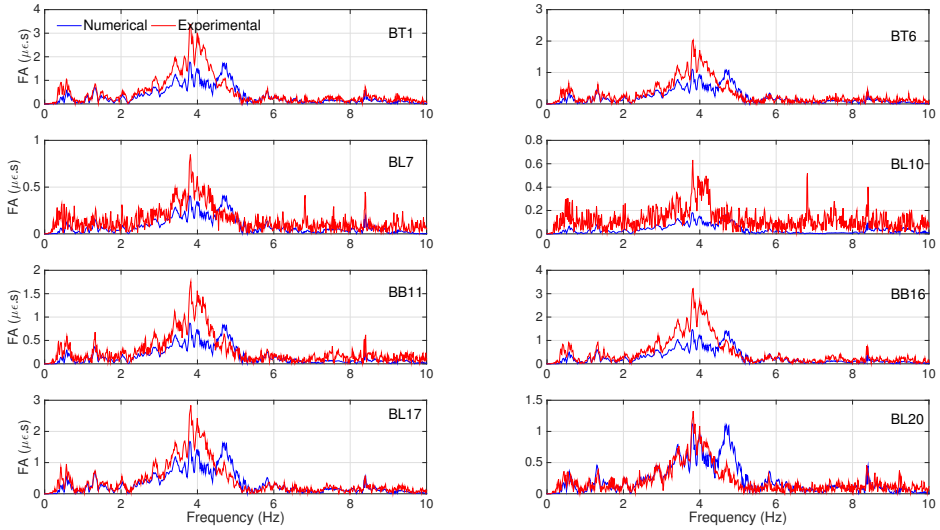

Figure 6.35: Comparison of the Fourier amplitude spectra of the rectangular structure for motion #04.

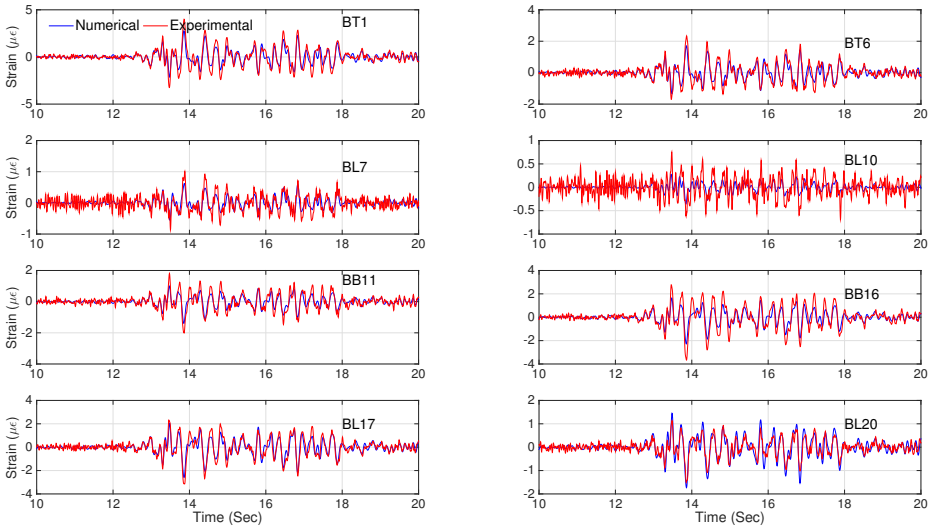

Figure 6.36: Comparison of the time series of the dynamic bending strains of the rectangular structure for motion #05.

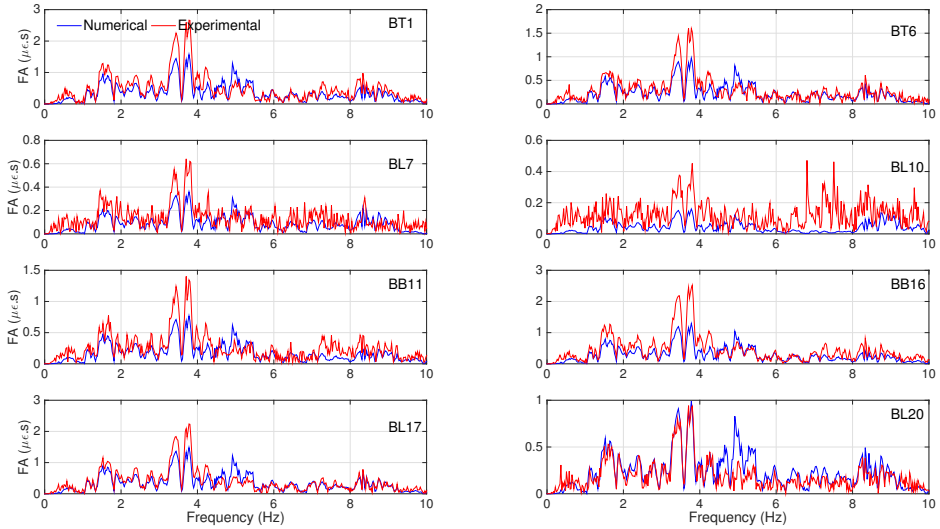

Figure 6.37: Comparison of the Fourier amplitude spectra of the rectangular structure for motion #05.

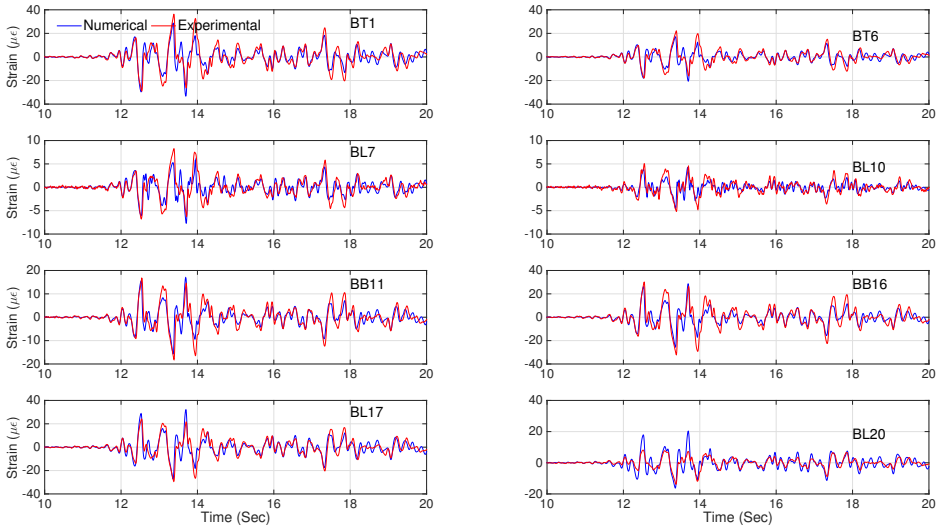

Figure 6.38: Comparison of the time series of the dynamic bending strains of the rectangular structure for motion #06.

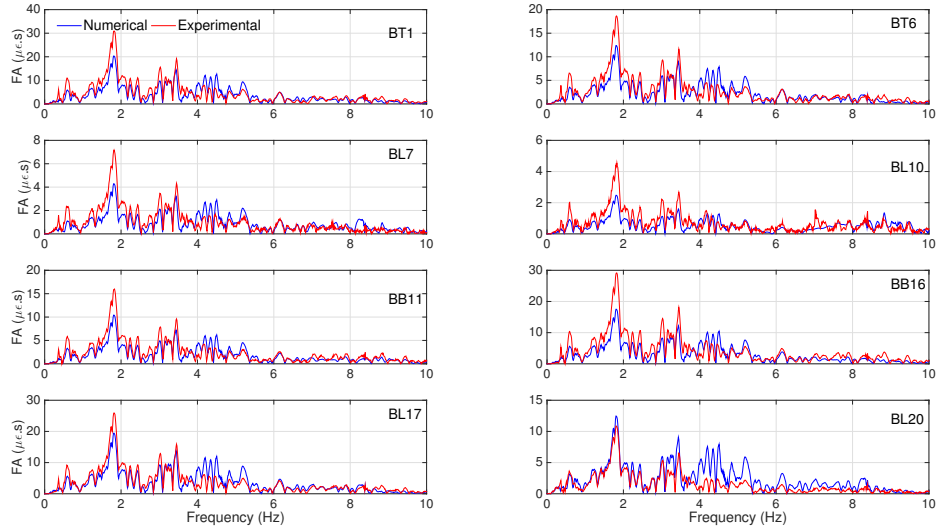

Figure 6.39: Comparison of the Fourier amplitude spectra of the rectangular structure for motion #06.

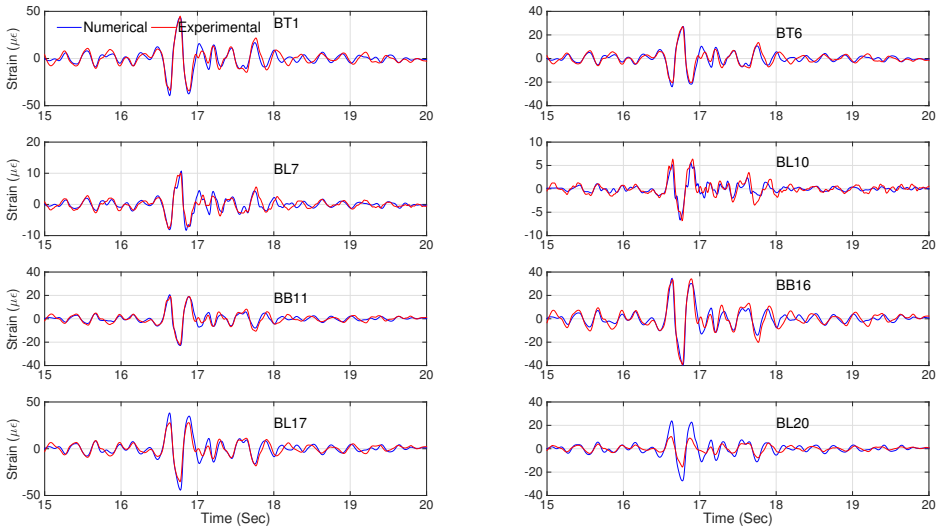

Figure 6.40: Comparison of the time series of the dynamic bending strains of the rectangular structure for motion #07.

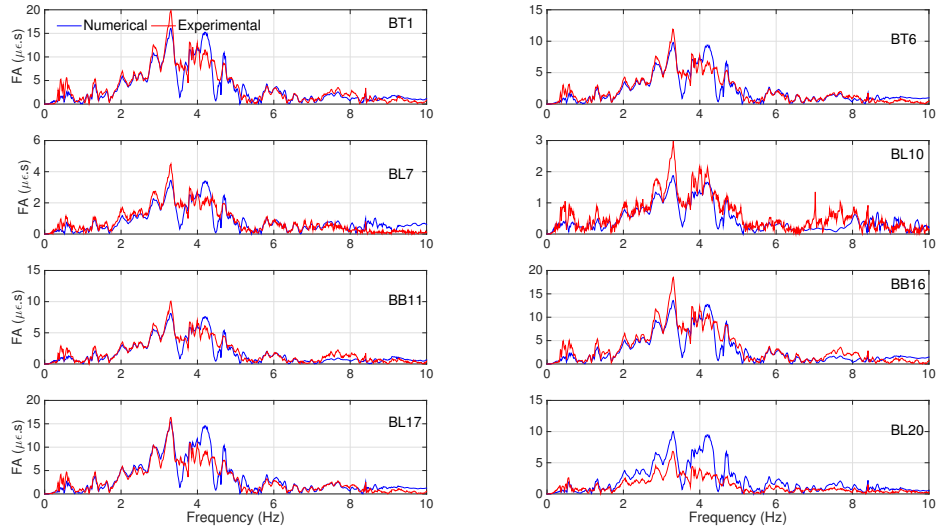

Figure 6.41: Comparison of the Fourier amplitude spectra of the rectangular structure for motion #07.

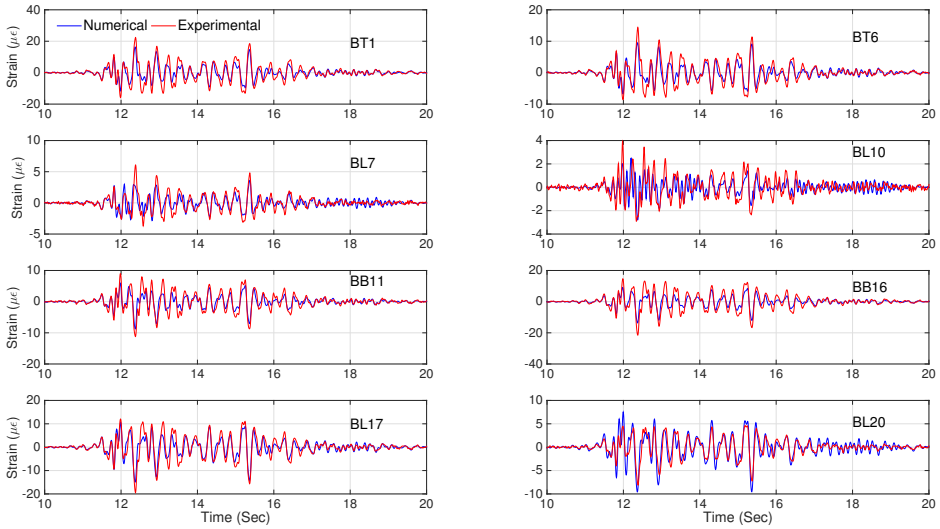

Figure 6.42: Comparison of the time series of the dynamic bending strains of the rectangular structure for motion #08.

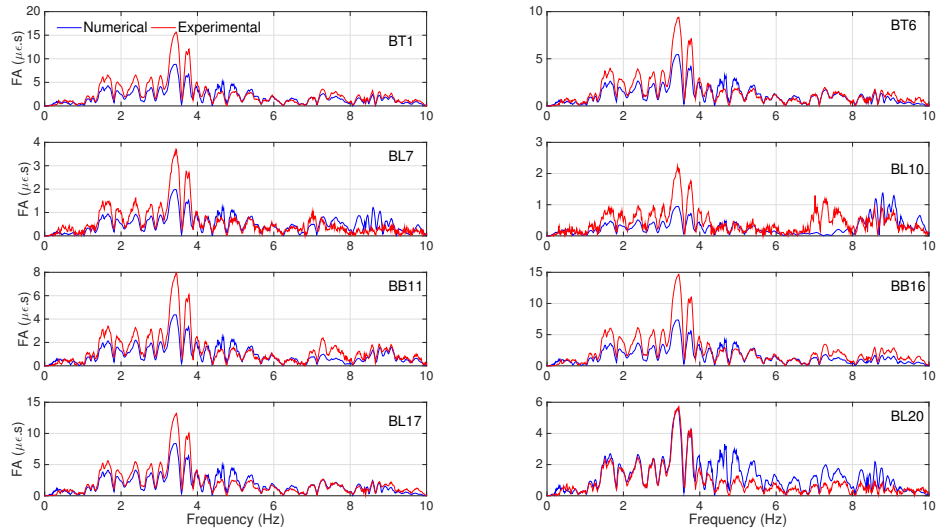

Figure 6.43: Comparison of the Fourier amplitude spectra of the rectangular structure for motion #08.

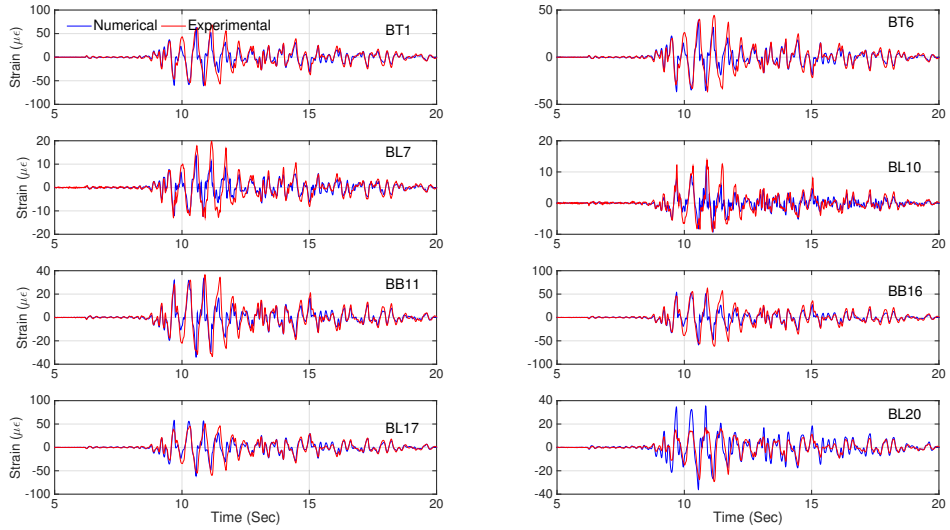

Figure 6.44: Comparison of the time series of the dynamic bending strains of the rectangular structure for motion #09.

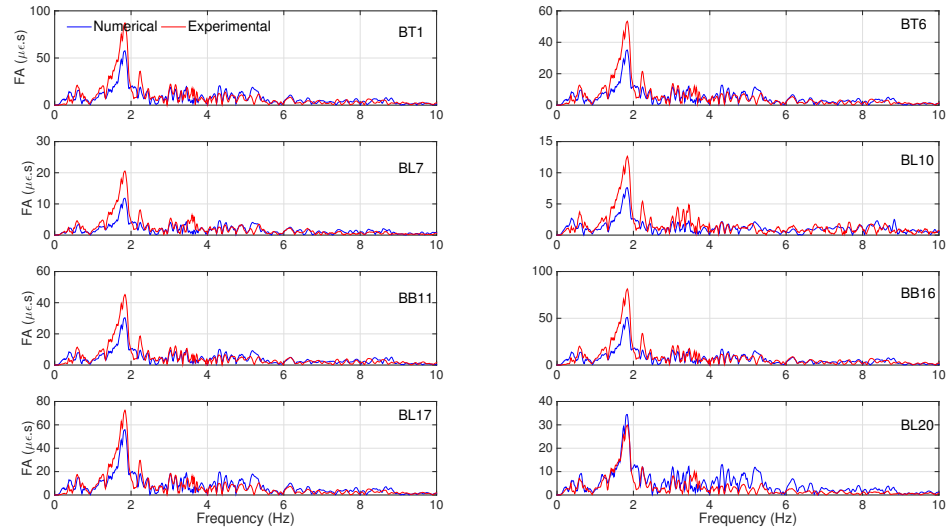

Figure 6.45: Comparison of the Fourier amplitude spectra of the rectangular structure for motion #09.

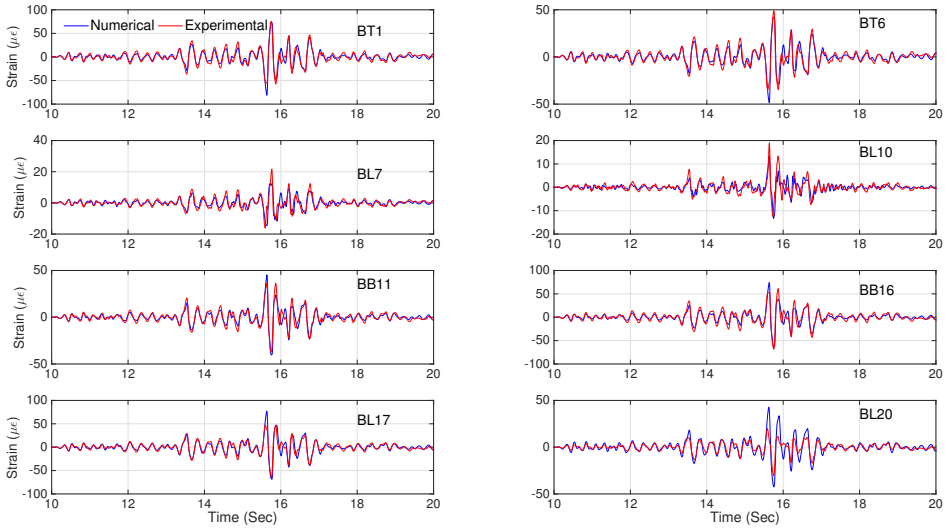

Figure 6.46: Comparison of the time series of the dynamic bending strains of the rectangular structure for motion #10.

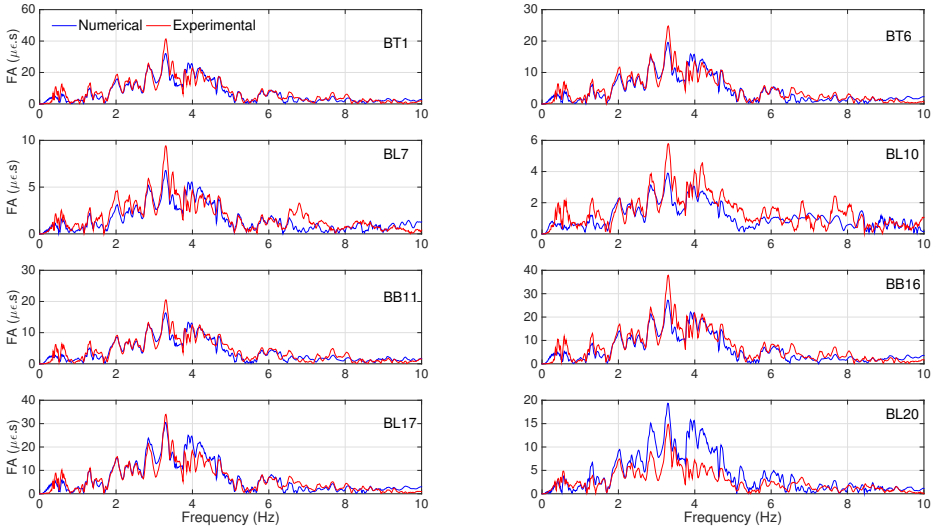

Figure 6.47: Comparison of the Fourier amplitude spectra of the rectangular structure for motion #10.

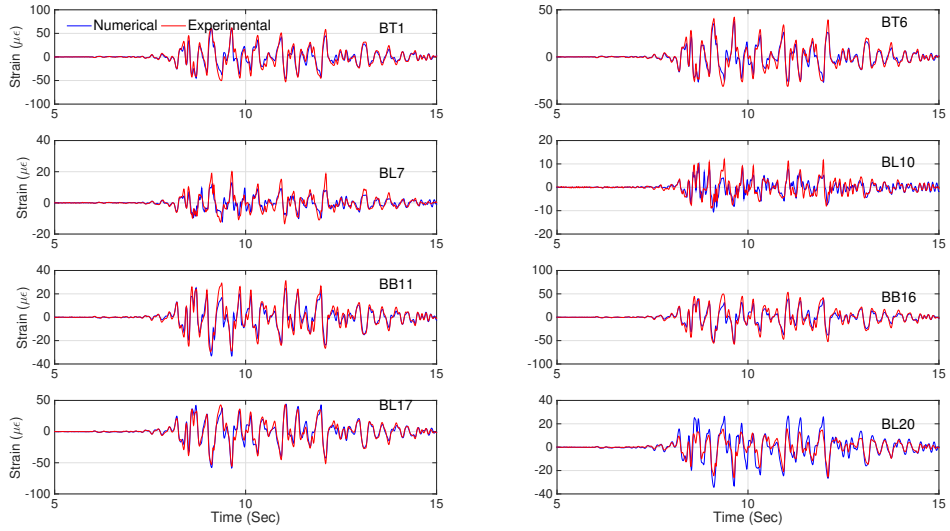

Figure 6.48: Comparison of the time series of the dynamic bending strains of the rectangular structure for motion #11.

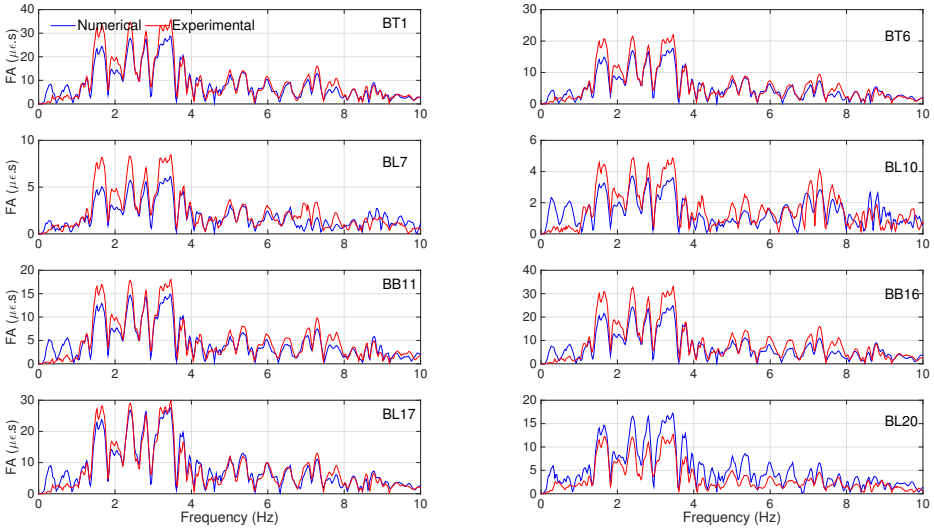

Figure 6.49: Comparison of the Fourier amplitude spectra of the rectangular structure for motion #11.

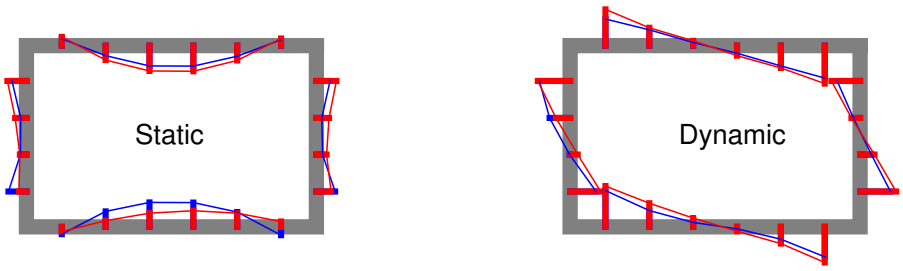

Figure 6.50: Comparison of the maximum static and dynamic bending strain profiles of the rectangular structure for motion #03.

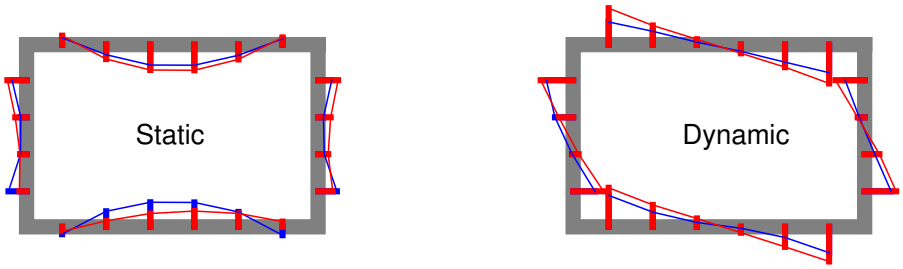

Figure 6.51: Comparison of the maximum static and dynamic bending strain profiles of the rectangular structure for motion #04.

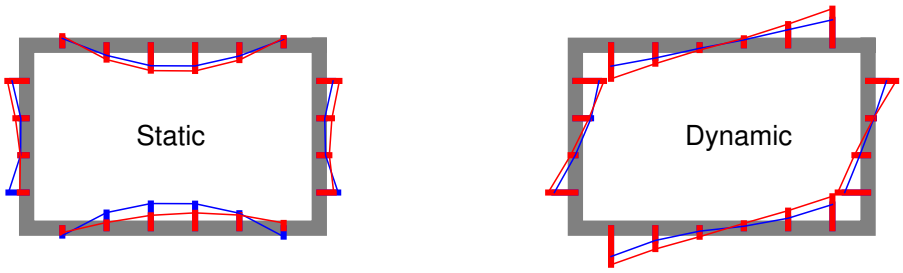

Figure 6.52: Comparison of the maximum static and dynamic bending strain profiles of the rectangular structure for motion #05.

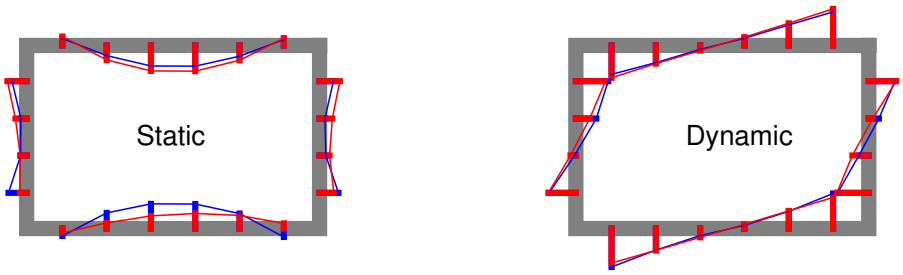

Figure 6.53: Comparison of the maximum static and dynamic bending strain profiles of the rectangular structure for motion #06.

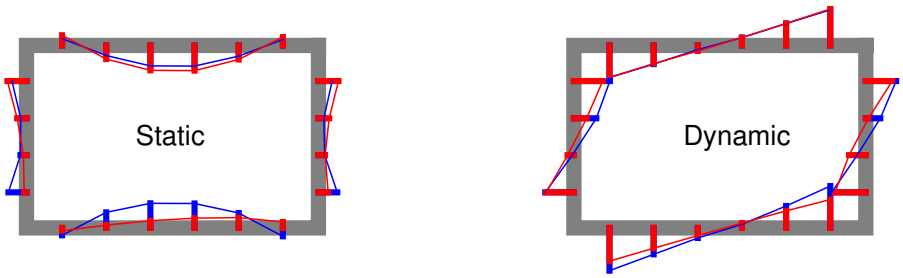

Figure 6.54: Comparison of the maximum static and dynamic bending strain profiles of the rectangular structure for motion #07.

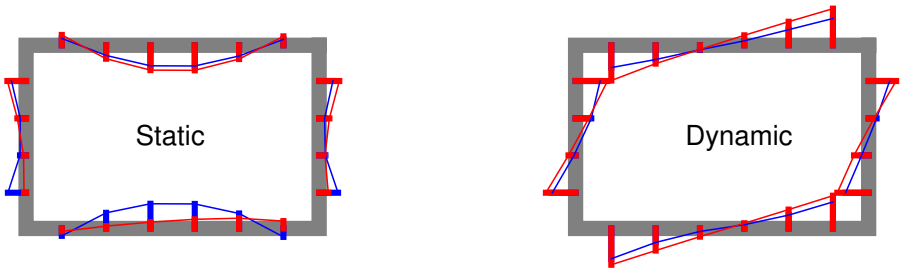

Figure 6.55: Comparison of the maximum static and dynamic bending strain profiles of the rectangular structure for motion #08.

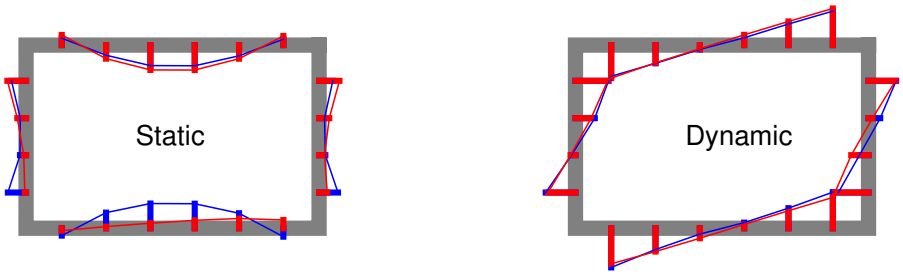

Figure 6.56: Comparison of the maximum static and dynamic bending strain profiles of the rectangular structure for motion #09.

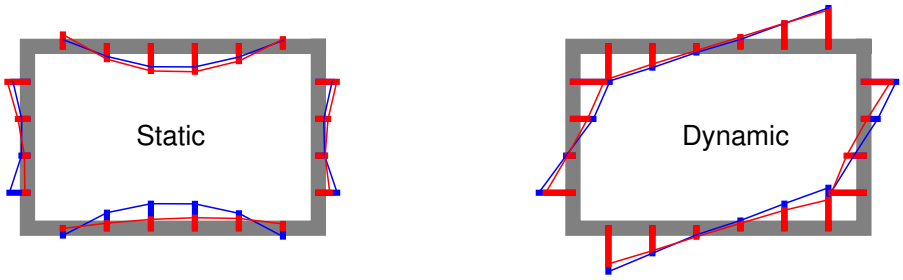

Figure 6.57: Comparison of the maximum static and dynamic bending strain profiles of the rectangular structure for motion #10.

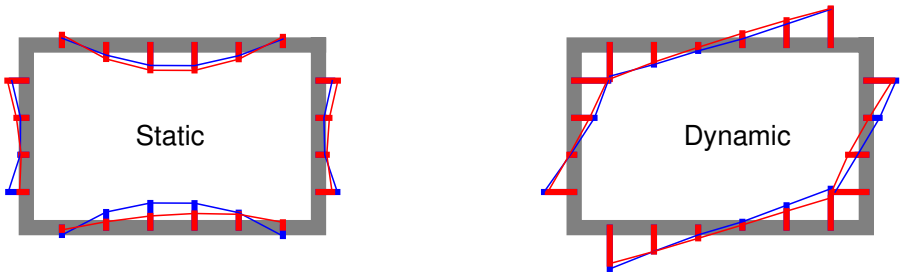

Figure 6.58: Comparison of the maximum static and dynamic bending strain profiles of the rectangular structure for motion #11.

6.4.4 Comparison of in-plane bending strains for circular culvert

Similarly, Figures 6.59-6.76 display the comparisons for the time series and Fourier amplitude spectra of the dynamic bending strains for the circular culvert, and Figures 6.77-6.85 display the comparisons for both static and dynamic bending strain profiles. As shown, the numerical model approach is again successful in general to capture bending strain time series. However, agreements are not perfect at all locations. Moreover, although the numerical model is successful in capturing the dynamic strain profile, it was unable to do so for the static case. This can be partially attributed to the fact that we are not modeling the soil densification in our numerical simulations and the initial condition is the same for all experiments. This is while in the actual centrifuge experiment we possibly had some soil densification around the circular structure as it was difficult to pluviate soil uniformly, and we had to use a hand vibrator to increase soil densification around it prior to the test. It is likely that this effort was not entirely successful. That said, the static strains are much smaller than the dynamic strains, and are incidentally more difficult to measure.

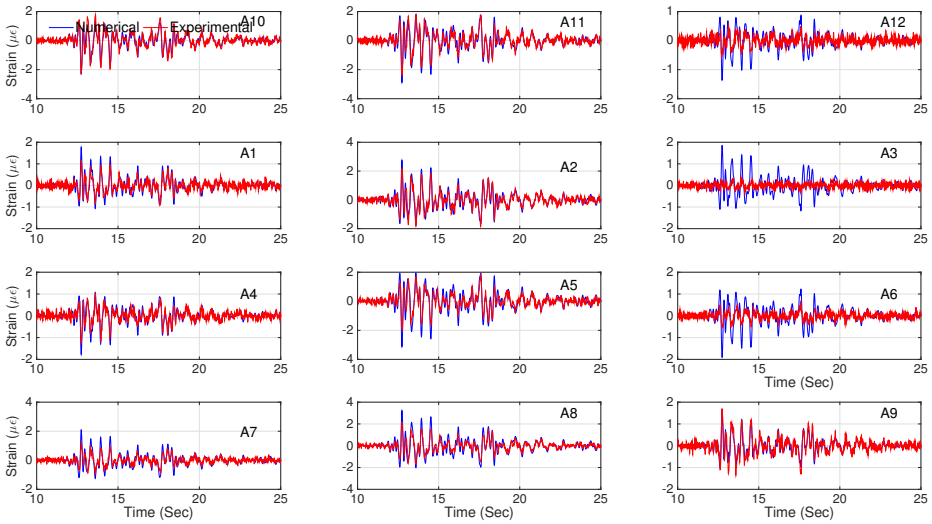

Figure 6.59: Comparison of the time series of the dynamic bending strains of the circular structure for motion #03.

6.4.5 Comparison of hoop strains for circular culvert

Figures 6.86-6.103 display the comparisons for the time series and Fourier amplitude spectra of hoop strains for the circular culvert, and Figures 6.104-6.112 show comparisons for both the static and dynamic hoop strain profiles. In general, the range of hoop strains are

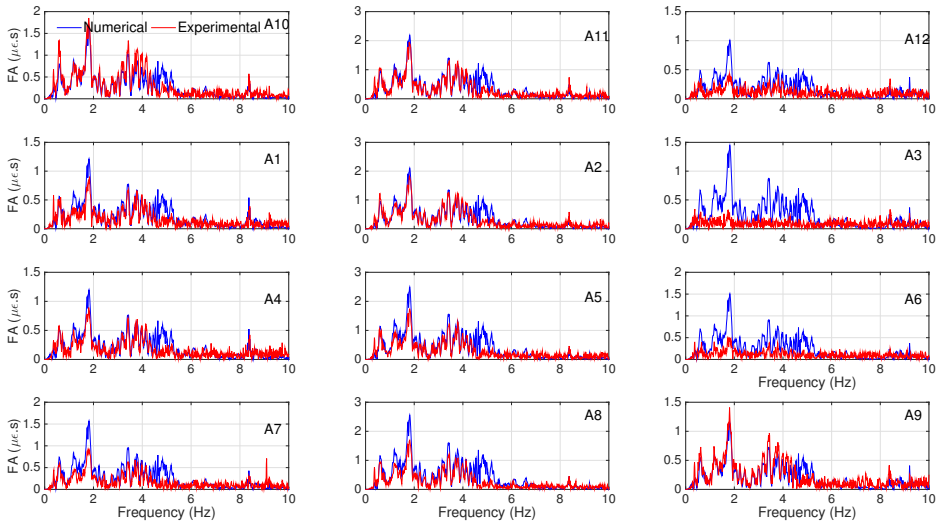

Figure 6.60: Comparison of Fourier amplitude spectra of the circular structure for motion #03.

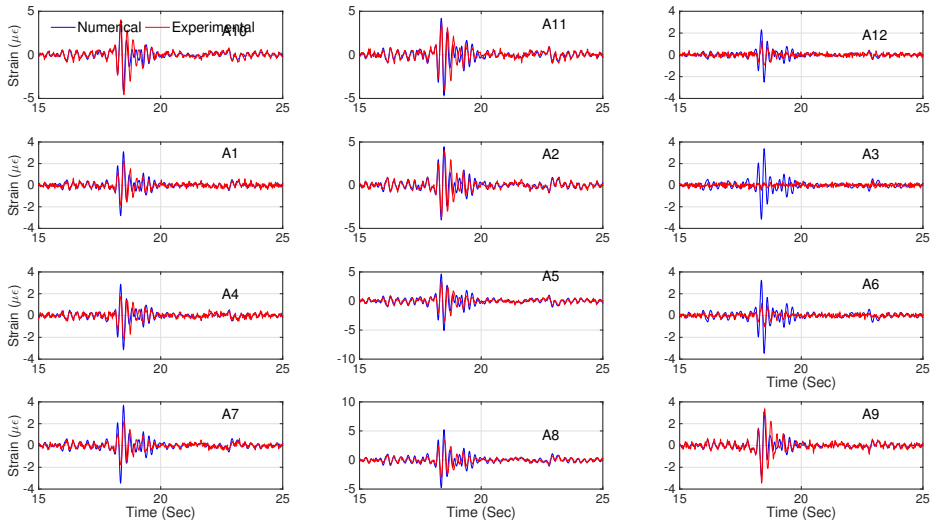

Figure 6.61: Comparison of the time series of the dynamic bending strains of the circular structure for motion #04.

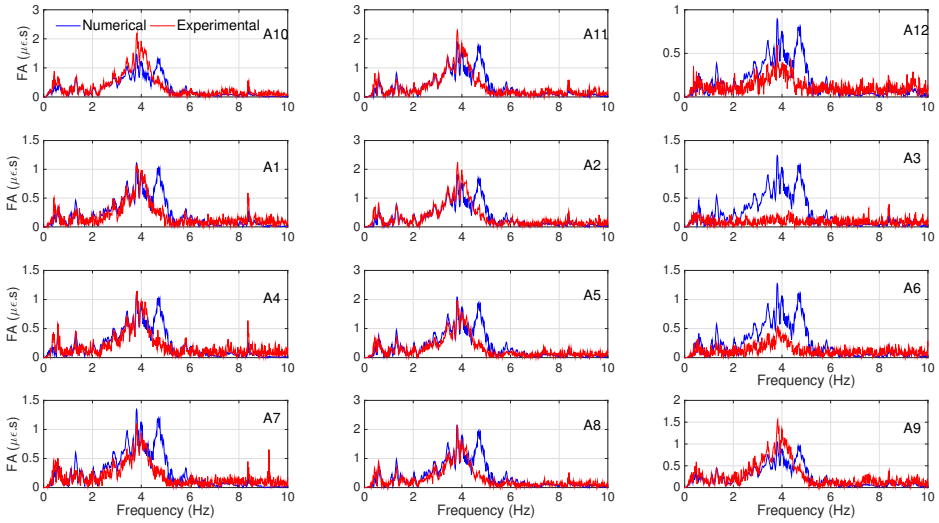

Figure 6.62: Comparison of the Fourier amplitude spectra of the circular structure for motion #04.

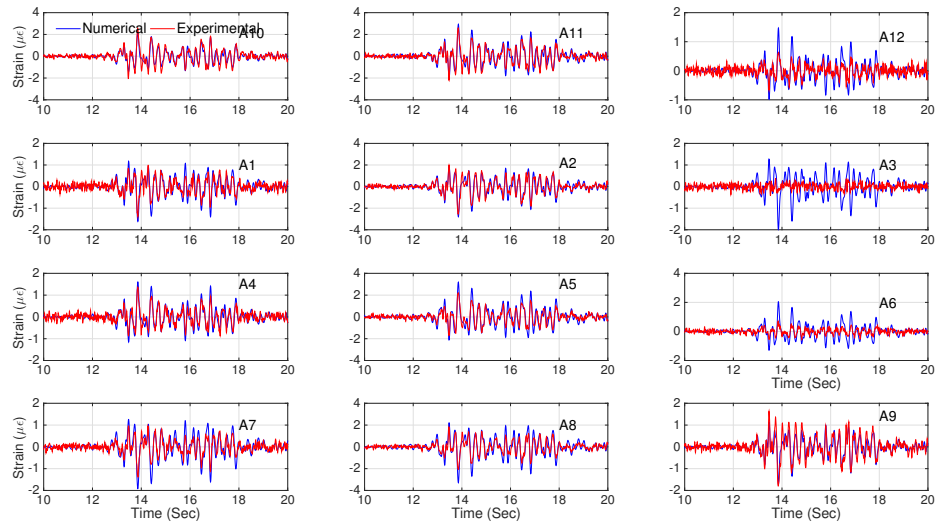

Figure 6.63: Comparison of the time series of the dynamic bending strains of the circular structure for motion #05.

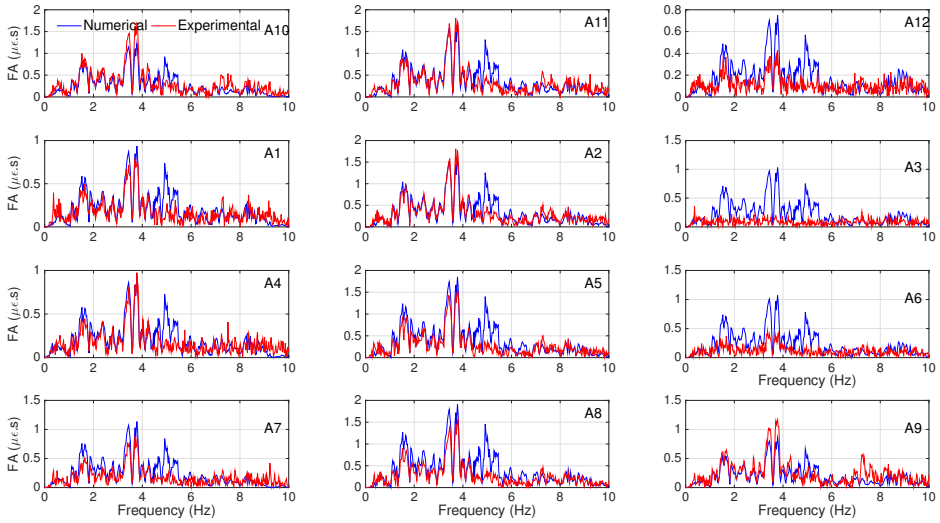

Figure 6.64: Comparison of the Fourier amplitude spectra of the circular structure for motion #05.

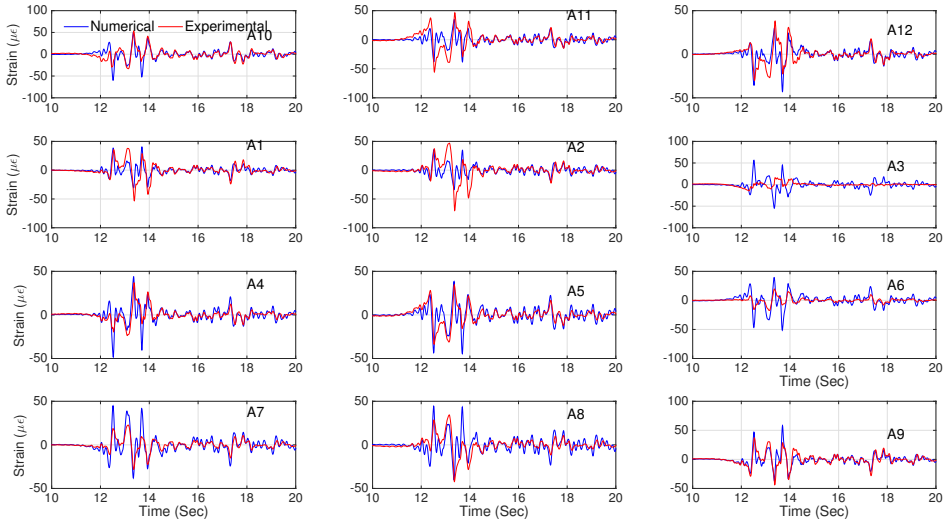

Figure 6.65: Comparison of the time series of the dynamic bending strains of the circular structure for motion #06.

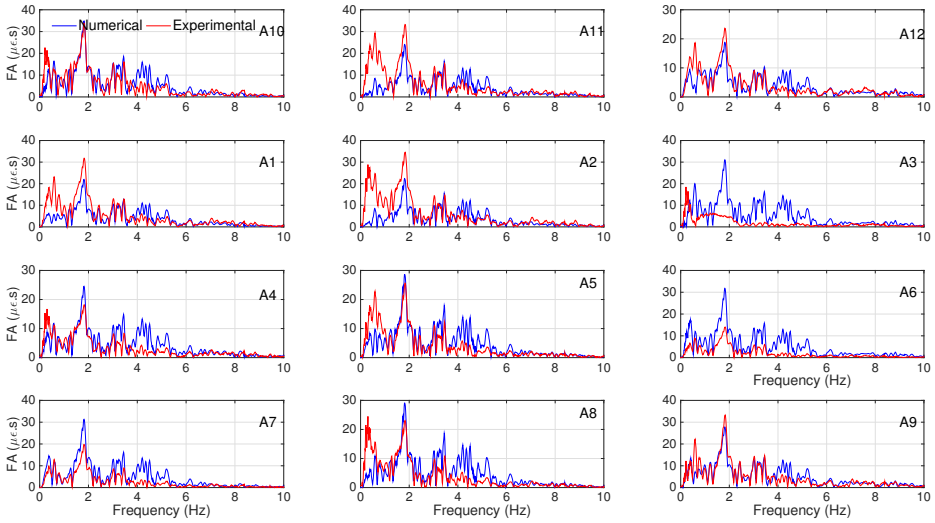

Figure 6.66: Comparison of the Fourier amplitude spectra of the circular structure for motion #06.

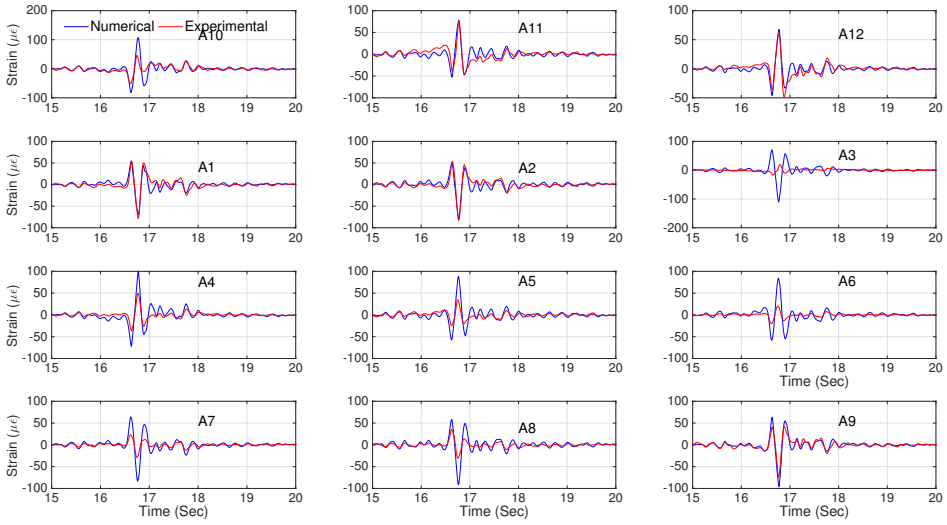

Figure 6.67: Comparison of the time series of the dynamic bending strains of the circular structure for motion #07.

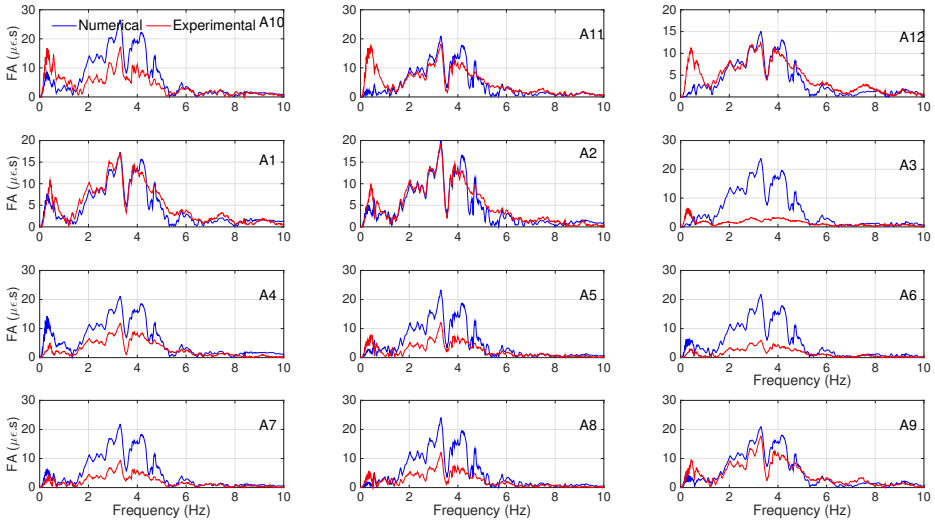

Figure 6.68: Comparison of the Fourier amplitude spectra of the circular structure for motion #07.

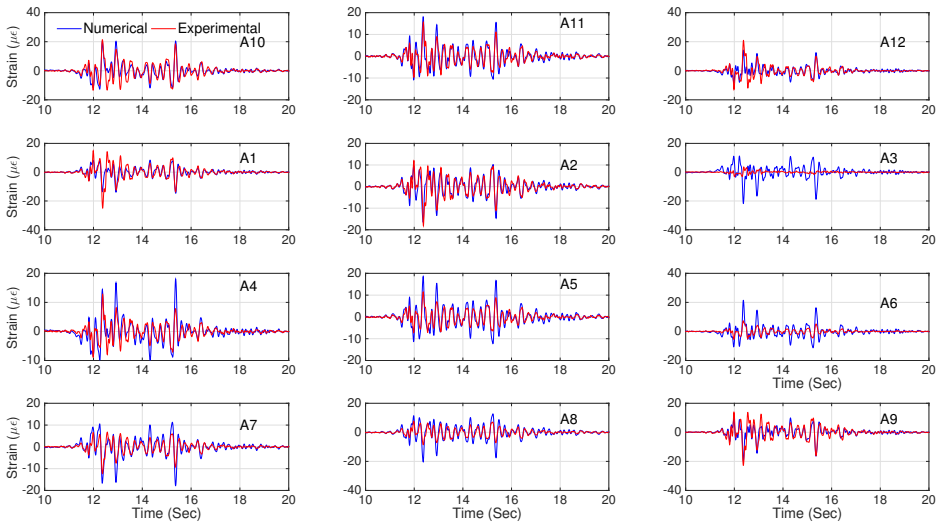

Figure 6.69: Comparison of the time series of the dynamic bending strains of the circular structure for motion #08.

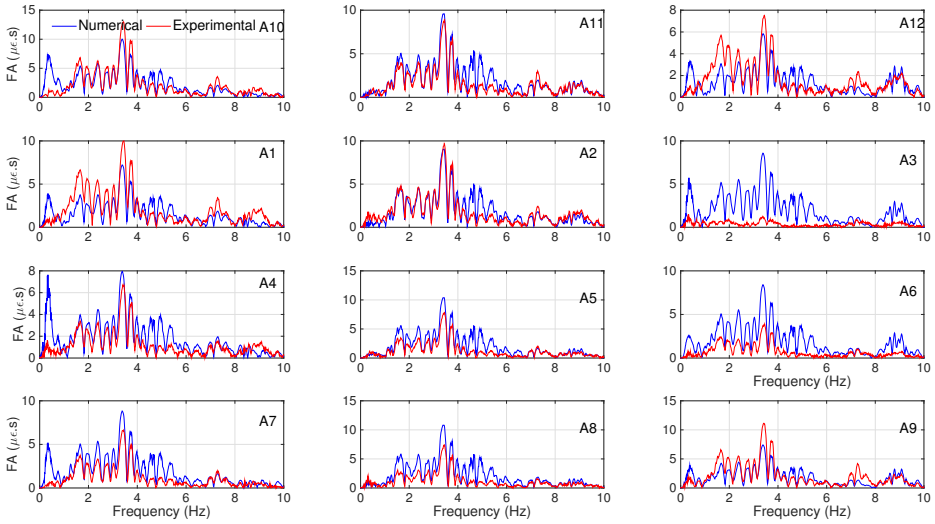

Figure 6.70: Comparison of the corresponding Fourier amplitude spectra of the circular structure for motion #08.

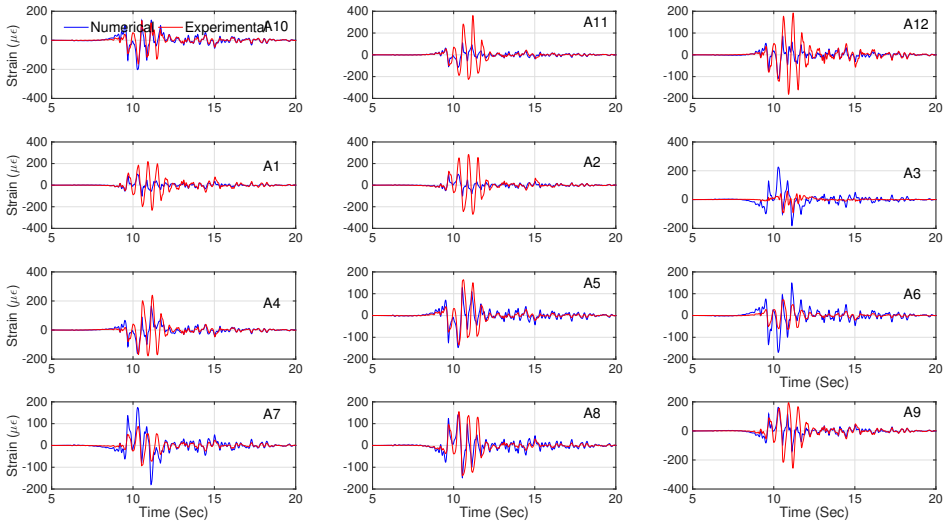

Figure 6.71: Comparison of the time series of the dynamic bending strains of the circular structure for motion #09.

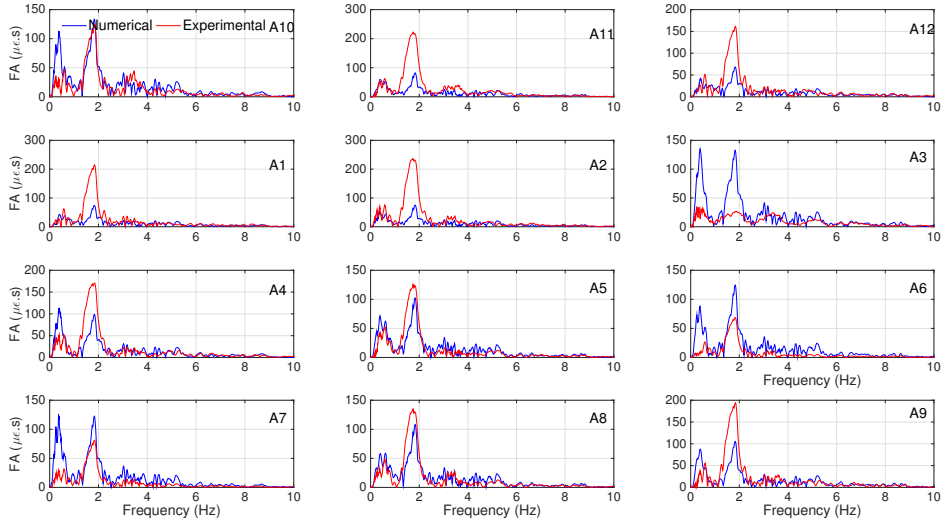

Figure 6.72: Comparison of the Fourier amplitude spectra of the circular structure for motion #09.

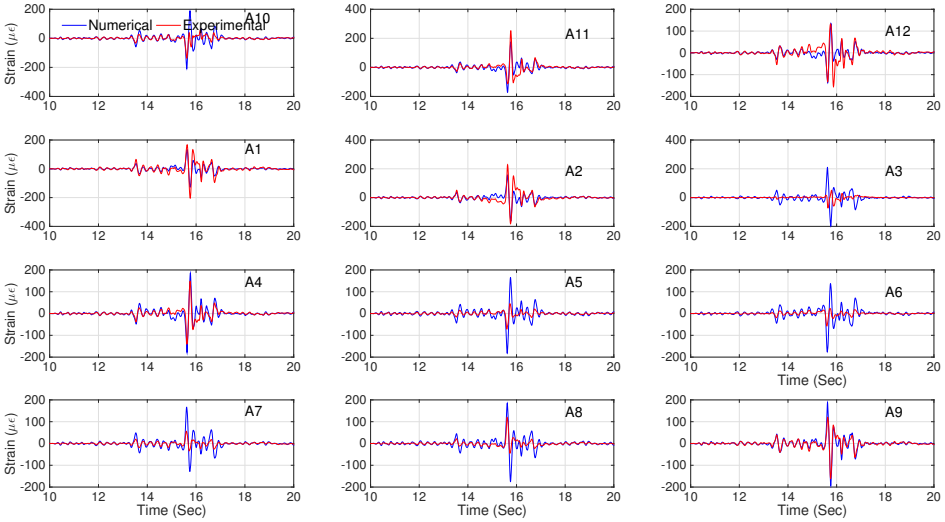

Figure 6.73: Comparison of the time series of the dynamic bending strains of the circular structure for motion #10.

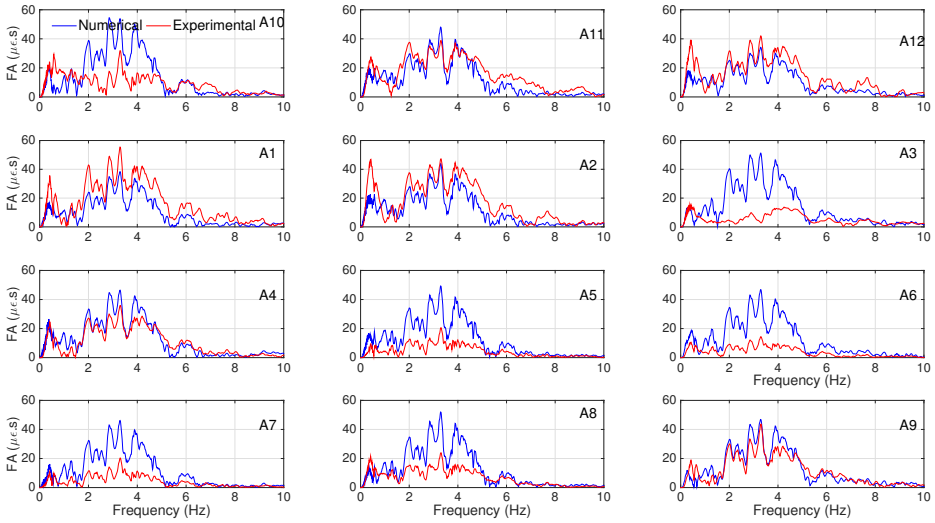

Figure 6.74: Comparison of the Fourier amplitude spectra of the circular structure for motion #10.

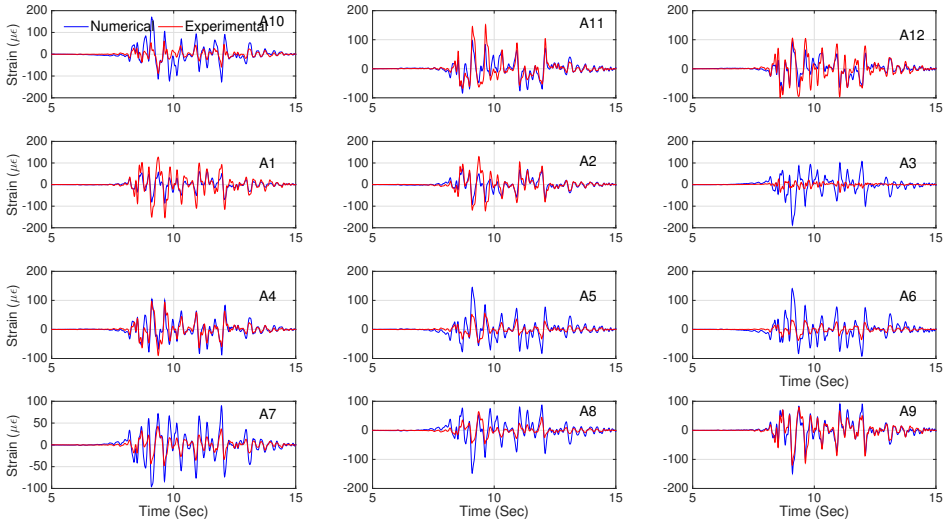

Figure 6.75: Comparison of the time series of the dynamic bending strains of the circular structure for motion #11.

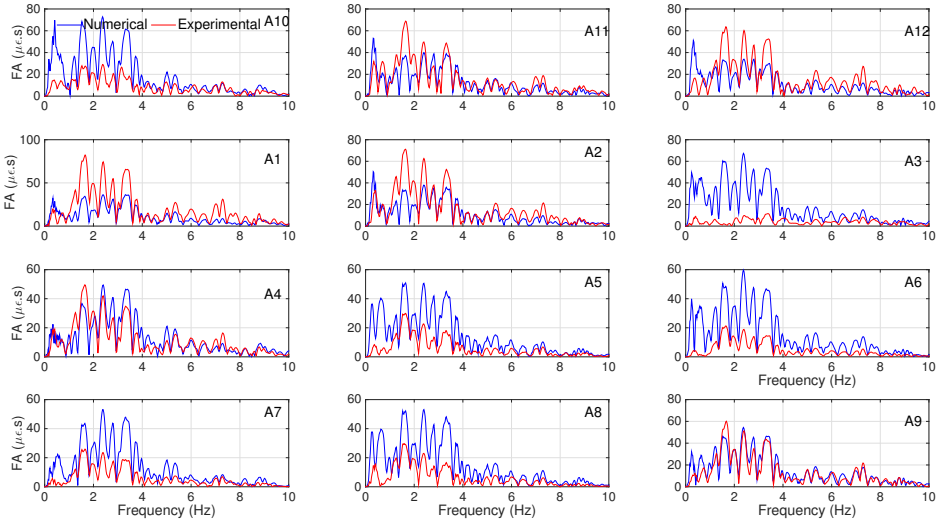

Figure 6.76: Comparison of the Fourier amplitude spectra of the circular structure for motion #11.

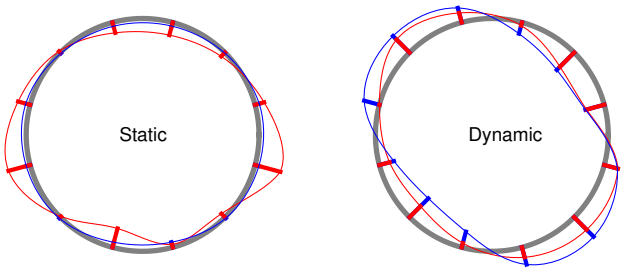

Figure 6.77: Comparison of the maximum static and dynamic bending strain profiles of the circular structure for motion #03.

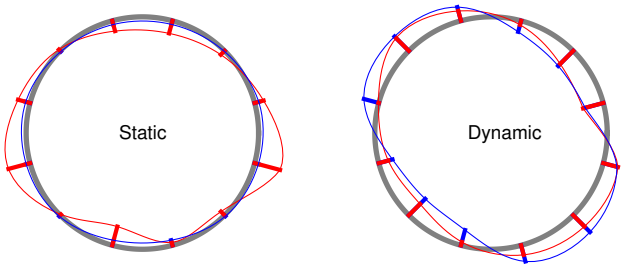

Figure 6.78: Comparison of the maximum static and dynamic bending strain profiles of the circular structure for motion #04.

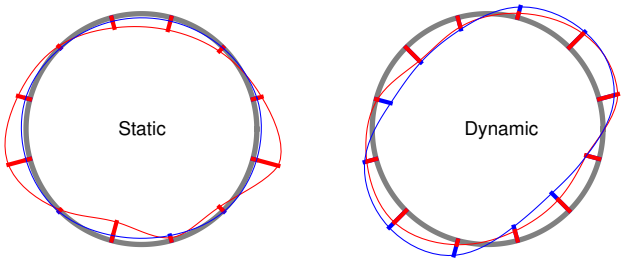

Figure 6.79: Comparison of the maximum static and dynamic bending strain profiles of the circular structure for motion #05.

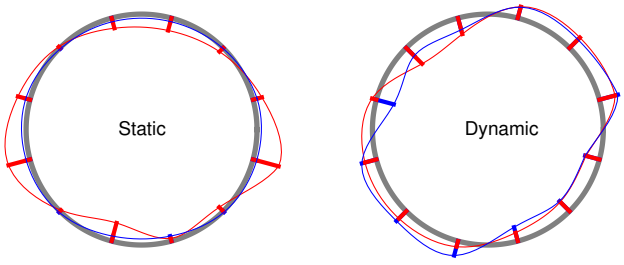

Figure 6.80: Comparison of the maximum static and dynamic bending strain profiles of the circular structure for motion #06.

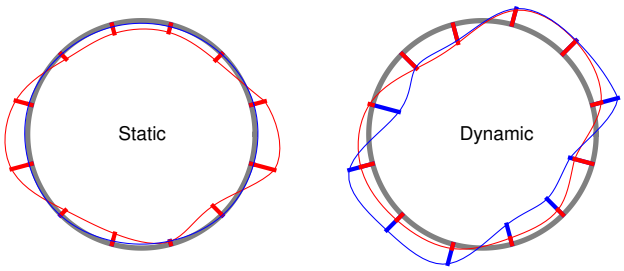

Figure 6.81: Comparison of the maximum static and dynamic bending strain profiles of the circular structure for motion #07.

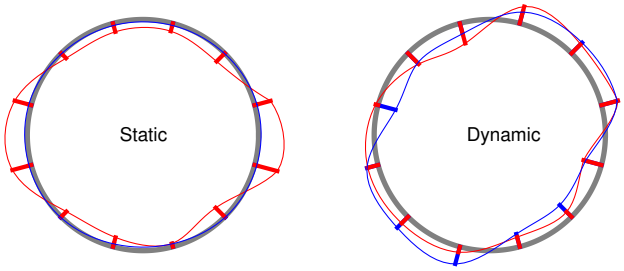

Figure 6.82: Comparison of the maximum static and dynamic bending strain profiles of the circular structure for motion #08.

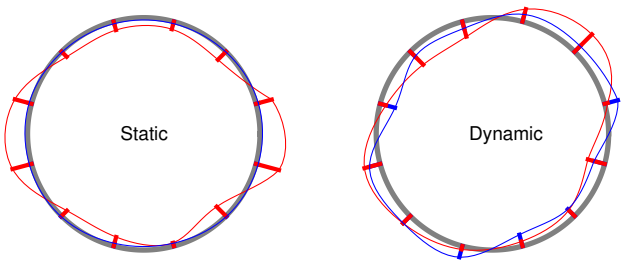

Figure 6.83: Comparison of the maximum static and dynamic bending strain profiles of the circular structure for motion #09.

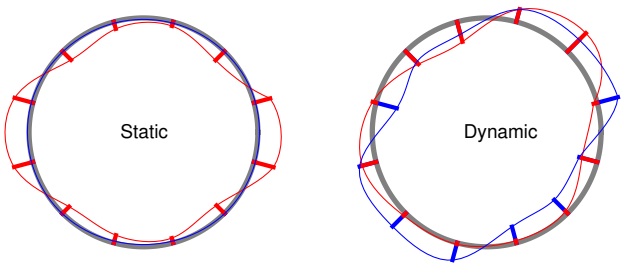

Figure 6.84: Comparison of the maximum static and dynamic bending strain profiles of the circular structure for motion #10.

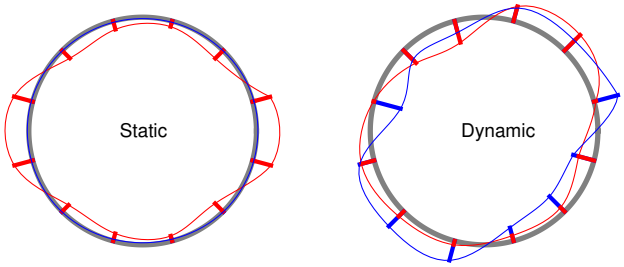

Figure 6.85: Comparison of the maximum static and dynamic bending strain profiles of the circular structure for motion #11.

smaller than the bending strains, and as such, they inherently have inherently lower signal-to-noise ratios. Not surprisingly, therefore, we could achieve better agreements between experimental hoop strain data and FE results for higher amplitude motions. Although the agreement is not uniformly good at all locations, the numerical model could capture very similar static and dynamic hoop strain profiles in general; and interestingly, the static profile agreement is much better than what was observed for the static in-plane bending strains shown previously.

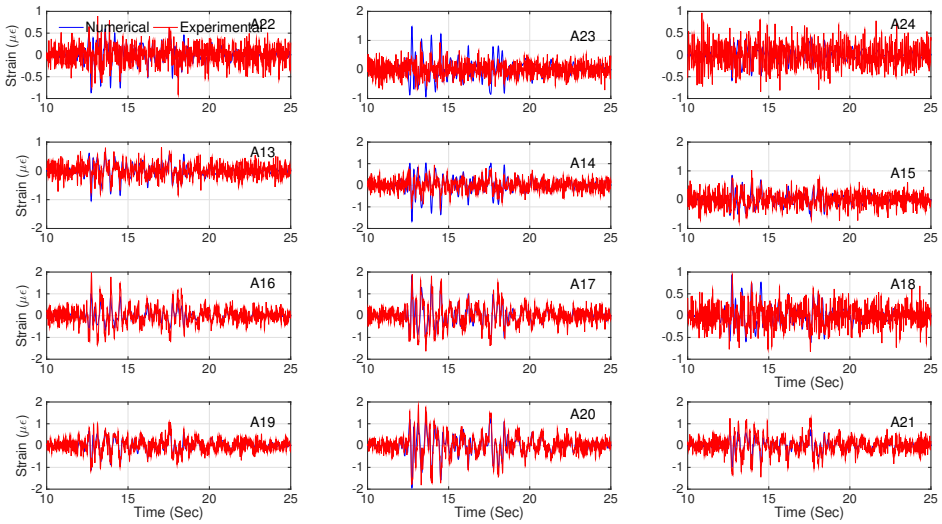

Figure 6.86: Comparison of the time series of the dynamic hoop strains of the circular structure for motion #03.

6.4.6 Maximum dynamic deformation profiles of culvert specimens

In order to investigate the dominant mode of deformation in both structures when the bending strain is maximum, we read the dynamic displacements of different nodes along the edge of the structure at the same time that we obtained the bending strain profiles. Figures 6.113 and 6.114 display the maximum deformation profiles for both the rectangular and the circular structure under all 9 motions. It should be noted that in both figures the resulting deformations are magnified 100 times.

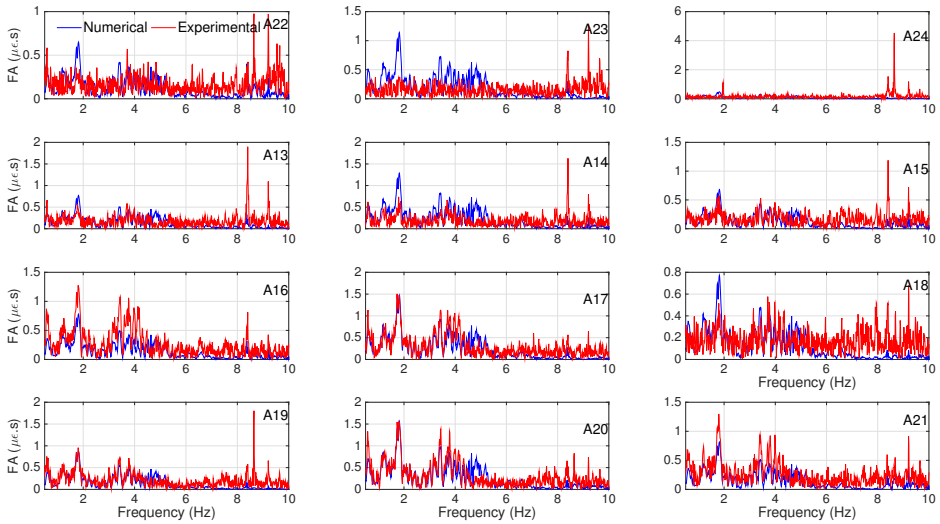

Figure 6.87: Comparison of the Fourier amplitude spectra of the circular structure for motion #03.

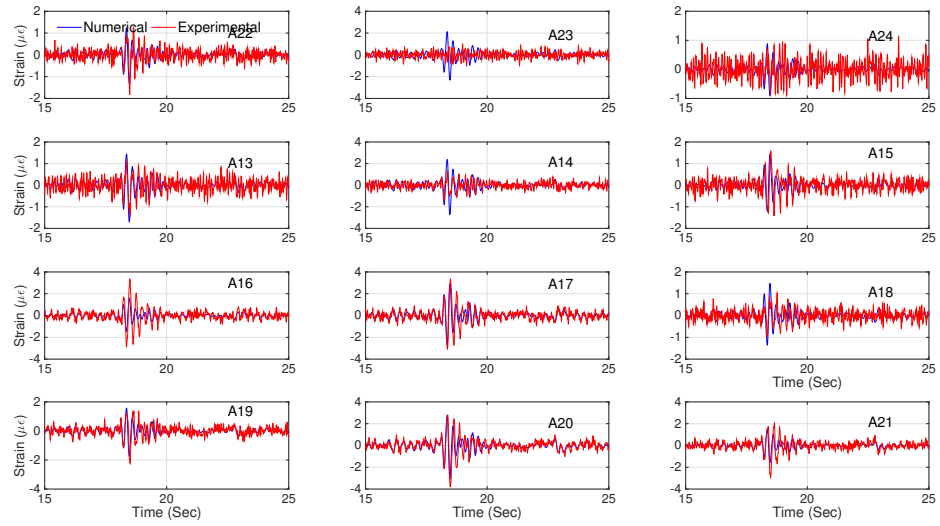

Figure 6.88: Comparison of the time series of the dynamic hoop strains of the circular structure for motion #04.

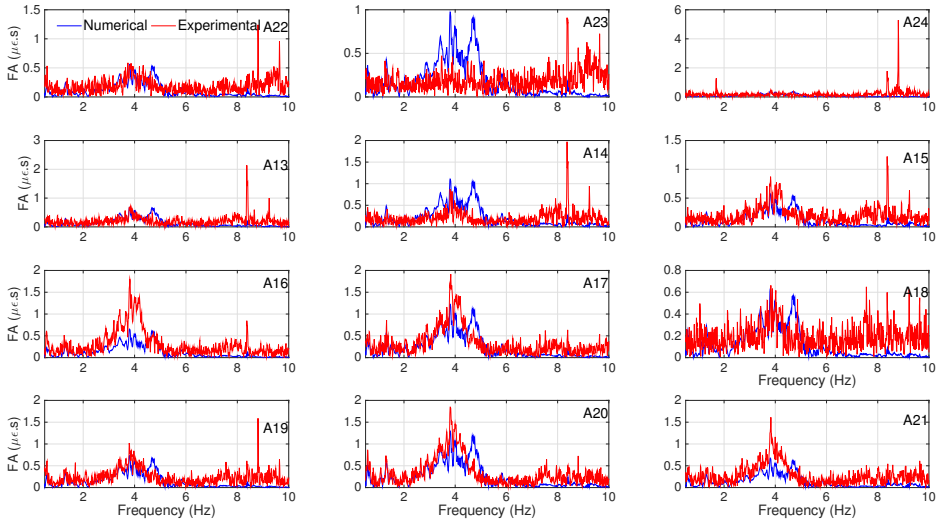

Figure 6.89: Comparison of the Fourier amplitude spectra of the circular structure for motion #04.

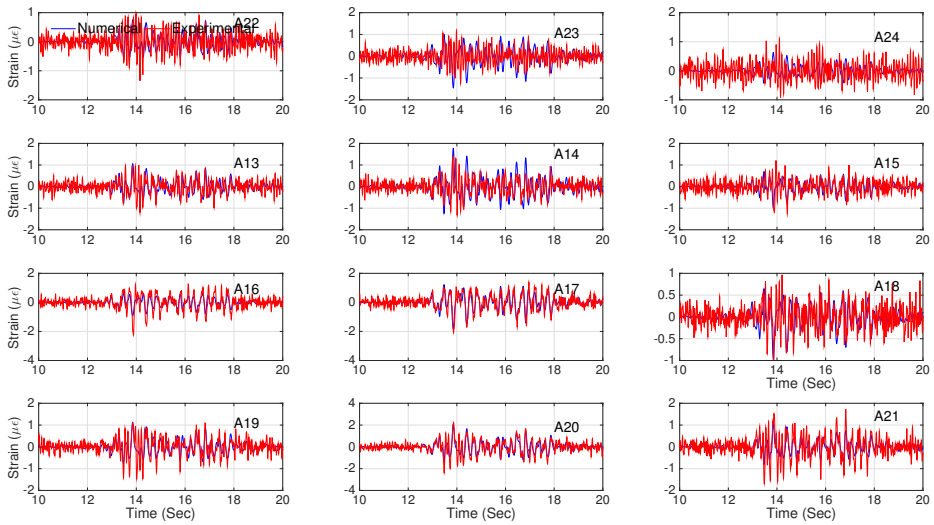

Figure 6.90: Comparison of the time series of the dynamic hoop strains of the circular structure for motion #05.

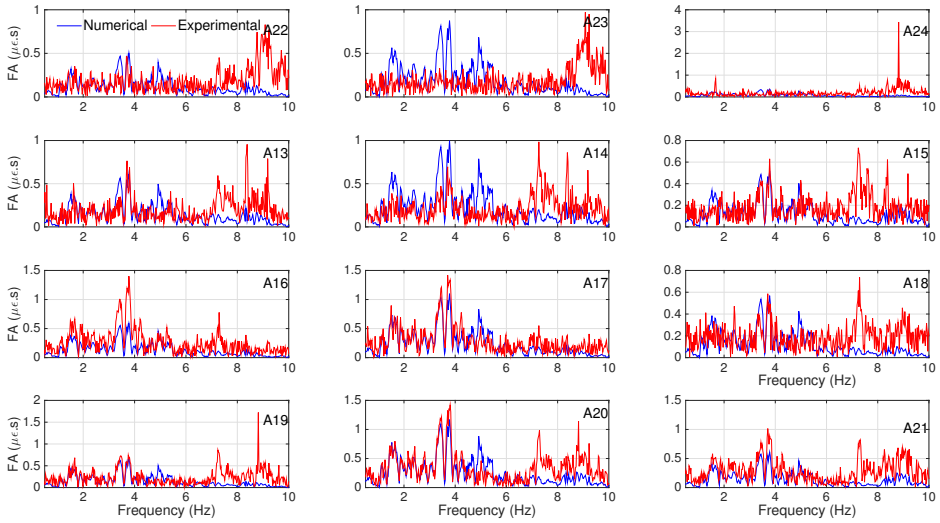

Figure 6.91: Comparison of the Fourier amplitude spectra of the circular structure for motion #05.

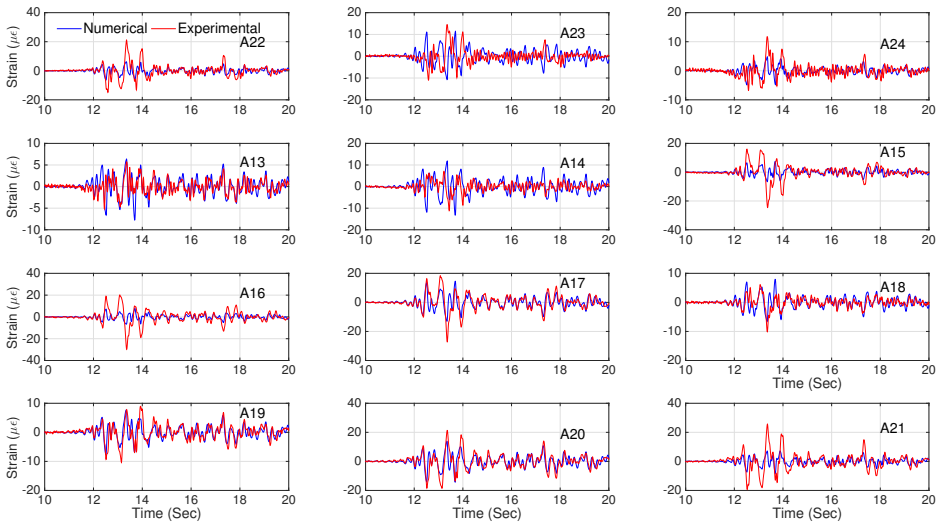

Figure 6.92: Comparison of the time series of the dynamic hoop strains of the circular structure for motion #06.

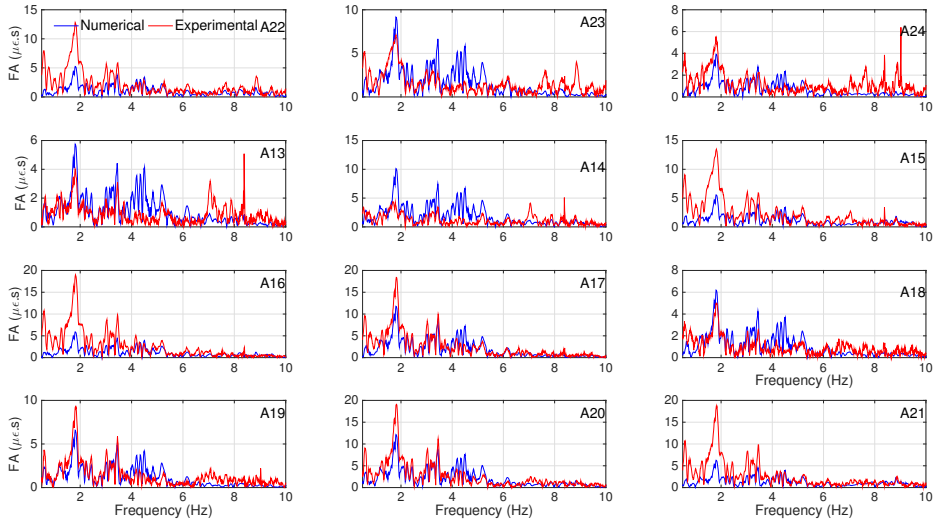

Figure 6.93: Comparison of the Fourier amplitude spectra of the circular structure for motion #06.

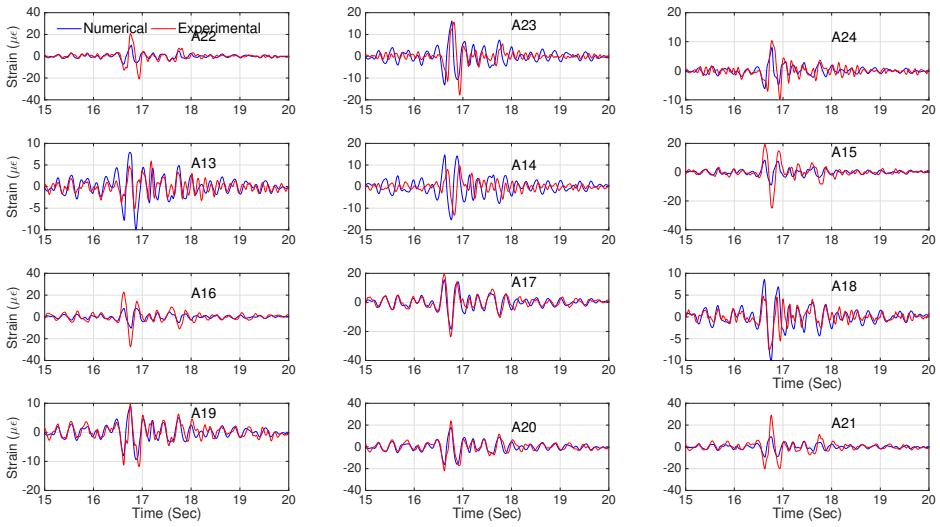

Figure 6.94: Comparison of the time series of the dynamic hoop strains of the circular structure for motion #07.

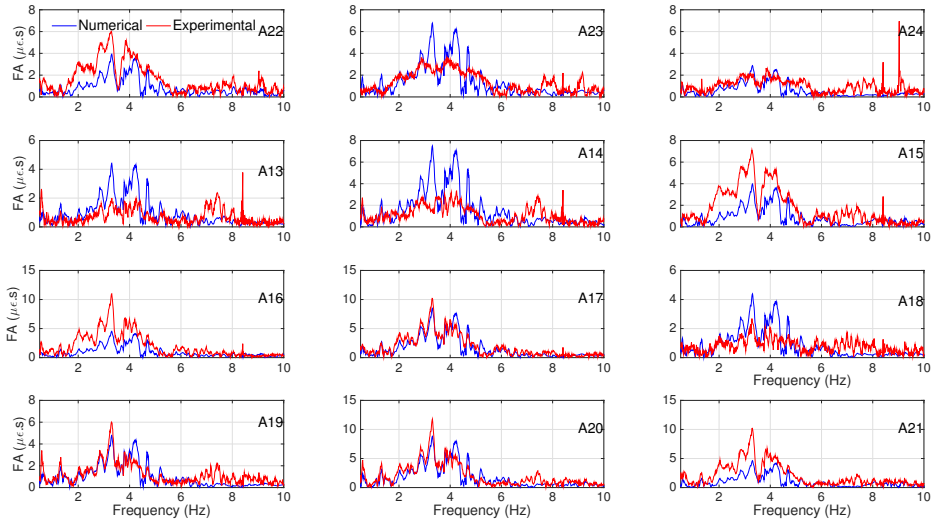

Figure 6.95: Comparison of the Fourier amplitude spectra of the circular structure for motion #07.

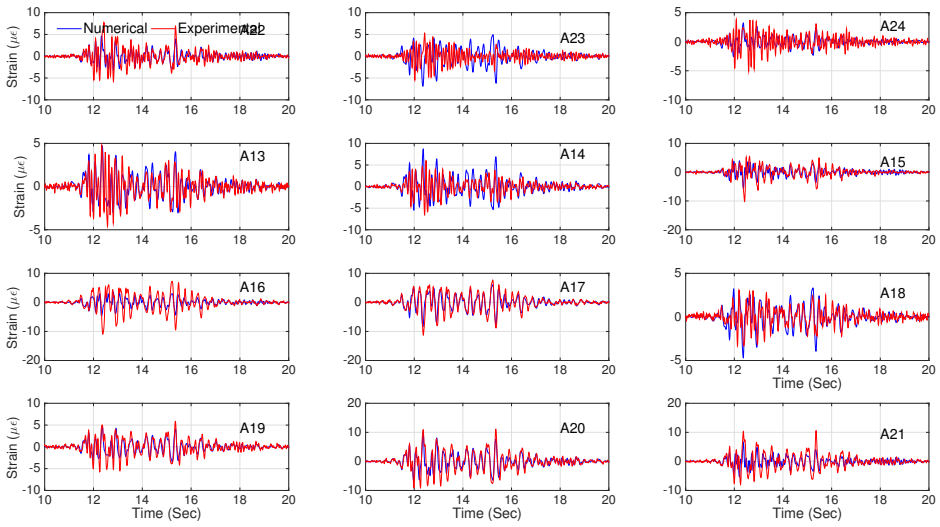

Figure 6.96: Comparison of the time series of the dynamic hoop strains of the circular structure for motion #08.

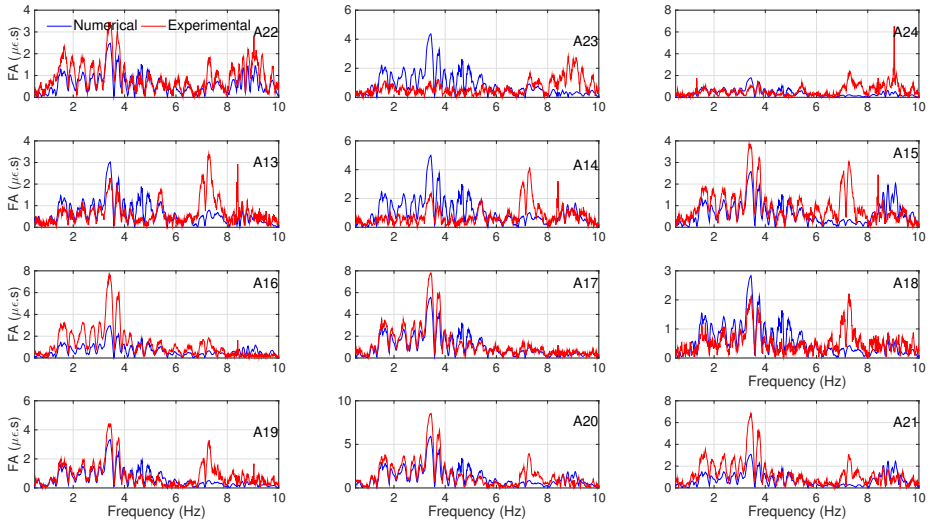

Figure 6.97: Comparison of the Fourier amplitude spectra of the circular structure for motion #08.

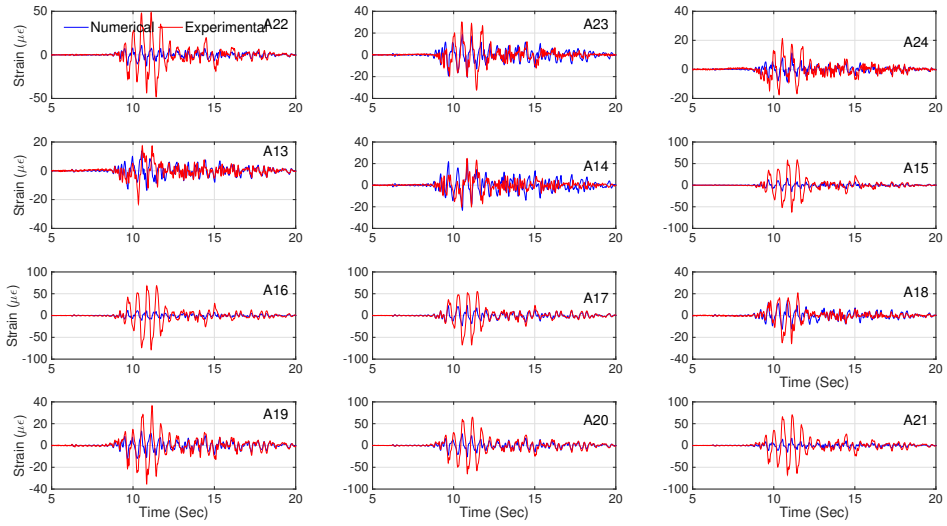

Figure 6.98: Comparison of the time series of the dynamic hoop strains of the circular structure for motion #09.

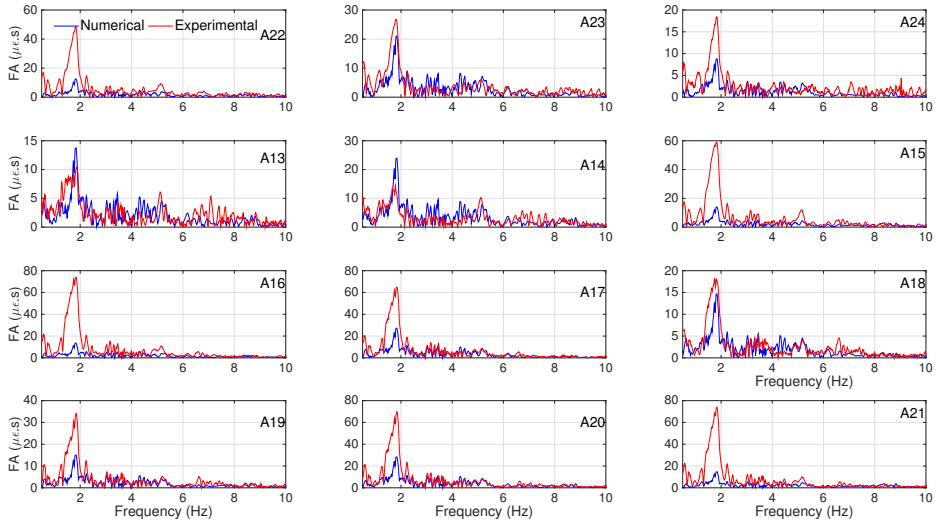

Figure 6.99: Comparison of the Fourier amplitude spectra of the circular structure for motion #09.

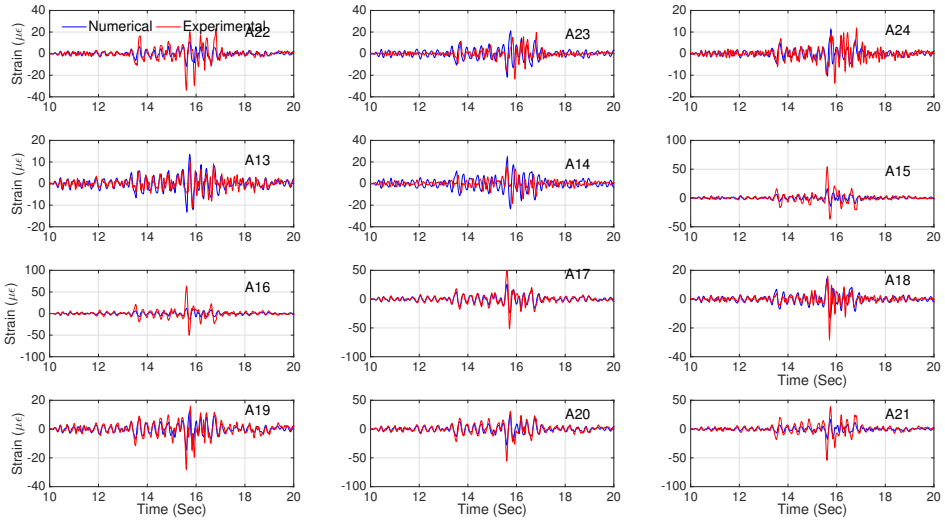

Figure 6.100: Comparison of the time series of the dynamic hoop strains of the circular structure for motion #10.

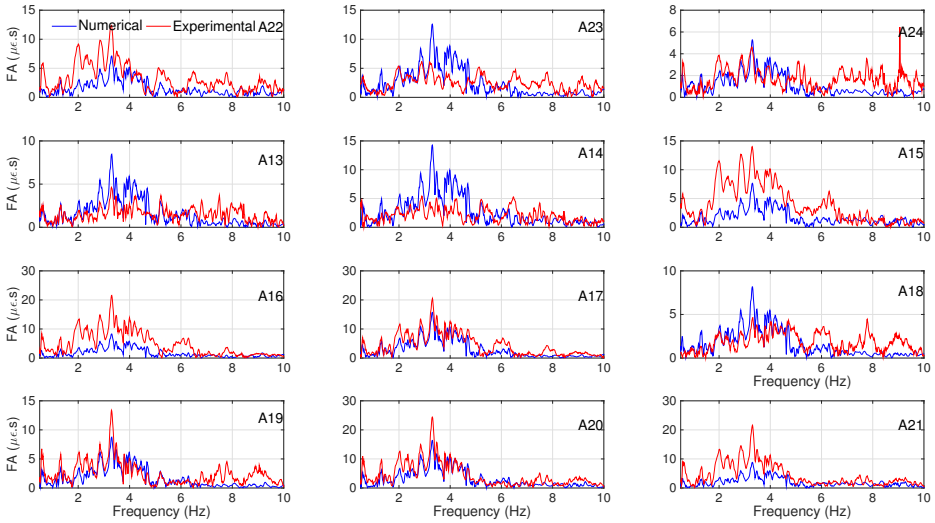

Figure 6.101: Comparison of the Fourier amplitude spectra of the circular structure for motion #10.

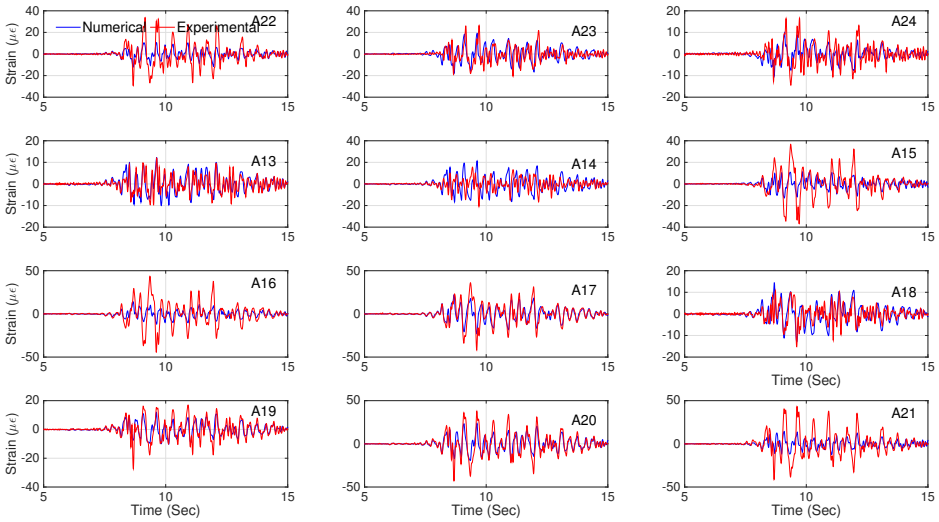

Figure 6.102: Comparison of the time series of the dynamic hoop strains of the circular structure for motion #11.

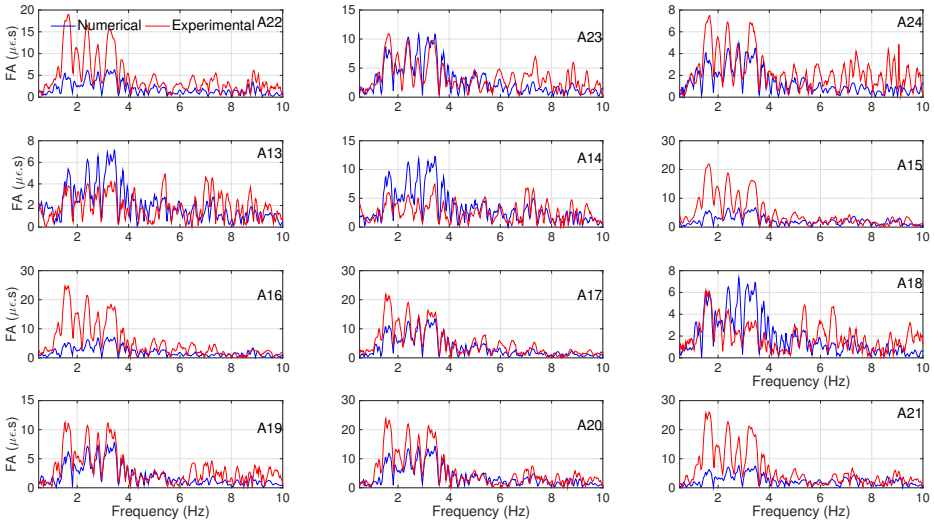

Figure 6.103: Comparison of the Fourier amplitude spectra of the circular structure for motion #11.

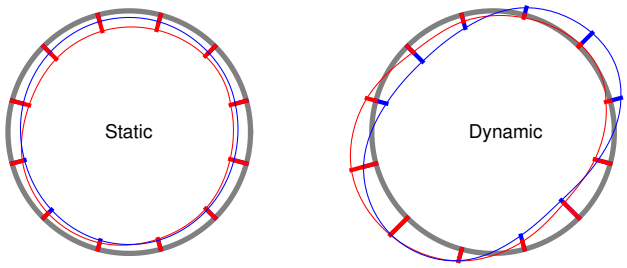

Figure 6.104: Comparison of the maximum static and dynamic hoop strain profiles of the circular structure for motion #03.

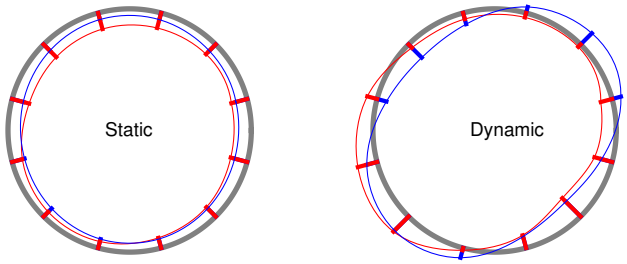

Figure 6.105: Comparison of the maximum static and dynamic hoop strain profiles of the circular structure for motion #04.

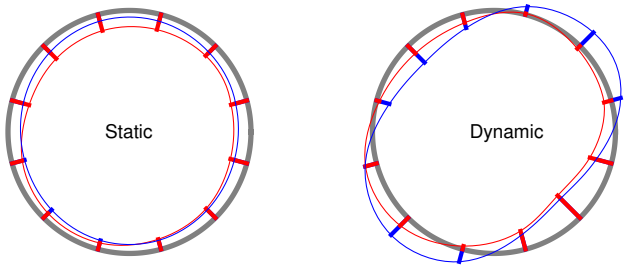

Figure 6.106: Comparison of the maximum static and dynamic hoop strain profiles of the circular structure for motion #05.

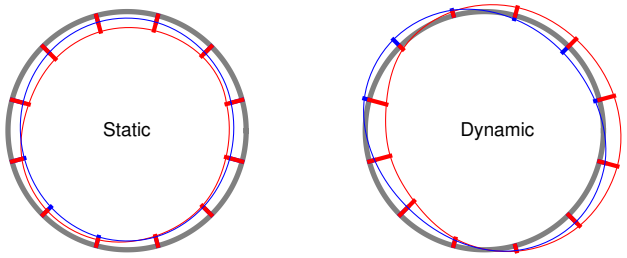

Figure 6.107: Comparison of the maximum static and dynamic hoop strain profiles of the circular structure for motion #06.

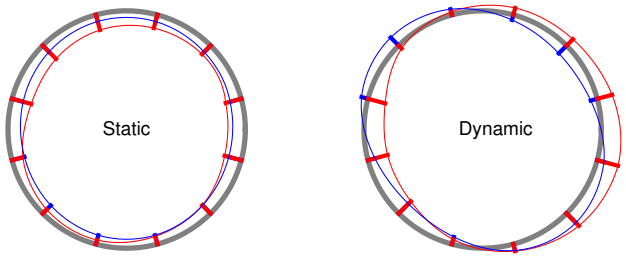

Figure 6.108: Comparison of the maximum static and dynamic hoop strain profiles of the circular structure for motion #07.

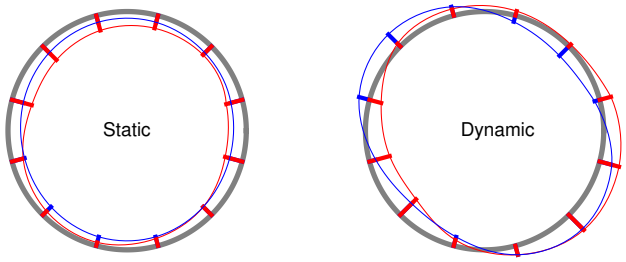

Figure 6.109: Comparison of the maximum static and dynamic hoop strain profiles of the circular structure for motion #08.

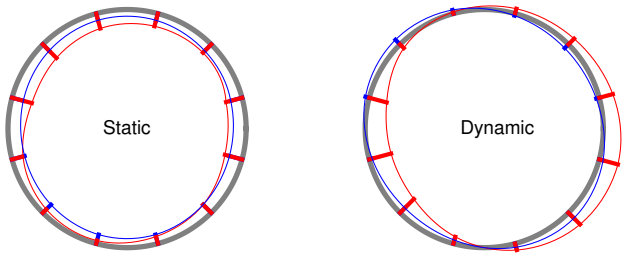

Figure 6.110: Comparison of the maximum static and dynamic hoop strain profiles of the circular structure for motion #09.

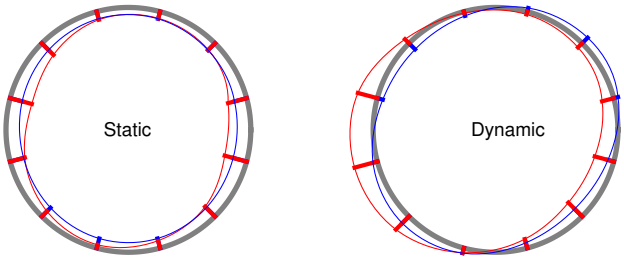

Figure 6.111: Comparison of the maximum static and dynamic hoop strain profiles of the circular structure for motion #10.

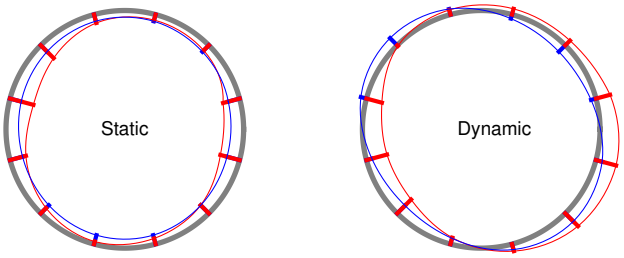

Figure 6.112: Comparison of the maximum static and dynamic hoop strain profiles of the circular structure for motion #11.

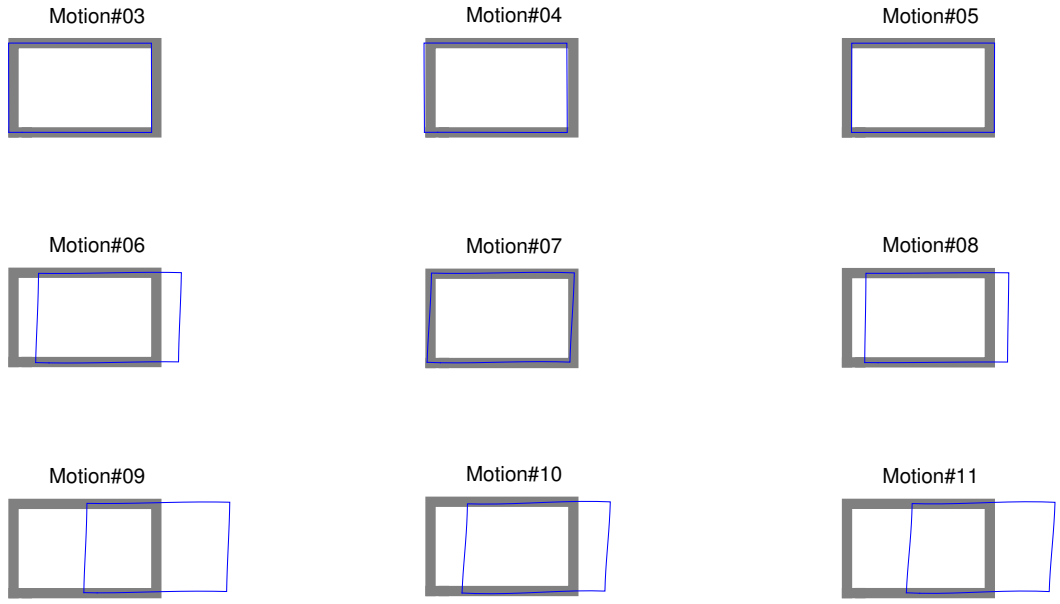

Figure 6.113: Maximum deformation plot for rectangular structure.

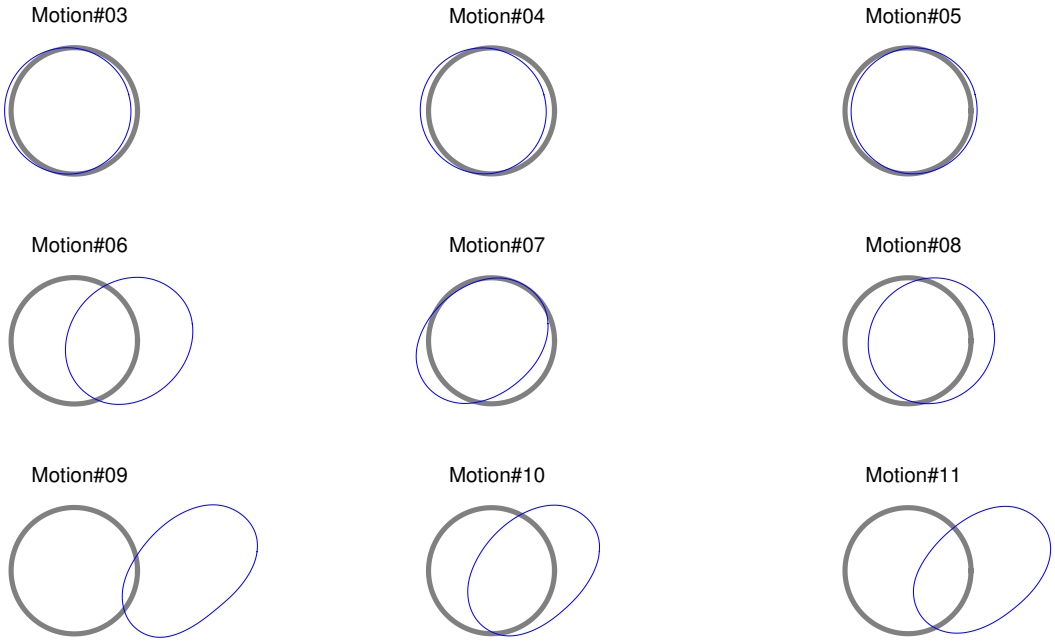

Figure 6.114: Maximum deformation plot for circular structure.

6.4.7 Error analysis

In order to summarize the capability of the calibrated numerical model in predicting different response parameters studied in this report, we compute the relative root-mean-square error (RMSE) for each response parameter as follows:

$$\text{Relative RMSE} = \frac{\sqrt{\left[\frac{1}{n}\sum_{k=1}^{n}\left(\mathrm{r}_k^{\mathrm{exp}} - \mathrm{r}_k^{\mathrm{num}}\right)^2\right]}}{\sqrt{\left[\frac{1}{n}\sum_{k=1}^{n}\left(\mathrm{r}_k^{\mathrm{exp}}\right)^2\right]}} \times 100\% \tag{6.14}$$

where n is the total number of time steps considered in the response time-series; and $\mathbf{r}^{\mathrm{exp}}$ and $\mathbf{r}^{\mathrm{num}}$ are the experimental and numerical response time-series, respectively. Considering each data point in the response time-series as different predictions in the dataset, the relative RMSE can be interpreted as the coefficient of variation, i.e. $\sigma/|\mu|$, where σ is the standard deviation and $|\mu|$ is the absolute mean value.

Figures 6.115 and 6.123 display the relative RMSE for all base shakings used in this report. We recall that AA1, AD18, AF28, AC16, AE26, and AFH30 are the ICPs measuring horizontal accelerations at the left and middle arrays in the soil; 7 and 1 are the ICPs at the bottom and top of the left wall of the rectangular structure; BT1, BL7, BB16, and BL17 are the bending strain bridges at corners of the rectangular culvert; 16 and 14 are the ICPs measuring the horizontal accelerations at θ=180 and 270 degrees, respectively, of the circular culvert; A11, A2, A5, and A8 are the bending strain bridges at θ=45, 135, 225, 315 degrees; and A23, A14, A17, and A20 are the hoop strain bridges at θ=45, 135, 225, 315 degrees. As shown, RMSE is less for higher amplitude motions in general, which is due to inherently higher signal-to-noise ratios in those experiments.

Finally, Table 6.1 summarizes the resulting maximum bending strain ratios for the rectangular culvert, maximum bending and hoop strain ratios for the circular culvert, and von Mises stress for both culverts, compared to those we obtained using the finite element model (FEM).

Table 6.1: Maximum bending and hoop strain ratios, and von Mises stress ratios between experiment and FE model predictions.

Motion	$e_b^{\square}$	$e_b^{\bigcirc}$	$e_h^{\bigcirc}$	$\sigma_{vm}^{\square}$	$\sigma_{vm}^{\bigcirc}$
3	0.89	1.37	0.98	0.89	1.29
4	0.81	1.14	0.81	0.81	1.17
5	0.77	1.26	0.87	0.77	1.26
6	1.05	0.86	0.49	1.05	0.89
7	1.17	1.33	0.63	1.17	1.15
8	0.83	0.87	0.88	0.83	0.91
$9^{(a)}$	1.07	0.63	0.34	1.07	0.59
10	1.19	0.83	0.45	1.19	0.85
11	1.13	1.23	0.53	1.13	1.22

$^{(a)}$ Only motion 9 is used for calibrating parameters of the noninear soil model for all analyses.

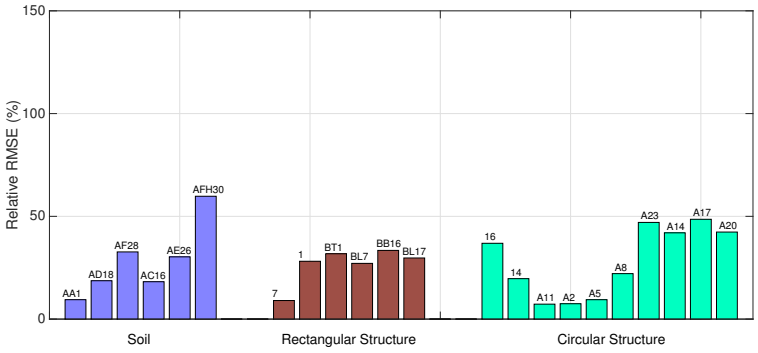

Figure 6.115: Relative RMSE for motion #03.

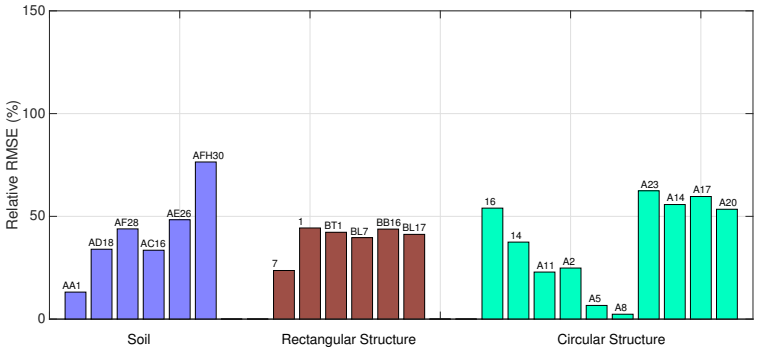

Figure 6.116: Relative RMSE for motion #04.

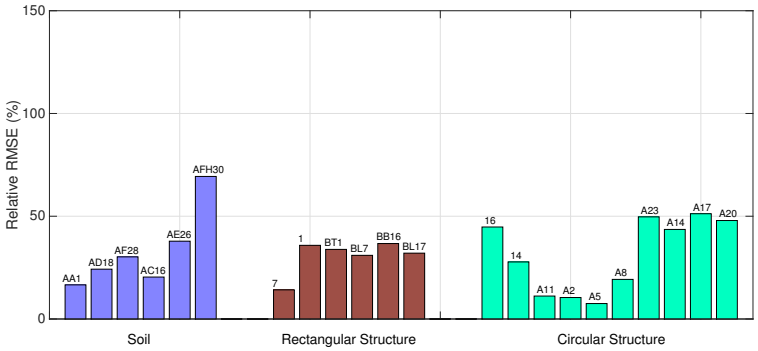

Figure 6.117: Relative RMSE for motion #05.

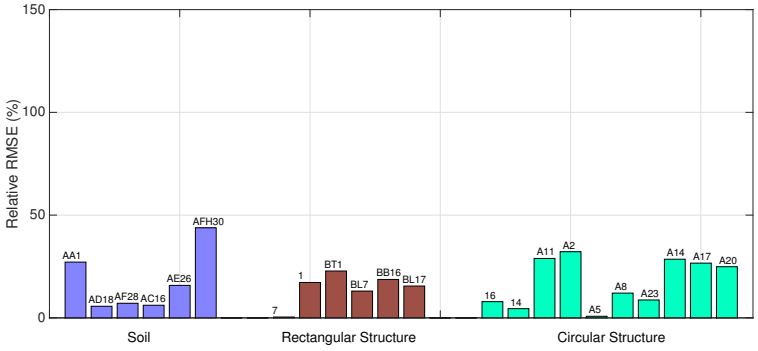

Figure 6.118: Relative RMSE for motion #06.

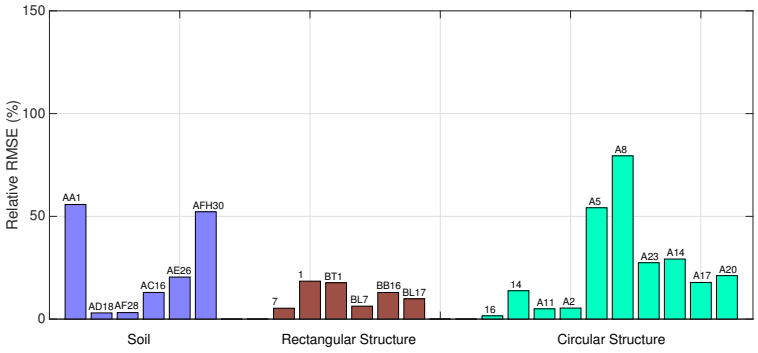

Figure 6.119: Relative RMSE for motion #07.

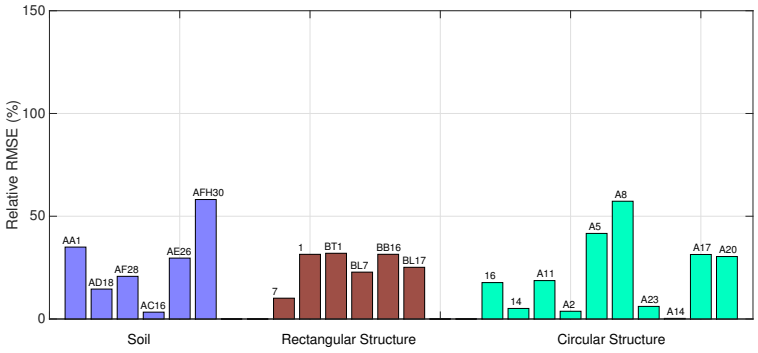

Figure 6.120: Relative RMSE for motion #08.

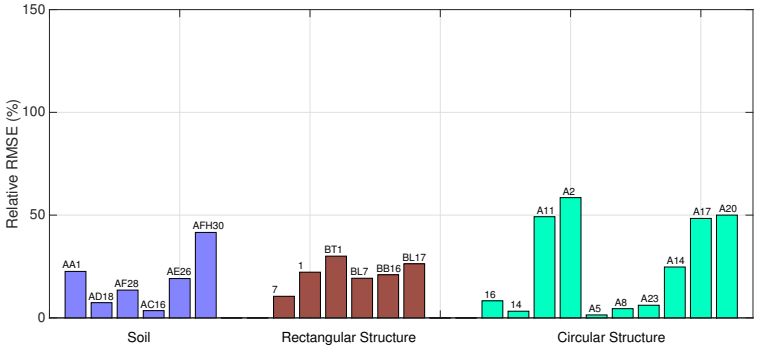

Figure 6.121: Relative RMSE for motion #09.

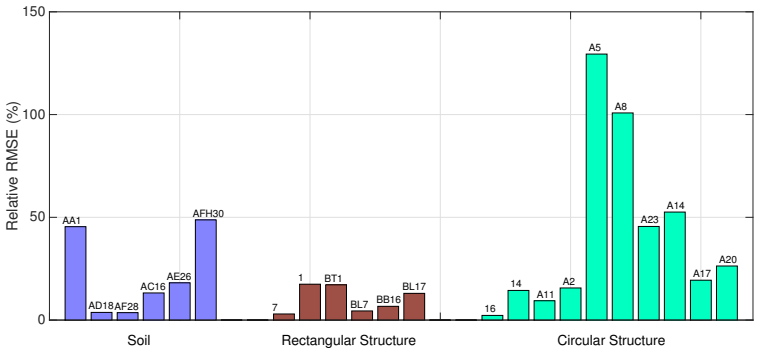

Figure 6.122: Relative RMSE for motion #10.

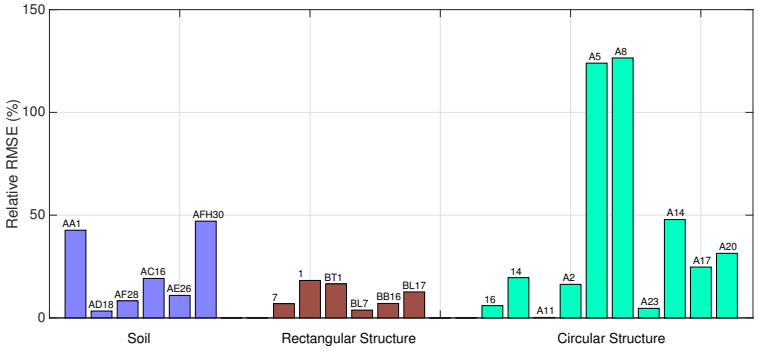

Figure 6.123: Relative RMSE for motion #11.

Chapter 7

Conclusions & recommendations

Details of the centrifuge experiments and data processing were provided in Chapters 2 and 3. Details of the NCHRP 611 method of analysis and comparison of predictions from these methods with test data were provided in Chapters 4 and 5. Finally, details of the numerical (i.e., finite element) modeling approach and its results against test data were provided in Chapter 6. In the following two sections the main findings and conclusions from these comparisons are presented along with potential caveats, and recommendations are made for future work.

7.1 Conclusions & Recommendations

NCHRP 611 Method: In this method, choosing a proper value for the maximum shear strain, which controls the seismic demand, plays the most critical role in the prediction of critical structural responses.

When we used the iterative procedure described in Chapter 5 to estimate the maximum shear strain, the bending strains in both the rectangular and circular culverts were over-predicted (see, Table 5.6). The predicted values for the rectangular box ranged from being 2.17 times (for a low amplitude motion) to 4.50 times (for a high amplitude motion) the measured value. The situation was better for the circular culvert, with predicted values being 1.29 times (for a medium amplitude motion) to 2.85 times (for a high amplitude motion) the measured values. These appeared to be severe inaccuracies for the NCHRP 611 method in predicting the bending strains.

The hoop strains in the circular culvert computed using the same method were generally

under-predicted[1], which was the case even when the NCHRP 611-recommended no-slip condition was used for computing the soil thrust—an option that provides higher values than the full-slip condition. The predicted hoop strains were as low as 0.48 times (for a high amplitude motion) and as high as 1.11 times (for a medium amplitude motion) the measured values.

The NCHRP 611 report recommends the use of more refined approaches—namely, one-dimensional site response analyses—to obtain better estimates of the maximum shear strain at the elevation of the culvert structures. As seen in Table 5.6, the use of this more refined approach resulted in improvement of the bending strain estimates for both structures, but further deterioration of the hoop strains for the circular culvert. The bending strains for the rectangular culvert were generally underestimated for the low and medium amplitude motions, and were generally overestimated for the high amplitude motions. That said, the NCHRP 611 method produced its best results for the latter (i.e., high amplitude motion) case, for which the bending strains were 1.15, 1.03, and 0.99 times the measured values for the three high amplitude base excitations. Unfortunately, while the bending strain estimate improved for the circular culvert, the hoop strains have deteriorated, which had considerable magnitudes.

Given these results, it can be concluded that using one-dimensional site response analysis in predicting the maximum shear strain should be preferred over obtaining this value (iteratively) from the modulus reduction curves, when using the NCHRP 611 methods.

Between the two structures, it was observed that the NCHRP 611 methods were more successful in capturing the relatively stiff structure's (i.e., the rectangular culvert's) responses than the flexible (circular) one. That said, it was observed that the NCHRP 611 method generally under-predicted the bending strains (especially for low and medium amplitude motions). For the circular structure, both the bending and hoop strains were under-predicted in general for all base excitations; and the worst cases of these inaccuracies were encountered for the high-amplitude base excitations.

Another important response measure considered was the von Mises stresses, which is a typical quantity used in strength-based design. The von Mises stresses (see Table 5.5) exhibited trends that were similar to the strains. Namely, (*i*) they were more accurate when obtained using the one-dimensional site response analyses; (*ii*) they were more accurate for the stiff (i.e., rectangular) structure than they were for the flexible (circular) one. It appeared that for most cases, the von Mises stresses obtained using the refined NCHRP approach provided adequate estimates, as the NCHRP-to-experiment ratios von Mises stresses ranged between 0.7 to 1.2. This implies that a strength-based design would require a safety factor of at least $1/0.7 \approx 1.43$ just to handle uncertainties in input motions *and* the model features related to ground motions—henceforth collectively referred to as epistemic uncertainties.

[1]The analogous (hoop) strains for the rectangular culvert were negligible in all experiments.

On the other hand, the same ratios were bracketed from 0.4 to 1.5 for the circular culvert, implying an factor of safety of 2.5, which is quite large.

Given these observations, it appears that the use of NCHRP 611 methods of analysis on flexible structures may not produce adequately safe designs. It is likely that the situation will be worse for structures with higher relative flexibility and for higher amplitude motions.

On the other hand, predictions obtained using the refined NCHRP approach for rigid culverts appear acceptable. It should be noted here that the use of the refined NCHRP approach requires one-dimensional site response analyses for *every* ground motion considered.

Finite Element (FE) Approach: Comparison of the numerical and experimental results showed that by using only a few sets of recorded free-field accelerations to calibrate the soil constitutive relationship, the finite element model was more systematically successful in predicting the key response parameters of both culvert specimens compared to the NCHRP 611 methods (see, §6.1, for details). As shown in Table 6.1, for both the rectangular and circular structures, the bending strain ratios are closer to one compared to those computed using the NCHRP methods. For the hoop strain, on the other hand, using the finite element approach resulted in ratios that are closer to those obtained using the NCHRP iterative method for the low amplitude motions, and closer to those obtained using the NCHRP refined approach for the moderate and high amplitude motions. As such, it is concluded that the finite element approach performed better in predicting bending strains regardless of the structure flexibility, while its accuracy in capturing the hoop strains decreased for cases in which the soil behaves more nonlinearly.

For the rigid (rectangular) culvert the ratio of predicted-to-experimental von Mises stresses ranged from 0.77 to 1.19, implying an epistemic factor of safety of $1/0.77 \approx 1.30$ (as compared to 1.43 for the refined NCHRP method). For the circular culvert, the same ratio ranged from 0.59 to 1.29, implying an epistemic factor of safety of $1/0.59 \approx 1.70$ (as compared to 2.5 for the refined NCHRP method). As such, it can be concluded that the FE method can handle rigid as well as flexible culverts equally well, and generally better than the NCHRP method.

It is also important to note that the soil model in the FE calculations was calibrated only once, using the centrifuge free-field array records during motion #9. It is, therefore, reasonable to expect that the FE model predictions could be made better overall, if its soil model was calibrated using free-field motions from multiple tests.

7.2 Caveats & Recommended Future Studies

In this report, the focus was to investigate the predictive capabilities of the "NCHRP 611" method as well as a direct numerical (i.e., a finite element) model in capturing the key response parameters of two rectangular and circular culvert structures subject to earthquake base shakings, by considering the results of the centrifuge experiments as the "true" response. This study suggest the following steps need to be taken in order to gain better insights on the predictive capabilities of the aforementioned methodologies.

1. Due to technical difficulties of sensors calibration, especially the strain bridges, the nominal sensitivity factors were used in signal processing. This is likely the primary source of various existing discrepancies reported in Chapters 5 and 6. It would be informative to explore the possibility of using an advanced (e.g., a machine-learning) algorithm to identify and exclude this source of measurement error from centrifuge data.

2. As it was observed that the accuracy of the NCHRP 611 method depended critically on the estimation of the maximum shear strain, it appears important to improve the models that predict this quantity. For example, future studies could be directed to improving Eq. 4.1 and Eq. 1. These equations yield the peak shear strain estimate, based on peak ground acceleration and its assumed variation with respect to depth. It may be possible to improve these predictions with more sophisticated methods of wave propagation and soil domains models.

3. Two main ingredients for the calibration of the soil model in this study has been the maximum shear modulus and the modulus reduction curves. Moreover, the soil-structure interface is modeled by using an interface element with a nominally chosen friction coefficient. It would be useful to perform numerical analyses to determine how sensitive the key response parameters are to variations in the numerical model parameters. The same study should be carried out on the NCHRP 611 method. Such a study would enable identification of the most influential parameters, and therefore to systematically improve the NCHRP 611 methodology as well as the numerical modeling approach.

4. Only earthquake base shakings were studied in this report. In order to have better understanding on behavior of the culvert structures over the wider range of frequencies, the sine-sweep and stepped-sine data should be studied in similar fashion.

5. Only two culvert structures were examined numerically. It is possible to use the FE model calibrated (and subsequently validated) here, to perform parametric studies using a broad range of ground motions, soil properties, structural geometries and properties to bracket that acceptable range of applicability of the NCHRP 611 method and to possibly improve it for flexible structure, by adding higher modes to it. This

appears especially important for tunnels, which will exhibit far higher flexibilities than the average culvert structure.

6. It appears possible to develop a FE-based analysis and design tool for culvert structures, which could take basic inputs from the user and can compute responses for any culvert geometry, soil profiles and properties, under any free-field motion. Given recent advances in cloud computing, such a tool would provide efficient aid to the design engineer.

7. The present study focused primarily on the dynamic responses of culverts. As centrifuge testing is well known to be unsuitable in general to obtain static (or quasi-static) behaviors from soil-structure specimens. As such, it is recommended to carry out field tests and use data from instrumented culverts in the field to examine static earth pressures that develop around them.

Bibliography

O. Abuhajar, H. E. Naggar, and T. Newson. Centrifuge modeling of the static and seismic soil culvert interaction. Technical report, University of Western Ontario, 2014.

O. Abuhajar, H. E. Naggar, and T. Newson. Experimental and numerical investigations of the effect of buried box culverts on earthquake excitation. *Soil Dynamics and Earthquake Engineering*, 79:130–148, 2015.

E. Agapaki, E. Esmaeilzadeh Seylabi, S. J. Brandenberg, J. P. Stewart, and E. Taciroglu. Centrifuge modeling of culvert structures to evaluate seismic earth pressures arising from soil-structure interaction. In *1st International Conference on Natural Hazards & Unfrastructure*, 28-30 June 2016.

D. G. Anderson, G. R. Martin, I. Lam, and J. N. Wang. *NCHRP Report 611: Seismic analysis and design of retaining walls, buried structures, slopes, and embankments.* Transportation Research Board, Washington, DC, 2008.

A. Bobet. Drained and undrained response of deep tunnels subjected to far-field shear loading. *Tunneling and Underground Space Technology*, 25:21–31, 2010.

A. Bobet, G. Fernande, H. Huo, and J. Ramirez. A practical iterative procedure to estimate seismic-induced deformations of shallow rectangular structures. *Canadian Geotechnical Journal*, 45:923–938, 2008.

R. I. Borja and A. P. Amies. Multiaxial cyclic plasticity model for clays. *Journal of Geotechnical Engineering*, 120(6):1051–1070, 1994.

R. I. Borja and W.-H. Wu. Vibration of foundations on incompressible soils with no elastic region. *Journal of Geotechnical Engineering*, 120(9):1570–1592, 1994.

R. I. Borja, C.-H. Lin, K. M. Sama, and G. M. Masada. Modeling nonlinear ground response of non-liquifiable soils. *Earthquake Engineering and Structural Dynamics*, 29:63–83, 2000.

S. J. Brandenberg, S. Choi, B. L. Kutter, D. W. Wilson, and J. C. Santamarina. A bender element system for measuring shear wave velocities in centrifuge models. In *6th International Conference on Physical Modeling in Geotechnics*, pages 165–170, 2006.

S. J. Brandenberg, G. Mylonakis, and J. P. Stewart. Kinematic framework for evaluating seismic earth pressures on retaining walls. *Journal of Geotechnical and Geoenvironmental Engineering*, 141:1–10, 2015.

H.-Y. Chao and R. I. Borja. Nonlinear dynamic soil-structure interaction analysis and application to Lotung problem. Technical Report J. A. Blume Earthquake Engrg. Ctr. Tech. Rep. 129, Stanford University, Stanford, CA, 1998.

U. Cilingir and S. P. G. Madabhushi. A model study on the effects of input motion on the seismic behavior of tunnels. *Soil Dynamics and Earthquake Engineering*, 31:452–462, 2011a.

U. Cilingir and S. P. G. Madabhushi. Effect of depth on the seismic response of square tunnels. *Soils and Foundations*, 51(3):449–457, 2011b.

Y. F. Dafalias and E. P. Popov. Cyclic loading for materials with a vanishing elastic region. *Nuclear Engineering and Design*, 41(2):293 – 302, 1977. ISSN 0029-5493. doi: http://dx.doi.org/10.1016/0029-5493(77)90117-0.

Y. Deng, S. Dashti, A. Hushmand, C. Davis, and B. Hushmand. Seismic response of underground reservoir structures in sand: Evaluation of class-c and c1 numerical simulations using centrifuge experiments. *Soil Dynamics and Earthquake Engineering*, 85:202–216, 2016.

Department of Transportation State of California. Standard plans (2015 edition). http://www.dot.ca.gov/hq/esc/oe/project_plans/HTM/stdplns-US-customary-units-new15.htm, 2015.

E. Esmaeilzadeh Seylabi, E. Agapaki, D. Pitilakis, S. J. Brandenberg, J. P. Stewart, and E. Taciroglu. Data report: Development of validated methods for soil-structure interaction analysis of buried structures. https://jupyter.designsafe-ci.org/user/culvert/notebooks/mydata/DigitalDataReport/Data%20Report%20v.02/Data%20Report.ipynb, 2017.

E. Esmaeilzadeh Seylabi, H. Ebrahimian, W. Zhang, D. Asimaki, and E. Taciroglu. Bayesian estimation of nonlinear soil model parameters using centrifuge experimental data. In *The Proceedings of Geotechnical Earthquake Engineering and Soil Dynamics V*, Austin, TX, 2018.

B. O. Hardin and V. P. Drnevich. Shear modulus and damping in soils. Technical report, Universtiy of Kentucky, 1970.

Y. M. A. Hashash, J. J. Hook, B. Schmidt, and J. I. Yao. Seismic design and analysis of underground structures. *Tunneling and Underground Space Technology*, 2001.

Y. M. A. Hashash, D. Park, and J. I.-C. Yao. Ovaling deformations of circular tunnels under

seismic loading, an update on seismic design and analysis of underground structures. *Tunnelling and Underground Space Technology*, 20:435–441, 2005.

Y. M. A. Hashash, M. I. Musgrove, J. A. Harmon, D. Groholski, C. A. Phillips, and D. Park. Deepsoil v6.1, user manual. Technical report, University of Illinois at Urbana-Champaign, Urbana, IL, 2016.

Hibbit, Karlsson, and Sorensen. *ABAQUS/Standard Analysis User's Manual*. Hibbitt, Karlsson, Sorensen Inc., USA, 2007.

M. G. Katona. Seismic Design and Analysis of Buried Structures with CANDE-2007. *Journal of Pipeline Systems Engineering and Practice*, 1(3):111–119, 2010.

S. Kontoe, V. Avgerinos, and D. M. Potts. Numerical validation of analytical solutions and their use for equivalent linear seismic analysis of circular tunnels. *Soil Dynamics and Earthquake Engineering*, 66:206–219, 2014.

B. L. Kutter, I. M. Idriss, T. Kohnke, J. Lakeland, X. S. Li, W. Sluis, X. Zeng, R. C. Tasuscher, Y. Goto, and I. Kubodera. Design of a large earthquake simulator at uc davis. *In Centrifuge*, 94:169–175, 1994.

G. Lanzano, E. Billota, G. Usso, G. Silvestri, and S. P. G. Madabhushi. Centrifuge modeling of seismic loading on tunnels in sand,. *Geotechnical Testing Journal*, 35, 2012.

G. Lanzano, E. Billota, G. Russo, and F. Siverstri. Experimental and numerical study on circular tunnels under seismic loading. *European Journal of Environmental and Civil Engineering*, 19:539–563, 2015.

J. S. Lee and J. C. Santamarina. Bender elements: performance and signal interpretation. *Journal of Geotechnical and Geoenvironmental Engineering*, 131:1063–1070, 2005.

G. Madabhushi. *Centrifuge modeling for civil engineers*. Taylor & Francis Group, 2014.

N. Matasovic. *Seismic Response of Composite Horizontally-Layered Soil Deposits*. PhD thesis, University of California, Los Angeles, 1993.

F. Y. Menq. *Dynamic properties of sandy and gravelly soils*. PhD thesis, University of Texas at Austin, 2003.

N. Mononobe and M. Matsuo. On the determination of earth pressures during earthquakes. In *Word Engineering Congress*, volume 9, pages 179–187, 1929.

K.-H. Park, K. Tantayopin, B. Tontavanich, and A. Owatsiriwong. Analytical solution for seismic-induced ovaling of circular tunnel lining under no-slip interface conditions: a revisit. *Tunnelling and Underground Space Technology*, 24:231–235, 2009.

J. Penzien. Seismically induced racking of tunnel linings. *Earthquake Engineering and Structural Dynamics*, 29:683–691, 2000a.

J. Penzien. Seismically induced racking of tunnel linings. *International Journal of Earthquake Engineering and Structural Dynamics*, 29:683–691, 2000b.

F. Pérez and B. E. Granger. IPython: a system for interactive scientific computing. *Computing in Science and Engineering*, 9(3):21–29, May 2007. ISSN 1521-9615. doi: 10.1109/MCSE.2007.53. URL http://ipython.org.

E. M. Rathje, C. Dawson, J. E. Padgett, J.-P. Pinelli, D. Stanzione, A. Adair, P. Arduino, S. J. Brandenberg, T. Cockerill, C. Dey, et al. Designsafe: New cyberinfrastructure for natural hazards engineering. *Natural Hazards Review*, page 06017001, 2017.

S. K. Roesler. Anisotropic shear modulus due to stress anisotropy. *Journal of Geotechnical Engineering*, 105:871–888, 1979.

J. Simo and T. Hughes. *Computational Inelasticity*. Interdisciplinary Applied Mathematics. Springer New York, 2000. ISBN 9780387975207. URL https://books.google.com/books?id=ftL2AJL8OPYC.

J. P. Stewart, K. Afshari, and Y. M. A. Hashash. Guidelines for performing hazard-consistent one-dimensional ground response analysis for ground motion prediction. PEER Report No. 2014/16, Pacific Earthquake Engineering Research Center, UC Berkeley, CA, 2014.

G. Tsinidis. Response characteristics of rectangular tunnels in soft soil subjected to transversal ground shaking. *Tunneling and Underground Space Technology*, 62:1–22, 2017.

G. Tsinidis, K. Pitilakis, G. Madabhushi, and C. Heron. Dynamic response of flexible square tunnels: centrifuge testing and validation of existing design methodologies. *Géotechnique*, 65(5):401–417, May 2015.

G. Tsinidis, K. Pitilakis, and G. Madabhushi. On the dynamic response of square tunnels in sand. *Engineering Structures*, 125:419–437, 2016.

D. Ulgen, S. Saglam, and M. Y. Ozkan. Dynamic response of a flexible rectangular underground structure in sand: centrifuge modeling. *Bulletin of Earthquake Engineering*, 13: 2547–2566, 2015.

J. Wang. Seismic design of tunnels: A simple state-of-the-art design approach. Technical report, Parsons, Brinckerhoff, Quade and Douglas Inc., 1993a.

J. N. Wang. Seismic design of tunnels: A simple state-of-the-art approach. Technical report, Parsons, Brinckerhoff, Quade and Douglas Inc., 1993b.

S. Yamashita, T. Kawaguchi, Y. Nakata, T. Mikami, T. Fujiwara, and S. Shibuya. Interpretation of international, parallel test on the measurement of gmax using bender elements. *Soils and Foundations*, 49:631–650, 2009.

Z. Yang, A. Elgamal, and E. Parra. Computational model for cyclic mobility and associated shear deformation. *Journal of Geotechnical and Geoenvironmental Engineering*, 129(12): 1119–1127, 2003.

W. Zhang, E. Esmaeilzadeh Seylabi, and E. Taciroglu. Validation of a three-dimensional constitutive model for nonlinear site response and soil-structure interaction analyses using centrifuge test data. *International Journal for Numerical and Analytical Methods in Geomechanics*, 41(18):1828–1847, 2017.